Non Linear Ultrasound Doppler and the Detection of Targeted Contrast Agents

Véronique Catherine Mahue

A thesis submitted for the degree of Doctor of Philosophy

Department of Bioengineering

Imperial College London

February 2011

Declaration of Originality

I declare that this thesis is the result of my own work carried out in the department of Bioengineering, Imperial College London.
All the work, analysis and illustrations were performed by me, unless otherwise specified in the text.

Véronique Mahue

Abstract

One of the main challenges in molecular imaging with targeted contrast agents is the detection and discrimination of attached agents from the rest of the signals originating from freely flowing agents and tissue. The aim of this thesis was to develop methods for the detection of targeted microbubbles.

One approach consisted of investigating the use of nonlinear Doppler for this purpose. Nonlinear Doppler enables the differentiation of moving from non-moving and linear from nonlinear scattering. Targeted microbubbles are static and nonlinear scatterers and they should be detected using this technique.

A novel nonlinear Doppler technique: Pulse subtraction Doppler, was developed and compared to pulse inversion Doppler. It is shown that both techniques lead to similar Doppler spectra and depending on the medical applications and the equipment limitations, both techniques have benefits.

This served as a starting point for the derivation of a generalised nonlinear Doppler technique, based on combined linear pulse pair sequences and tested in a simulation study. The response from a single microbubble was simulated for different pulse combinations and the pulse sequences were compared with regards to criteria specific to imaging requirements. It was shown that depending on initially set criteria, such as transmitted energy, mechanical index or scanner characteristics, certain pulse combinations offer alternatives to the current imaging modalities and allow to take into account specific constrains due to the targeted application/equipment. Furthermore, the proposed approach is directly applicable in a strict non linear imaging approach, without Doppler processing.

An *in vitro* phantom was designed in order to assess pulse subtraction Doppler for the detection and discrimination of static nonlinear microbubbles in the presence of free flowing ones. It was shown that pulse subtraction Doppler enables such discrimination and the practicability for *in vivo* situations is discussed.

The pulse subtraction Doppler sequences were also tested on a phantom containing magnetic bubbles. It was shown that the magnetic bubbles can be immobilised through a magnetic field to a

specific region of interest under flow conditions. The bubbles also showed to be acoustically detectable and to scatter linearly at diagnostic driving pressures.

Preliminary work regarding experimental biotinylated microbubbles and their attachment to streptavidin coated surfaces is also presented.

Due to their proximity to a wall, researchers have found that targeted microbubbles exhibit different acoustic signatures compared to free ones and this knowledge can improve their detection techniques. The behaviour of microbubbles against a membrane of varying stiffness was also studied through high speed camera observations. It was found both experimentally and by comparison to theoretical modelling that within the stiffness range of human blood vessels the change in acoustical behaviour of microbubbles is negligible.

This thesis has taken two complementary research approaches which have shown to constitute advancements for the detection and discrimination of targeted microbubbles.

Table of Contents

DECLARATION OF ORIGINALITY 2

ABSTRACT 3

TABLE OF CONTENTS 5

ACKNOWLEDGEMENTS 9

LIST OF FIGURES 11

LIST OF TABLES 16

ABBREVIATIONS USED 17

CHAPTER 1 INTRODUCTION TO ULTRASOUND MOLECULAR IMAGING 18

1.1 Vascular and perfusion disease processes 18

1.2 Ultrasound imaging and contrast imaging 19

1.3 Targeted contrast agents 21
1.3.1 Targeting strategies 21
1.3.2 Molecular imaging applications 22
1.3.3 Main challenges in ultrasound molecular imaging 23
1.3.4 Detection techniques 23

1.4 Overview of thesis 24

CHAPTER 2 THEORY OF CONTRAST AND TARGETED IMAGING 26

2.1 Contrast enhanced imaging 26
2.1.1 Microbubble modelling 26
2.1.1.1 Rayleigh-Plesset equation 26
2.1.1.2 Polynomial expansion model 28
2.1.2 Ultrasound Contrast agent imaging modalities 28
2.1.2.1 Harmonic imaging 28
2.1.2.2 Pulse inversion imaging 29
2.1.2.3 Other multipulse sequences 31

2.2 Velocity imaging in medical ultrasound imaging 32
2.2.1 Continuous wave and pulsed wave Doppler 32
2.2.2 Velocity estimation techniques 35
2.2.2.1 Time shift estimation techniques 35

2.2.2.2 Phase shift estimation techniques 36
2.2.3 Colour flow imaging 38
2.2.4 Nonlinear Doppler 40
2.2.4.1 Harmonic Doppler 40
2.2.4.2 Pulse inversion Doppler 40

2.3 Targeted contrast agent detection techniques 41
2.3.1 Targeted contrast agent acoustic behaviour 41
2.3.2 Signal processing techniques 41

2.4 Summary 44

CHAPTER 3 PULSE SUBTRACTION DOPPLER 45

3.1 Introduction 45

3.2 Theory 46
3.2.1 Pulse subtraction principle 46
3.2.2 Pulse subtraction Doppler principle 48

3.3 Methods 49
3.3.1 Simulations 49
3.3.2 Experiments 50

3.4 Results 52
3.4.1 Simulations 52
3.4.2 Experiments 54

3.5 Discussion 56

3.6 Conclusions 58

CHAPTER 4 GENERALISED CONTRAST IMAGING AND NONLINEAR DOPPLER . 60

4.1 Introduction 60

4.2 Nonlinear Doppler theory 63
4.2.1 Driving pulses 63
4.2.2 Echo processing 63
4.2.3 Effect of noise 64
4.2.4 Nonlinear Doppler processing 65
4.2.4.1 Linear case 65
4.2.4.2 Nonlinear case 66
4.2.4.3 Relation between the residue and the amount of nonlinear energy in the Doppler spectrum 67
4.2.5 Summary 67

4.3 Methods 68

4.4 Simulations 68
4.4.1.1 Pulse sequences 68
4.4.1.2 Pulse design parameters 69
4.4.1.3 Contrast 69
4.4.2 Types of criteria 70
4.4.2.1 Pulse design criteria 70
4.4.2.2 Contrast criteria 72

4.5 Results 72

4.6 Discussion 81
4.6.1 Harmonic analysis 81
4.6.2 Comparison criteria 82
4.6.3 Hardware nonlinearities 83
4.6.4 Effect of noise 84
4.6.5 Effects of ultrasound propagation 84
4.6.6 Pulse combinations 85
4.6.7 Single bubble simulation 85

4.7 Conclusion 86

CHAPTER 5 TOWARDS THE DETECTION OF TARGETED MICROBUBBLES WITH NONLINEAR DOPPLER 87

5.1 Introduction 87

5.2 Imaging of static microbubbles 88
5.2.1 Methods 89
5.2.1.1 Flow phantom circuit 89
5.2.1.2 Ultrasound exposure 89
5.2.1.3 Doppler echo processing 91
5.2.2 Results 91
5.2.3 Discussion 93
5.2.4 Conclusion 95

5.3 Imaging of magnetic bubbles 96
5.3.1 Methods 96
5.3.1.1 Microscopy images 96
5.3.2 Flow phantom circuit 96
5.3.2.1 Magnet 97
5.3.2.2 Ultrasound exposure 97
5.3.2.3 B-mode cine loop capture 98
5.3.2.4 RF capture 98
5.3.3 Results 98
5.3.3.1 Bubble size distribution 98
5.3.3.2 Bubble behaviour under microscope 99
5.3.3.3 B-mode cine loop capture 100
5.3.3.4 RF data 101
5.3.4 Discussion 103
5.3.5 Conclusion 104

5.4 Preliminary work on biotinylated bubbles 104
5.4.1 Methodology 105
5.4.1.1 General properties of the biotinylated microbubbles 105
5.4.1.2 Coating of a surface with streptavidin 105
5.4.1.3 Washing of microbubbles 106
5.4.1.4 Targeting of microbubbles to the surface 107
5.4.2 Imaging 107
5.4.2.1 Microscopy 107
5.4.2.2 Confocal microscopy 109
5.4.3 Conclusion 111

5.5 General conclusion 112

CHAPTER 6 OSCILLATIONS OF MICROBUBBLES IN CONTACT WITH AN ELASTIC WALL 113

6.1 Introduction 113

6.2 Methods 115
6.2.1 Preparation of the membranes 115
6.2.2 Tensile testing of the membranes 116
6.2.3 Experimental set up 118
6.2.4 Optical experiment 120
6.2.5 Modelling 122

6.3 Results 124
6.3.1 High speed camera graphs plots 124
6.3.2 Modelling results 126

6.4 Discussion and future work 129
6.4.1 Discussion 129
6.4.2 Future work suggestions 130

6.5 Conclusion 131

CHAPTER 7 CONCLUSIONS AND ACHIEVEMENTS 133

7.1 Overview 133

7.2 Pulse subtraction Doppler 134

7.3 Generalised contrast imaging and nonlinear Doppler 135

7.4 Towards the detection of targeted bubbles with nonlinear Doppler 138
7.4.1 Imaging of static microbubbles 138
7.4.2 Imaging of magnetic microbubbles 139
7.4.3 Preliminary work on biotinylated microbubbles 140

7.5 Oscillations of microbubbles in contact with an elastic wall 140

7.6 Future research directions for ultrasound molecular imaging 142

7.7 Principal achievements 144

7.8 Final conclusion 145

REFERENCES 146

APPENDIX 155

Acknowledgements

I would like to thank my supervisor, Dr Mengxing Tang for all his support, scientific guidance and helpful criticism towards becoming an independent researcher. In particular, I would like to thank him for always challenging and questioning my work. I am also very grateful to my second supervisor, Dr Rob Eckersley for all his technical advice and constant encouragement. In particular, I would like to thank him for all his advice in the design of experiments, in technical writing and for giving me so many comments to work on for all my chapters.

I would also like to thank my two examiners, Dr Ayache Bouakaz and Dr Rob Dickinson, for evaluating my PhD. I thoroughly enjoyed the experience of “defending” my work and took onboard useful criticism.

My PhD would not have been the same without the help of Dr Jean Martial Mari. He was not only a brilliant colleague, but also a great friend. Through innumerable discussions Jean Martial gave me tips and tricks to tackle problems PhD students usually encounter, such as applying for travel grants, preparing efficiently oral presentations and making “beautiful lists”. Jean Martial also taught me so much in the lab and I am immensely thankful for that. Even when he was back in France, Jean Martial was still there to motivate and encourage me during the hard writing up period. Merci pour tout Jean Martial!

I would also like to thank Dr Charles Sennoga for providing me with all the bubbles I needed for my experiments and for his patience whilst teaching me so many chemistry techniques. It has always been a pleasure to work with you and I very much enjoyed all our discussions!

I would also like to thank Dr Eleanor Stride for collaborating on several projects and for all her useful advice. Thanks also go to Dr Sergey Martynov and to Dr Spyros Masouros for both promptly accepting to help me in one of my studies. My thanks also go to Ken Keating who was always ready to give a hand and help with complex laboratory equipment.

I would like to thank the rest of the ultrasound group for their support and helpful input during our weekly group meetings, notably Dr Helen Mulvana, Dr Rui Li, Jonathan Loughran, Jonathan Casey, Richard Browning, Dr Daniel Finfer and Prof David

Cosgrove. These lab meetings were a great place to debate, discuss and comment on the work of all the group members. I will definitely miss them.

I would like to thank Prof Colin Caro and his PA Andrea Laine for their administrative support and career-oriented advice. My thanks also go to Kate Hobson for all her efficient help in administrative matters.

My attendance to international conferences would not have been possible without the financial support from a number of institutions. I would like to thank the department of Bioengineering, the Imperial College Trust, the Old Centralians' Trust, the Royal Academy of Engineering, the International Congress of Ultrasonics and the IEEE UFFC.

I would like to thank all my friends who through many different ways have made my life in London very enjoyable; in particular my climbing friends, Florian, Gemma, Delphine, Guillaume, Alejandro, as well as Lise, who managed to keep me motivated until the end. I would also like to thank all my friends from France, from Germany and from all over the world, many of whom came to visit me more than once!

I would like to thank my parents and family for all their support, encouragement and for always being there for me during all these long studies I chose to pursue.

Finally I would like to thank my boyfriend, Fran for his unlimited patience and emotional support. I just can't thank you enough.

List of Figures

Figure 1-1: Schematic representing a biotinylated microbubble and its binding to receptors on a target surface via biotinylated ligands. The attachment of the ligands to the bubble is achieved through streptavidin linkers. 22

Figure 2-1: The overlapping region between the transmission and reception passband results in unwanted signal detected in harmonic mode. 29

Figure 2-2: Principle of pulse inversion detection using two 3-cycle phase inverted driving pulses p_1 and p_2 of centre frequency 2 MHz. The linear echoes are represented as specular reflectors. The microbubble echoes were simulated using de Jong's bubble model [44] for a bubble of 3 µm in diameter. 30

Figure 2-3: Schematic of one scatterer and the related coordinate system for its velocity measurement. The x axis corresponds to the ultrasound beam acquisition direction. The velocity component measured with the Doppler system is v_x, the projection of the velocity v on the x axis. 33

Figure 2-4: Successive returned echoes of a simulated moving scatterer for a pulsed Doppler system. The y axis represents the slow time axis, sampled at the PRF and the x axis represents fast time. The represented time delay t_s corresponds to the time travelled by the scatterer in between two successive pulses. The time t_x corresponds to the depth of interest the velocity measurement is performed at. 35

Figure 2-5: Quadrature demodulation process. 36

Figure 2-6: Colour Doppler image of my carotid, taken with a L14-38 linear probe of the Sonix RP 500 research scanner (Ultrasonix Medical Corporation, BC, Canada). The image shows the velocity map overlaid onto a B-mode grey scale image. The colour bar on the left hand side shows the velocity range that can be displayed (here from -38 to +38 cm/s). Both the flows moving towards and away from the transducer can be displayed, as shown by the positive or negatives velocity values. A frame rate of 13 frames/s was achieved, as indicated on the right hand side. This rate can be changed by varying parameters, such as the field of view, the depth of imaging, or the number of Doppler pulses sent per line of sight. 38

Figure 2-7: Velocity profiles across a latex tube, 1 cm in diameter. The legend represents the expected maximum velocities for the 4 different flow rates tested. The echoes were originally collected at a sampling rate of 40 MHz. The *I* and *Q* channels were resampled at the lower rate of 4 MHz. The final profiles were smoothened by a median filter of order 20 (function medfilt1 in Matlab) 39

Figure 2-8: Schema representing the protocol for imaging retained microbubbles. After injection of the bolus, the imaging is performed when most of free flowing agents are cleared. Figure adapted from [19]. 42

Figure 2-9: Signal processing steps for the detection of bound agents. F denotes free circulating bubbles, B, bound bubbles and T, tissue. Figure adapted from [29] 42

Figure 2-10: General signal processing steps for the detection of bound agents. F denotes free circulating bubbles, B, bound bubbles and T, tissue. The first nonlinear imaging mode suppressed linear tissue signals, leading to signals from freely flowing and bound bubbles. The slow-time filter then removes the flowing bubbles, resulting in a remaining signal from the bound bubbles. 43

Figure 3-1: Principle of Pulse Subtraction using a two-cycle and a four-cycle driving pulse. The linear echoes are represented as specular reflectors and the nonlinear echoes are simulated echoes from a single microbubble model, based on a modified Rayleigh-Plesset equation. The amplitudes of the echoes are all normalised by considering the maximum between $E\{p_1\}$ and $E\{p_2\}$. 48

Figure 3-2: Experimental setup: Pulse-echo acquisition system for a flow phantom containing either a suspension of SonoVue™ microbubbles, or a control suspension of cellulose particles. 51

Figure 3-3: Measured frequency response of the single element transducers 52

Figure 3-4: Simulated PSD spectra for of a) a linear static scatterer and b) a single static microbubble. Both demodulations were done at the fundamental frequency fo and the driving pressure was of 150 kPa. 53

Figure 3-5: Simulated PSD spectra for of a) a moving linear scatterer and b) a single moving microbubble. Both demodulations were done the at fundamental frequency fo and the driving pressure was 150 kPa. The Doppler frequency fd is also represented on each graph by an arrow. 53

Figure 3-6: Simulated amplitudes of the nonlinear peaks for PSD and PID as a function of the driving pressure for a quadrature demodulation at a) f_0 and b) $2f_0$. The dotted lines represent the two pressures at which PSD was compared to PID in the experiments. 54

Figure 3-7: Pulse subtraction Doppler spectra for: experimental data from a static linear tube reflector (a) and from a static sample of suspension of SonoVue™ microbubbles located in the middle of the tube (b). Both demodulations were done the fundamental frequency f_o and the driving pressure used was of 150 kPa. 55

Figure 3-8: Pulse subtraction Doppler spectra for: experimental data from a flow sample located in the middle of the tube, for linear scattering cellulose particles (a) and a suspension of SonoVue™ microbubbles (b). Both demodulations were done the fundamental frequency f_o and the peak negative driving pressure used was 150 kPa. 55

Figure 3-9: Mean (± standard error of mean) averaged over 40 samples of the CTR for PSD and PID, by demodulating at f_o (a), and at 2 f_o (b) for the two MIs. 56

Figure 4-1: a) Simulated in-phase channel obtained when using a nonlinear Doppler sequence on a linear scatterer moving at a constant velocity. The Doppler signal was calculated based on 128 echoes. Motion was simulated by including a 10 ns time shift between each echo lines. For a PRF set to 10 kHz, the corresponding simulated velocity was of 7.7 $cm.s^{-1}$. b) represents the corresponding Doppler spectrum with one Doppler peak. 66

Figure 4-2: a) Simulated in-phase channel obtained when using a nonlinear Doppler sequence on a simulated single microbubble moving at a constant velocity. The Doppler signal was calculated based on 128 echoes. Motion was simulated by including a 10 ns time shift between each echo lines. For a PRF set to 10 kHz, the corresponding simulated velocity was of 7.7 $cm.s^{-1}$. b) represents the corresponding Doppler spectrum with two Doppler peaks. ... 67

Figure 4-3: a) Total contrast and its decomposition into the three nonlinear harmonics: b) nonlinear fundamental, c) second harmonic and d) third harmonic, as a function of the pulse combination sequence. All the contrast levels were normalised by the highest total contrast obtained. The pulse combination number refers to the pulse sequence number described in Table 4-3. 73

Figure 4-4: PI pulse pair sequence, a) driving pulses, b) echoes and residue, c) pulse parameters, d) frequency spectra of the echoes and the residue. 74

Figure 4-5: PIAMPS pulse pair sequence, a) driving pulses, b) echoes and residue, c) pulse parameters, d) frequency spectra of the echoes and the residue. 75

Figure 4-6: a) Total residue contrast normalised by the transmitted energy, b) the max transmitted pressure, c) the minimum pulse length used and d) the transmitted pulse area..... 76

Figure 4-7: a) Nonlinear fundamental contrast normalised by the transmitted energy, b) the maximum transmitted pressure, c) the minimum pulse length used and d) the transmitted pulse area. 77

Figure 4-8: a) Second harmonic contrast normalised by the transmitted energy, b) the maximum transmitted pressure, c) the minimum pulse length used and d) the transmitted pulse area. . 78

Figure 4-9: a) Third harmonic contrast normalised by the transmitted energy, b) the max transmitted pressure, c) the minimum pulse length used and d) the transmitted pulse area. . 79

Figure 4-10: Variation of the standard deviation (std) of noise in the residue signal as a function of pulse pair combinations. The stds were all normalised in both graphs by the highest noise level. a) represents the noise levels predicted by Equation 4.8 and b) the averaged noise levels calculated over 20 samples from the simulations. 80

Figure 4-11: a) Total CNR and its decomposition into the three nonlinear harmonics b) nonlinear fundamental, c) second harmonic and d) third harmonic. 81

Figure 5-1: Experimental flow phantom which allows an injection of static contrast agents at the upper wall..... 89

Figure 5-2: a) Received echoes from a linear interface for the short pulse p_1 (red dotted line) and long pulse p_2 (green dotted line); b) Residue signal (black line) after subtracting the virtual echo (red dotted line) from the long echo (green dotted line)..... 90

Figure 5-3: Arrangement of the Doppler lines and B-Mode lines in the ultrasound probe. Each beam along one line was fired using 32 elements for transmission and reception. 91

Figure 5-4: a) Schematic representing the latex tube flow phantom and b) its corresponding colour Doppler image constructed as an overlay of a velocity map in red onto a grey scale B-Mode image. The maximum velocity measured was 37 cm/s. 92

Figure 5-5: Grey scale B-Mode images with the velocity map overlaid in red and the nonlinear static scattering amplitude in green. The four tubing cases were represented. In a) no stuck bubbles and no flow, b) stuck bubbles and no flow, c) no stuck bubbles and flow, d) stuck bubbles and flow. The colour maps of the nonlinear scattering have been normalised to the maximum measured nonlinear amplitude. The velocity scale shows the maximum measured velocity. The high velocity values obtained in no flow conditions are due to the velocity estimation with a noise signal and do note represent an actual velocity. 93

Figure 5-6: Experimental setup of the wall-less agar phantom used to target magnetic bubbles to the bottom wall. 97

Figure 5-7: a) Size distribution of the magnetic bubble population, courtesy of Dr Helen Mulvana. The bubbles outside the range 0.5 to 10 μm were excluded. The original data is included in the plot as clear bars. b) A microscopy image of the bubbles X40 at time zero, before the introduction of the magnet. 99

Figure 5-8: Microscopy images showing the response of magnetic bubbles over time to a magnetic field. The magnet was positioned at the top of the microscope slide. 100

Figure 5-9: Frames taken at different time intervals showing the arrival of the magnetic bubbles in the tube and their attachment to the bottom of the tube. a) Diagram of the elements of the video images. b) Cavity before the flow is turned on. c) Bubbles flowing in and deviating

towards the bottom of the tube. d) Bubbles immobilised at the bottom of the tube wall and floating at the top..... 101

Figure 5-10: B-mode images of a square cavity cross-section with their corresponding nonlinear residue images. a) Without magnetic bubbles at an MI of 0.07 and b) with immobilised magnetic bubbles at the bottom of the cavity at the same power. Images c) and d) were done at an MI of 0.35. All the images were plotted with the same grey scale. 101

Figure 5-11: Nonlinear Doppler spectra as a function of depth after PSD processing was applied for a) an empty latex tube and b) the tube containing a solution of static magnetic bubbles. Linear signal is detectable at 0Hz. However in both cases no nonlinear signal is detectable at PRF/2..... 103

Figure 5-12: Biotinylated microbubble and its targeting to a streptavidin coated surface. 105

Figure 5-13: a) Biotinylated bubbles attached to the surface and b) bubbles not attached on the control surface. c) Zoom on the central area of the surface containing attached bubbles. ... 108

Figure 5-14: a) Streptavidin coated area on which attached microbubbles are expected. b) Control area where no bubbles are expected. 109

Figure 5-15: Absorption and emission spectra for DiI dye bound to a phospholipid bilayer membrane. This information was found on the Invitrogen website..... 110

Figure 5-16: Fluorescence microscopy of DiI dye incorporated in the membrane of microbubbles. X63 objective (glycerol immersion)..... 110

Figure 5-17: Attachment of biotinylated bubbles to an agar surface. a) Streptavidin coated surface and b) Control surface..... 111

Figure 6-1: Tensile test principle on a membrane of dimensions w, t, and L (width, thickness and length). ΔL represents the elongation of the sample under the applied force F. 116

Figure 6-2: Picture of the membrane tensile test setup. a) Overall view of the setup, and b) a zoom on a Sylgard sample during testing. 117

Figure 6-3: Load-elongation curves for the three Sylgard membranes prepared with different mixing ratios, ratio 1 (1:10), ratio 2 (1:20) and ratio 3 (1:30). The mean and standard deviation are represented by straight and dotted lines respectively. 117

Figure 6-4: High speed camera setup for the imaging of a single oscillating microbubble floating up against a membrane..... 119

Figure 6-5: High speed camera setup. a) Overall view of the setup, and b) zoom on the Sylgard membrane..... 120

Figure 6-6: Driving pulse used to excite a single microbubble: 0.5 MHz, 12 cycle Gaussian windowed sine wave. The amplitude scale is normalised. 121

Figure 6-7: Radial excursion observation of a single microbubble of initial diameter 9 µm, placed underneath a membrane of stiffness 517 kPa. A series of six pictures taken at different times, corresponding to compressions (pictures c) and e)) or expansions (pictures b) and d)) are represented. The graph in g) represents the corresponding radial excursion of the bubble as a function of time. The maximum excursion of the microbubble is of 1.9 µm in this case. 124

Figure 6-8: High speed camera recording of a single bubble maximal excursion as a function of its initial diameter for bubbles placed under membranes of different stiffness. 125

Figure 6-9: Beam profiles around the focal point of the 0.5 MHz single element transducer. a) Axial profile and b) lateral profile. The FWHM corresponds to 2 cm. 126

Figure 6-10: The maximal radial expansion of a bubble as a function of the equilibrium diameter, predicted using the Rayleigh-Plesset equation for the excitation pulse described by Eq. 3 at f_0 = 0.5 MHz and acoustic pressures p_{ac} = 10, 30, 50, 70 and 100 kPa..... 127

Figure 6-11: The natural frequencies of oscillations of a bubble for an unconfined bubble and for confined bubbles sitting at rigid and free surfaces. 128

List of Tables

Table 4-1: Current contrast agent detection techniques and their pulse design parameters. 63

Table 4-2: Novel contrast agent detection techniques and their pulse design parameters..... 69

Table 4-3: Summary of the nonlinear pulse sequences tested. The amplitudes (a_1, a_2) and pulse lengths (L_1, L_2) indicated in number of cycles are given for the two transmitted pulses p_1 and p_2 respectively. The corresponding transmitted energy (Etrans), peak negative pressure (p^-) and resolution are also provided. 71

Table 6-1: Stiffness of the three samples used for the optical recording..... 118

Abbreviations Used

AM	Amplitude Modulation
AMPS	Amplitude Modulation Pulse Subtraction
BSA	Bovine Serum Albumin
CPS	Contrast Pulse Sequencing
CTN	Contrast to Noise Ratio
CVD	Cardiovascular Diseases
CW	Continuous Wave Doppler
LPF	Low Pass Filter
MI	Mechanical Index
PBS	Phosphate Buffered Saline
PI	Pulse Inversion
PIAM	Pulse Inversion Amplitude Modulation
PIAMPS	Pulse Inversion Pulse Subtraction Amplitude Modulation
PID	Pulse Inversion Doppler
PIPS	Pulse Inversion Pulse Subtraction
PRF	Pulse Repetition Frequency
PS	Pulse Subtraction
PSD	Pulse Subtraction Doppler
PW	Pulsed Wave Doppler
RP	Rayleigh-Plesset
SNR	Signal to Noise Ratio
TI	Thermal Index
VEGF-A	Vascular Endothelial Growth Factor A

Chapter 1 Introduction to ultrasound molecular imaging

1.1 Vascular and perfusion disease processes

Cardiovascular diseases (CVD) and cancer are the main causes of death in the developed countries. CVD accounted for 34.3% of all deaths in 2006 in the United States. An estimated 81 million American adults (more than 1 in 3) have 1 or more types of CVD [1]. High blood pressure, coronary heart disease, heart failure and stroke are amongst the most common CVD. Cancer is the second leading cause of death around the world. The World Health Organization estimates that 84 million people will die of cancer between 2005 and 2015 without intervention. The costs associated to the diseases are high. In 2003, CVD cost the European Union €169 billion [2] and around €350 billion in direct and indirect annual costs in the United States [3]. CVD cost the health care system in the UK around £14.4 billion in 2006. By comparison, the estimated cost of all cancers in the United States is €146.19 billion, according to the World Health Organization.

Both types of diseases take their origins at the molecular level. Atherosclerotic vascular disease can be the source of many clinical conditions, including myocardial infarction (heart attack), chronic stable angina, stroke and peripheral vascular diseases (such as obstruction of arteries). Atherosclerosis is characterised by the formation of lipidic plaques within the walls of large arteries [4], causing the walls to thicken. It was recognised that the process of inflammation fundamentally regulates the phases of atherosclerosis and that the progression and rupture of plaques is governed by molecular and cellular processes [5]. Under inflammatory conditions, leucocytes are recruited and adhere to the endothelial cells at the vessel wall. Their adhesion is mediated by several molecules of the selectins family, including P- and E-selectins expressed on endothelial cells, L-selectins on leukocytes, and other intercellular adhesion molecules such as vascular cell adhesion molecule VCAM-1 [6].

Another example of one of the most widespread categories of disease is cancer, according to the World Health Organization. The development and progression of various tumours is generally associated with the formation of new blood vessels, from pre-existing vessels, a process commonly known as angiogenesis [7]. Vascular

endothelial growth factor A (VEGF-A), is an important angiogenic protein as it induces tumour angiogenesis [8]. VEGF-A is widely expressed by tumour cells and acts through receptors (VEGFR-1, VEGFR-2) that are expressed on the vascular endothelium.

The molecular markers expressed in both atherosclerosis and angiogenesis represent selective targets for imaging and therapy. They would require specific targeted imaging agents, which could preferentially attach to these targets and help identifying them. New developments in cellular and molecular imaging could contribute to earlier diagnosis, more precise disease characterisation and the development of techniques for the delivering and monitoring of drug therapy [4].

Imaging the molecular markers would require signal enhancement through the use of purpose-built contrast agents [4], [9]. The contrast agent must be able to identify the target with high specificity and to bind to it through ligands or peptides. The agent should also possess physical properties that allow its detection via an imaging method. Finally, it should also generate a sufficiently detectable signal within the image to be distinguishable from un-enhanced tissue and present no toxicity for the organism.

As described here, vascularisation plays an important role in the development of atherosclerosis and cancer. As a consequence, a large number of imaging methods are under constant development for the imaging of blood perfusion, such as positron emission tomography (PET), magnetic resonance imaging (MRI), X-ray computed tomography (CT) and ultrasound [10]. Recent findings [11] suggest that ultrasound can not only image the vascular system, but also be used to target molecules of a selected type at the surface of endothelial cells, and finally to deliver medicine at those locations of choice [11].

1.2 Ultrasound imaging and contrast imaging

Ultrasound has a number of advantages over other imaging modalities. It is safe, cheap, widely available and portable. One major advantage over other techniques is that images can be produced at a high frame rate, making it a real-time technique [6].

Ultrasound refers to the sound with frequency higher than 20 kHz, which is greater than the audible frequencies in human hearing. Clinical diagnostic ultrasound scanners use frequencies in the range of 1 MHz to 30 MHz. When a sound wave propagates through tissues, refraction, reflection, scattering and absorption contribute to the attenuation of the wave. The main disadvantage of ultrasound imaging compared to MRI or X-rays is

its limited resolution. To achieve greater penetration, spatial resolution must be compromised. Indeed, low frequency pulses during transmission are less attenuated than higher frequency pulses; however the resolution is directly proportional to the pulse length. Therefore, the choice of an ultrasound imaging frequency for a particular clinical application is a trade-off between resolution and penetration depth, with higher frequencies being used for more superficial structures.

Ultrasound is recognised as the most physiological modality [6], able to measure both structure and function at the same time. Structural information of tissues can be obtained via B-mode imaging. In this mode, ultrasound pulses are transmitted from a transducer along several lines of sight and the intensity of the returning echoes is displayed in different levels of brightness in a grey-scale image. Functional information can be accessed via Doppler ultrasound for example, enabling both the measurement of blood flow and blood perfusion in organs. The following chapter will describe the technicalities of Doppler ultrasound in more detail.

The development of microbubble contrast agents has opened many new ultrasound imaging opportunities. Microbubbles are gas-filled bubbles of 1 to 7 μm in diameter, which are injected intravenously into the patient. They were shown to be very efficient scatterers of ultrasound and backscatter much stronger than regular blood or normal tissue. This is due to the strong gas/blood interface as well as the relative difference in their compressibility and density compared to blood.

When hit by a sinusoidal ultrasound pulse, microbubbles expand and contract in response to pressure variations during the compression and rarefaction phases. Their oscillations are maximal at a particular frequency, their resonance frequency. For microbubbles smaller than 7 μm in diameter these frequencies coincide with the typical frequencies used in diagnostic ultrasound, which makes microbubbles such efficient scatterers.

The interaction of a microbubble in an acoustic field is complex and one can distinguish three regimes in their oscillatory behaviour. At low acoustic pressures, the bubble is considered as a linear scatterer and oscillates symmetrically at the driving frequency. At higher acoustic pressures, the expansion and contraction phases become asymmetrical and the bubble is considered as a nonlinear scatterer, generating harmonics. The echo signal now contains multiple frequencies of the driving frequency. At even higher transmit pressures, the microbubbles exhibit transient nonlinear scattering [72]. For contrast echo studies, the display of a parameter, the mechanical

index (MI) is a useful tool to inform the sonographer about possible microbubble disruptions during the scan [12]. It is related to the peak negative driving pressure and the frequency of the pulse by Equation 1.1 :

$$MI = \frac{p^-}{\sqrt{f_0}} \qquad \text{Equation 1.1}$$

where p^- is the peak negative pressure measured in MPa and f_0 the centre frequency of the driving pulse, measured in MHz.

The nonlinear scattering properties of microbubbles were used as the basis for the development of numerous imaging techniques, separating microbubbles from tissues, usually considered as linear scatterers [13]. A detailed description of the various nonlinear detection techniques will be exposed in the following chapter.

Microbubbles can improve the visualisation of the microcirculation especially with the use of nonlinear imaging techniques. They also boost Doppler signals for a better flow measurement. Although the acoustic spatial resolution is limited, so that individual capillaries can often not be discerned, the microbubbles give rise to signals whose intensity is proportional to the microbubble concentration and thus to the blood volume in that portion of tissue. This has led to new applications of ultrasound. In cardiology for example, the myocardial perfusion can now be measured via novel microbubble quantification techniques [14]. In the liver the microbubble generated contrast allows a clear distinction between benign masses and metastases. In tumours, the neovascular supply can be better studied [13].

Since microbubbles remain in the vasculature, disease processes such as angiogenesis, inflammation or thrombus formation are ideal targets for molecular ultrasound imaging.

1.3 Targeted contrast agents

1.3.1 Targeting strategies

The use of contrast agents for imaging molecular and cellular events has recently been achieved by the development of novel targeted microbubbles that can be retained within diseased organs [6]. Two main strategies are generally used to target microbubbles to regions of disease. The first takes advantage of the chemical and electrostatic properties of the microbubble shell that promotes the non-specific

retention of microbubbles at the target site [11]. The second strategy is more target specific since it relies on the attachment of antibodies, peptides or ligands to the microbubble shell that recognise disease-related antigens [15], [16].

The attachment of microbubbles to disease related receptors has been developed mostly with biotin-streptavidin-mediated techniques [17], as represented with the schematic in Figure 1-1. This approach is useful for pre-clinical experiments. However due to the immunogenicity of most of the available antibodies, these techniques are not yet applicable for the human.

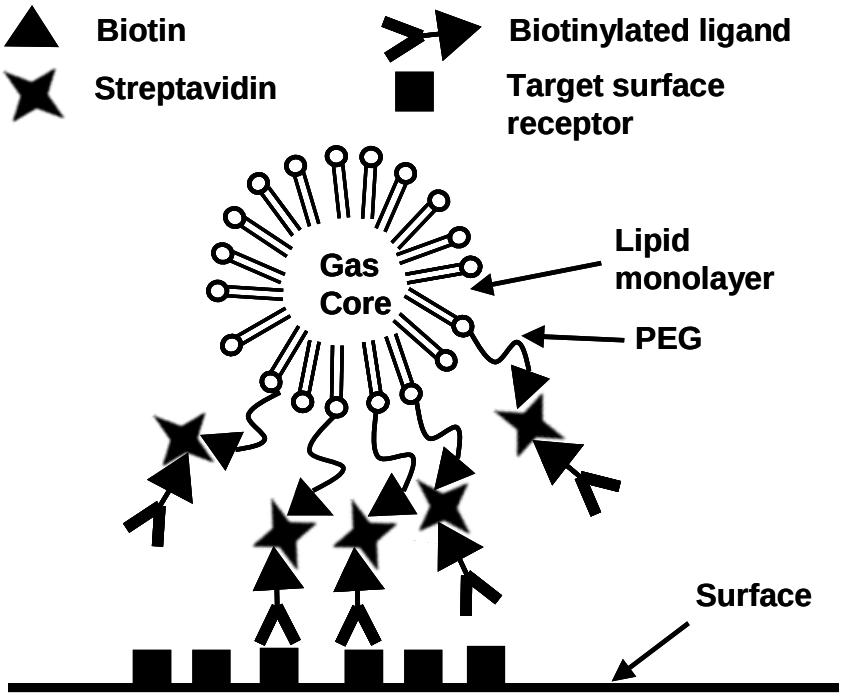

Figure 1-1: Schematic representing a biotinylated microbubble and its binding to receptors on a target surface via biotinylated ligands. The attachment of the ligands to the bubble is achieved through streptavidin linkers.

1.3.2 Molecular imaging applications

Kaufman *et al.* [18] has shown *in vitro* the use of targeted microbubbles for the molecular imaging of VCAM-1 and their capability of rapidly quantifying vascular inflammatory changes that occur in different stages of atherosclerosis. Other inflammatory markers such as E- and P-selectin have been targeted with microbubbles to quantify inflammation in various organs such as the kidneys, the heart and the colon [19], [20], [21]. Several studies have targeted the integrin $\alpha_v\beta_3$, which is known to be required for angiogenesis [22]. Targeting of $\alpha_v\beta_3$ has also been shown to allow the detection of tumor-induced angiogenesis [23]. Another application of targeted microbubbles is to enhance the ultrasonic visualisation of deep venous thrombi. The

use of receptor selective targeted microbubbles improved the binding to blood clots *in vitro* and *in vivo* [24], [25].

1.3.3 Main challenges in ultrasound molecular imaging

Many challenges remain in ultrasound targeted imaging before being used clinically. The adherence of the microbubbles must have high specificity and efficiency. In addition, the density of the bound bubbles at the target as well as their binding strength have to be high enough in order to provide a detectable acoustic signal [26]. Acoustic radiation force has been used in several studies to increase the adhesion of microbubbles, by displacing them to the blood vessel wall [27], [28]. Finally, one main challenge is the discrimination of echoes from adherent microbubbles in the presence of free microbubbles and tissue. The strong echoes from free microbubbles obscure the signal from bound ones and conventional nonlinear imaging techniques cannot separate them [29].

1.3.4 Detection techniques

Several targeted contrast agent detection techniques have been developed to distinguish the attached bubbles form the free flowing ones. Lindner *et al.* [30] proposed an imaging method that first waits for the clearance of free flowing bubbles before acquiring echoes from the retained ones. However, the waiting period required is usually of around 10 minutes, not making it a real time technique. More rapid techniques are based on the combination of a filtering technique which removes signals from flowing agents, with a nonlinear contrast agent detection technique, allowing tissue cancellation [29], [31], [32], [33].

Other approaches suggest the use of the specific acoustic response of targeted microbubbles to directly distinguish them from unbound agents [34], [35], [36]. The various detection techniques will be discussed in more detail in the following chapter.

1.4 Overview of thesis

As underlined in the previous sections, the imaging of targeted contrast agents has many challenges, notably in the discrimination of adherent agents staying static at the wall, from the flowing ones moving with the blood, and from the surrounding tissue.

The aim of this thesis was to study and develop medical imaging and signal processing methods for the detection of static microbubbles at the vessel wall and their discrimination from free flowing ones in the blood stream.

The work is organised following two approaches. Ultrasound imaging is about transmitting signals towards targets, and analysing the backscattered echoes. As such, this thesis first acts on the transmitted pulse sequences, and then aims at understanding the characteristics and specificity of the targets, with the ultimate goal of developing specific transmission sequences to maximise the response from the target. Here, since flow is one of the main differences between adherent and free flowing bubbles it was hypothesised that Doppler and its nonlinear version, pulse inversion Doppler (PID), could be used to separate moving from non moving nonlinear scatterers and at the same time reject tissue signals. The second approach of this thesis consisted in studying the oscillatory response of a bubble in contact with an elastic surface. A better understanding of the differences with free flowing bubbles could lead to the development of methods for the selective detection of targeted microbubbles.

In order to apprehend the work presented here, it is necessary to be familiar with the fundamentals of ultrasound contrast agents imaging and the principles of ultrasound Doppler. These are presented briefly in chapter 2. First, the background on nonlinear microbubble contrast imaging is presented and the current contrast agent detection modalities are described. Then microbubble oscillation models are described, with the focus on the de Jong's model, which will be used throughout the thesis. A review of Doppler ultrasound techniques is then presented with the description of signal processing methods for velocity estimation. Finally, a technical review of the current methods used for detecting targeted microbubbles is presented, as well as their limitations.

In chapter 3 a new nonlinear Doppler technique, pulse subtraction Doppler (PSD), is presented and compared with pulse inversion Doppler. PSD was tested in a simulation study using a single microbubble model, as well as in flow experiments and was shown

to differentiate moving from non-moving and linear from nonlinear scattering. Since targeted microbubbles are static and nonlinear scatterers, this technique is a good candidate for their detection.

This study served as a starting point for the derivation of a generalised nonlinear Doppler, described in chapter 4. It is based on combined linear pulse pair sequences and was tested in a simulation study. The response from a single microbubble was simulated for different pulse combinations and the pulse sequences were compared with regards to criteria specific to imaging requirements. It was shown that depending on the imaging system capabilities and clinical applications, certain pulse combinations could offer alternatives to the current imaging modalities. Furthermore, the proposed approach is directly applicable in a strict non linear imaging approach, without Doppler processing.

Chapter 5 describes a series of two flow phantom experiments on which the pulse subtraction Doppler sequences were tested.
First, an *in vitro* flow phantom was designed in order to assess pulse subtraction Doppler for the detection and discrimination of static nonlinear microbubbles in the presence of free flowing ones. It was shown that the technique enables such discrimination and the practicability for *in vivo* situations is discussed.
Then the nonlinear Doppler sequences were tested on a phantom containing magnetic bubbles. It was shown that the magnetic bubbles could be immobilised through a magnetic field to a specific region of interest under flow conditions. The acoustic properties of the bubbles were also studied. Finally, chapter 5 describes some preliminary work with biotinylated bubbles and their attachment to different streptavidin coated surfaces.

The behaviour of microbubbles against a membrane of varying stiffness was also studied through high speed camera observations and is presented in chapter 6. It was found both experimentally and by comparison to theoretical modelling that within the stiffness range of human blood vessels the change in acoustical behaviour of microbubbles is negligible.

Chapter 7 concludes this research by reminding and summarising the achievements, and by proposing new perspectives of research which seem to be opened here.

Chapter 2 Theory of contrast and targeted imaging

The physics of ultrasound contrast agents is of complex nature and many aspects and parameters need to be taken into account in order to describe the behaviour of microbubbles realistically. This chapter aims at summarising the key elements which are needed to understand this thesis. It focuses first on ultrasound contrast agents, their modelling and their most common detection techniques. Doppler ultrasound imaging and signal processing methods for the estimation of blood flow velocity are then described. Finally, a detailed technical review of the current methods used for detecting targeted microbubbles is presented.

2.1 Contrast enhanced imaging

Modelling of ultrasound contrast agents is a useful tool for better understanding and predicting their nonlinear behaviour in the presence of an acoustic field. Predicting their response to different excitation pulses can lead to the development of new detection techniques and the improvement of current ones [37]. This process can ultimately lead to an enhancement of the contrast to tissue ratio of the image and therefore also increase the diagnostic potential. At the same time, acoustic experiments are also needed to compare and validate the results as well as to improve the models. In this section the main ultrasound contrast modalities will also be exposed.

2.1.1 Microbubble modelling

2.1.1.1 Rayleigh-Plesset equation

In 1917, Lord Rayleigh [38] laid the foundations of analytical bubbles oscillation models, by describing the problem of a vapour-filled cavity collapsing in a liquid when subject to a steady external pressure field. The presence of surface tension was then taken into account by Plesset in 1949 [39] for a vapour-filled bubble. He also introduced a first description of bubble dynamics by modelling forced radial oscillations of bubbles immersed in an external variable acoustical field. The description of gas-filed bubbles [40] and the addition of the effect of viscosity [41], lead to the Rayleigh-Plesset-Noltingk-Neppiras-Poritsky (RPNNP) equation commonly known as the “Rayleigh-Plesset equation”. Energy losses tend to reduce the oscillations of the bubble and damping was added to the equation of motion by Prosperetti [42] and

Leighton [43]. Typically energy losses through radiation, viscous forces and thermal conduction contribute to the damping.

In order to stabilise ultrasound contrast agents and increase their lifespan against dissolution in the surrounding liquid, most of the microbubbles are encapsulated by a shell made of materials such as phospholipids, albumin or polymers. The first contrast agent theoretical model was proposed by De Jong *et al.* in 1994 [44] and described the equation of motion of an encapsulated microbubble. Two parameters, the shell elasticity S_p and the shell friction S_f model the influence of the coating and were estimated by fitting calculated transmission and scattering values to linear scattering measurements for Albunex microspheres. The equation of motion is given by Equation 2.1

$$\rho_l(R\ddot{R}+\frac{3}{2}\dot{R}^2)=(p_0+\frac{2\sigma}{R_0}-p_v)(\frac{R_0}{R})^{3\kappa}+p_v-\frac{2\sigma}{R} \\ -2S_p(\frac{1}{R_0}-\frac{1}{R})-\delta_t\omega\rho_l R\dot{R}-p_0-P(t) \qquad \text{Equation 2.1}$$

R = instantaneous bubble radius (m)

$\dot{R}$ = first time derivative of the radius (m.s^{-1})

$\ddot{R}$ = second time derivative of the radius (m.s^{-2})

ρ_l = density of the surrounding liquid (kg.m^{-3})

R_0 = initial bubble radius (m)

p_{go} = initial gas pressure inside the bubble (Pa)

κ = polytropic exponent of the gas (-)

p_v = vapour pressure (Pa)

p_o = ambient pressure (Pa)

σ = surface tension coefficient (N.m^{-1})

δ_t = damping coefficient (-)

ω = angular frequency of incident acoustic field (rad.s^{-1})

$P(t)$ = time varying acoustic pressure (Pa)

Many other models of encapsulated bubbles were then developed based on this model, such as the models from Church [45], who described the bubble encapsulation as an elastic solid and accounted for the thickness and viscoelastic properties of the shell in the Raileigh-Plesset model. Hoff *et al.* [46], determined the viscoelastic parameters of the shell of the model by Church, in the limit of small shell-thickness in

comparison with the bubble diameter. Another example of bubble modelling was developed by Marmottant *et al.* [47] who developed a model of phospholipid coated bubbles at large amplitudes, which enabled the prediction of compression-only behaviour of the bubble. Many models were not mentioned here, however a good overview of most of the existing models can be found in Marcia Emmer's thesis [48].

2.1.1.2 Polynomial expansion model

The harmonic content of the response of a microbubble can also be predicted via the model developed by Haider and Chia [49], who modelled the nonlinear echo signal from microbubbles as a polynomial expansion of the transmitted waveform. As shown in Equation 2.2, the echo signal E{p(t)} can be expressed as a function of p(t), the transmitted pulse.

$$E\{p(t)\} = a_1 p(t) + a_2 p(t)^2 + \ldots + a_N p(t)^N = \sum_{n=1}^{N} a_n p(t)^n \qquad \text{Equation 2.2}$$

where the a_n coefficients represent the contributions of the nonlinear components to the echo signal. For a linear system, only a_1 is non null. When considering a transmitted sinusoidal pulse of centre frequency f_0, it was shown by [49] that odd harmonic nonlinearities generate harmonic components at odd multiples of f_0 and even nonlinearity components generate even harmonics. The third component for example contributes to the nonlinear fundamental, located at f_0.

Although simple, this model was shown to be useful in predicting the harmonic content of microbubble echoes, in response to different excitation pulses. This model helped explaining some of the most common ultrasound contrast imaging modalities [50], [51].

2.1.2 Ultrasound Contrast agent imaging modalities

2.1.2.1 Harmonic imaging

Almost all clinical applications of ultrasound contrast agents rely on, and are limited by, the ability to detect microbubbles in the presence of tissue. Due to their strong scattering, the contrast agents were first imaged at their driving pulse centre frequency [52], creating images of greater clarity. However the detectability of the bubbles within tissue was limited and new detection methods were developed, which were based on their nonlinear behaviour and their ability to generate harmonics. Second harmonic

imaging [53] was one of the first contrast agent imaging modalities. In harmonic detection, ultrasound is transmitted into the body at one frequency, f_o, the fundamental frequency, and the received echoes are filtered at the second harmonic, $2f_o$. Since tissue is generally considered as a linear scatterer, the echoes arising from tissue are mainly centred at the transmitted fundamental frequency and are therefore suppressed during the high-pass filtering. However harmonic detection involves an inherent trade-off between contrast and imaging resolution, as represented in Figure 2-1.

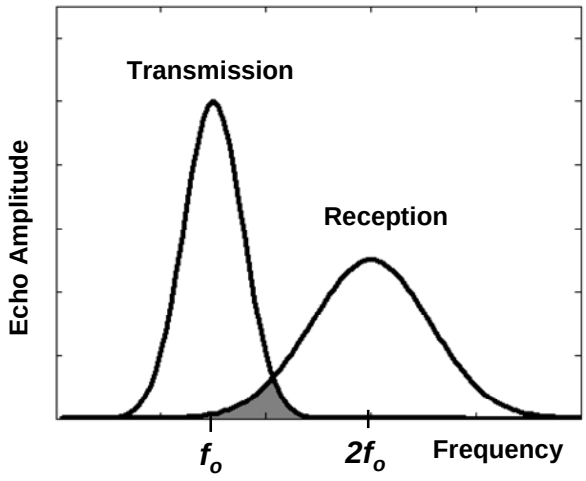

Figure 2-1: The overlapping region between the transmission and reception passband results in unwanted signal detected in harmonic mode.

If the transmit pulse passband and the receive passband overlap, the linear echoes from tissue will be detected in the harmonic signal. Such echoes reduce the contrast to tissue ratio (CTR) and can mask the nonlinear echoes from small quantities of agent, especially at low incident intensities when nonlinear scattering is weak. To increase the contrast, transmit and receive bandwidths must be narrowed, by using longer transmission pulses and therefore reducing the axial resolution. This trade-off particularly affects the imaging of small vessels, in situations in which the concentrations of agent is limited or at low incident sound intensities [50].

2.1.2.2 Pulse inversion imaging

Pulse inversion, developed by Simpson *et al.* [50] overcomes the contrast resolution trade-off of the harmonic imaging technique. This method relies on the asymmetric oscillation of an ultrasound bubble in an acoustic field and enables a detection of a nonlinear signal over the entire bandwidth of the transducer [50]. In pulse inversion imaging, two pulses p_1 and p_2 are sent in rapid succession into the tissue. The second pulse is a 180º phase shifted version of the first pulse, as shown in Equation 2.3.

$$p_1(t) = -p_2(t)$$ Equation 2.3

The scanner detects the echoes E_1 and E_2 from theses two pulses and forms their sum R.

$$R(t) = E_1(t) + E_2(t)$$ Equation 2.4

For ordinary tissue, which behaves in a linear manner, the sum of the echoes produced by the two inverted pulses is zero. On the other hand, for an echo with nonlinear components, such as that from a microbubble, the echoes produced will not be simple images of each other and their sum is not null. Thus this technique, as illustrated in Figure 2-2, suppresses tissue signal and enables the detection of contrast agents. The harmonic content of the residue can be deduced from the polynomial expansion model [49]. Since the driving pulses have inverted phases, this will affect the phases of the echo harmonics. It can be seen that the odd harmonics cancel and the even harmonics add up [50]. The latter are the terms which will contribute to the nonlinear residue signal.

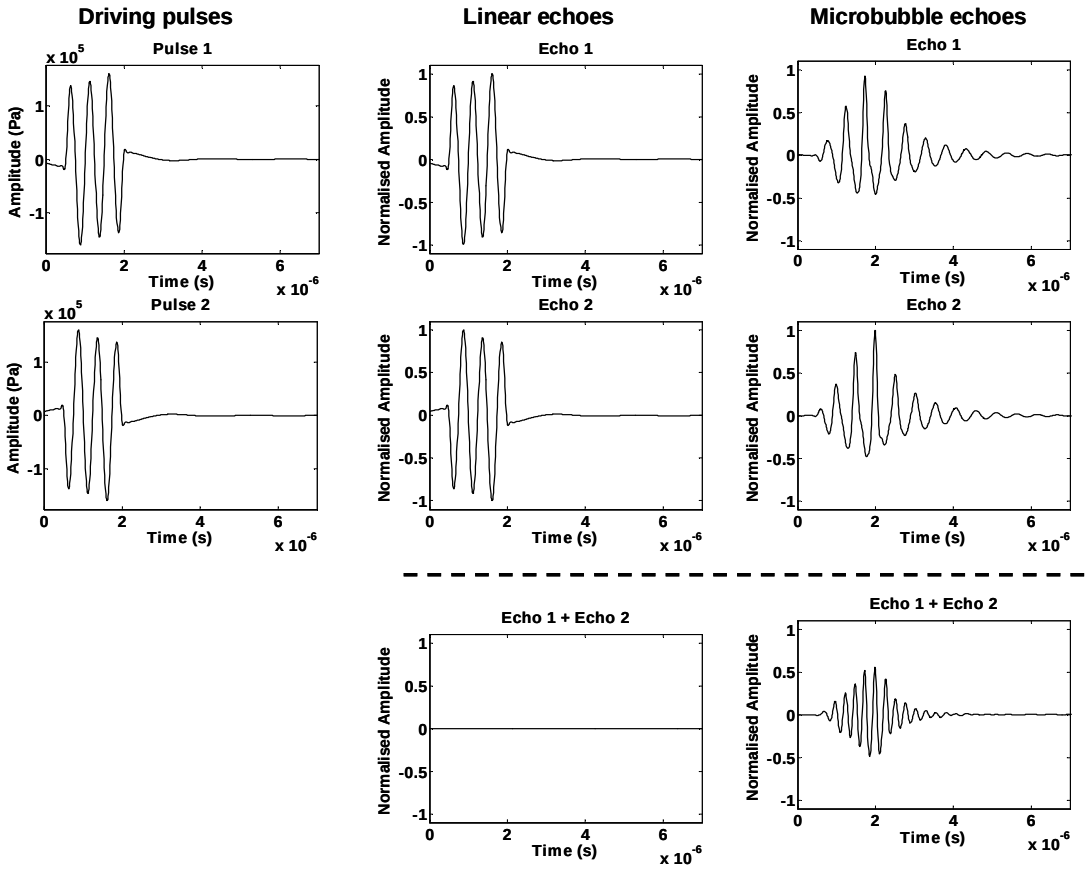

Figure 2-2: Principle of pulse inversion detection using two 3-cycle phase inverted driving pulses p_1 and p_2 of centre frequency 2 MHz. The linear echoes are represented as specular reflectors. The microbubble echoes were simulated using de Jong's bubble model [44] for a bubble of 3 μm in diameter.

2.1.2.3 Other multipulse sequences

Harmonic imaging and pulse inversion rely mainly on the detection of second harmonic signal in the echoes and do not extract nonlinear signal within the fundamental frequency band. As it was first suggested by Haider and Chia [49], transmitting pulses of different amplitudes and phase can enable the extraction of odd order nonlinearities. Since odd orders also contribute to the nonlinear fundamental, the latter could easily be detected with low attenuation within the transducer bandwidth.

Amplitude modulation (AM) [54], also referred to as power modulation, enables the detection of the nonlinear fundamental as well as the second harmonic component from the microbubbles. AM consists in transmitting two pulses, the second pulse, p_2 having usually an amplitude of half the amplitude of the first pulse, p_1 as shown in Equation 2.5.

$$p_1(t) = 2p_2(t) \qquad \text{Equation 2.5}$$

After echo reception, the differences in driving pulse amplitudes can be compensated in order to cancel linear scattering after subtraction of both echoes, as shown in Equation 2.6.

$$R(t) = E_1(t) - 2E_2(t) \qquad \text{Equation 2.6}$$

Pulse inversion amplitude modulation (PIAM) [51] combines both phase inversion and amplitude modulation and was shown to enhance the contrast compared to PI or AM alone.

$$p_1(t) = -2p_2(t) \qquad \text{Equation 2.7}$$

$$R(t) = E_1(t) - 2E_2(t) \qquad \text{Equation 2.8}$$

Also based on the combination of phase and amplitude, cadence contrast pulse sequencing (CPS) [55] was shown to allow an increase of the CTR. CPS is based on the successive transmission of three pulses p_1, p_2 and p_3 of different amplitude and phase, as shown in Equation 2.9. Their echoes are then recombined for tissue suppression, as shown in Equation 2.10.

$$2p_1(t) = -p_2(t) = 2p_3(t) \qquad \text{Equation 2.9}$$

$$R(t) = 2E_1(t) - E_2(t) + 2E_3(t)$$ Equation 2.10

Another multipulse approach proposed by [56] and referred to as pulse subtraction time delay imaging, uses pulses of different length to extract nonlinearities.

The main advantage of these multipulse sequences over harmonic imaging is that they work over the entire echo bandwidth and hence allow an improved image resolution. They also enable the extraction of different nonlinear harmonic components, increasing therefore the CTR. These techniques have been shown to perform at low pressure levels, which prolongs the lifetimes of the microbubbles [50]. This can also limit clutter signals caused by nonlinear propagation of ultrasound through tissue. However, these contrast modalities are limited in the case of tissue motion. The decorrelation of two successive echoes due to scatter movement affects tissue cancellation and tissue signal will be detected as nonlinear scatterers, deteriorating the CTR. Tissue cancellation can be improved in such case by the use of multipulse sequences transmitting more than two pulses [55].

2.2 Velocity imaging in medical ultrasound imaging

The advent of ultrasound contrast agents, has increased the intensity of Doppler flow signals from blood [57] and greatly improved the detection of small vessels [58], [59]. This section focuses on Doppler velocity detection techniques as well as their combination with contrast imaging.

2.2.1 Continuous wave and pulsed wave Doppler

The first continuous wave (CW) Doppler experiment was developed in the 50s by Satomura [60], who demonstrated that ultrasound could be used to detect cardiac motion. Since then, blood flow assessment through Doppler has become common practice in many diagnostic ultrasound exams. In a diagnostic ultrasound scan the Doppler effect occurs when sound is reflected from moving scatterers. For a pulse transmitted at a central frequency f_0, the received signal will be shifted by a frequency f_d, proportional to the scatterer velocity v, following the Doppler Equation 2.11.

$$f_d = \frac{2vf_0\cos(\theta)}{c}$$ Equation 2.11

where *c* is the speed of sound and θ the angle of the ultrasound beam with the blood vessel. Figure 2-3 represents a schematic of one scatterer and its related coordinate system for its velocity measurement.

The main advantage of CW Doppler is its ability to measure high velocities accurately. However as it continuously transmits and receives from different transducers it does not allow resolving velocities as a function of depth and the Doppler shift measured arises from all the red blood cells along the ultrasound beam.

This disadvantage was overcome by the development of pulsed wave (PW) Doppler systems. These use a transducer which alternates the transmission and reception of ultrasound, and therefore allowing depth discrimination. In pulsed Doppler, N identical pulses are transmitted along one line of sight at a pulse repetition frequency (PRF) and the echoes detected for processing.

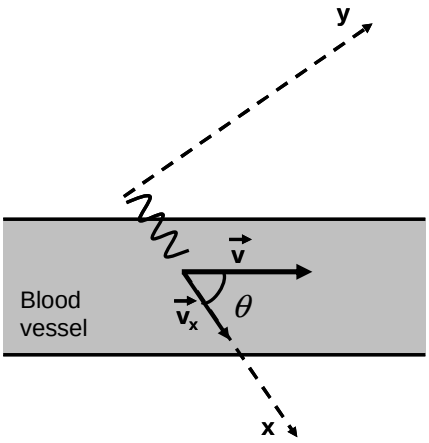

Figure 2-3: Schematic of one scatterer and the related coordinate system for its velocity measurement. The x axis corresponds to the ultrasound beam acquisition direction. The velocity component measured with the Doppler system is v_x, the projection of the velocity v on the x axis.

The transmitted pulses take the form of sinusoids *p*(*t*), of envelope *g(t)* and centre frequency f_0, as shown in Equation 2.12.

$$p(t) = g(t)\sin(2\pi f_0 t) \qquad \text{Equation 2.12}$$

The first echo received *e*(*1,t*) of a scatterer moving at a velocity *v* and located at an initial distance *d* is given by Equation 2.13:

$$e(1,t) = g'(t - t_0)\sin(2\pi f_0 (t - t_0)) \qquad \text{Equation 2.13}$$

where

$$t_0 = \frac{2d}{c}$$ Equation 2.14

where *g'(t)* denotes the difference in envelope compared to the driving pulse.
Assuming that the scatterer moves at a constant velocity, it will have moved by a distance d_x between each ultrasound pulse, and the k^{th} echo will take the form

$$e(k,t) = g'(t - t_0 - kt_s)\sin(2\pi f_0(t - t_0 - kt_s))$$ Equation 2.15

where t_s is the time delay observed between the successive echoes due to the scatterer movement. This delay is proportional to the travelled distance d_x and the velocity v_x, along the direction of the ultrasound acquisition, as shown by Equation 2.16.

$$t_s = \frac{2d_x}{c} = \frac{2v_xT}{c}$$ Equation 2.16

where *T* is the time interval between two pulses (*T=1/PRF*)
The axial velocity v_x of a moving scatterer can therefore be expressed in terms of the time difference t_s between successive echoes Equation 2.17.

$$v_x = \frac{ct_s}{2T}$$ Equation 2.17

In order to derive the velocity at a depth of interest, the echo measurements are taken at the corresponding to time t_x, relative to the pulse emission time *t*. This process is represented in Figure 2-4.

$$\begin{aligned} e(k,t_x) &= g'(t_x - t_0 - kt_s)\sin(2\pi f_0(t_x - t_0 - kt_s)) \\ &= g'(t_x - t_0 - kt_s)\sin(-2\pi f_0 kt_s + \Phi_x) \\ \Phi_x &= 2\pi f_0(t_x - t_0) \end{aligned}$$ Equation 2.18

Each echo leads to one sample of the Doppler signal *e(k)* at a particular depth d_x and the sampled Doppler signal can be written as:

$$e(k) = g'(t_x - t_0 - kt_s)\sin(-2\pi\frac{2v_xT}{c}f_0k + \Phi_x)$$ Equation 2.19

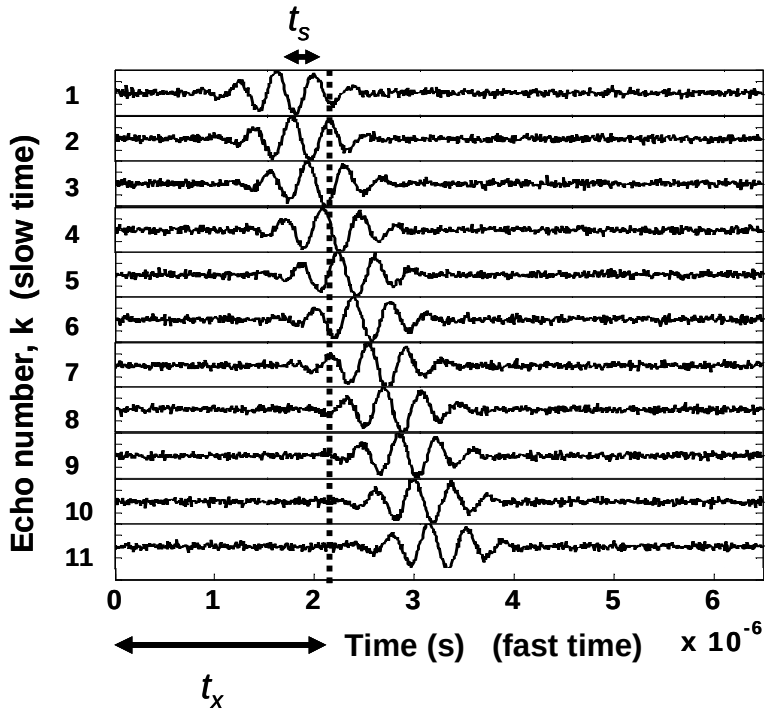

Figure 2-4: Successive returned echoes of a simulated moving scatterer for a pulsed Doppler system. The y axis represents the slow time axis, sampled at the PRF and the x axis represents fast time. The represented time delay t_s corresponds to the time travelled by the scatterer in between two successive pulses. The time t_x corresponds to the depth of interest the velocity measurement is performed at.

Several velocity estimation techniques are available in Doppler imaging and they are usually classified in two categories: time shift and phase shift estimation techniques, usually based on Equation 2.11 or Equation 2.17 respectively.

2.2.2 Velocity estimation techniques

Several time-shift and phase shift velocity estimation techniques exist and are described by Evans *et al.* [61]. In this section the most common techniques will be described.

2.2.2.1 Time shift estimation techniques

Also denoted as wideband imaging techniques, they consist in estimating the time delay between successive echoes and to derive the velocity, using Equation 2.16. Estimating t_s can be done by tracking patterns between successive echoes by means of cross-correlations. The search for similar patterns can be performed along different search windows, in order to estimate the velocity as a function of depth. Bonnefous *et al.* [62] presented for the first time this method, which was then tested by Embree *et al.* [63].

2.2.2.2 Phase shift estimation techniques

Quadrature demodulation

In order to extract the relative phase change between successive echoes, several methods exist. One common process known as quadrature demodulation consists in removing the carrier frequency from the echoes, as represented in the schematic of Figure 2-5. Each echo is first multiplied with reference signals $\cos(2\pi f_0 t)$ and $\sin(2\pi f_0 t)$ of frequency the transmission frequency f_0. The signals obtained are then low pass filtered (LPF) in order to remove high frequency components. This process extracts a complex envelope of each echo signal, made of an in-phase component *I(k,t)* and a quadrature component *Q(k,t)* as shown in Equation 2.20.

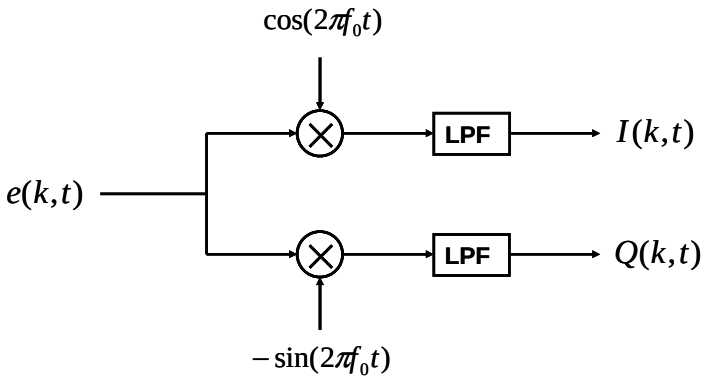

Figure 2-5: Quadrature demodulation process.

$$I(k,t) = g''(t - t_0 - kt_s)\sin(\varphi(k))$$
$$Q(k,t) = g''(t - t_0 - kt_s)\cos(\varphi(k))$$
$$\text{where } \varphi(k) = 2\pi f_0(t_0 - kt_s) = \varphi_0 - 2\pi\frac{2v_x T}{c} f_0 k$$

Equation 2.20

$\varphi(k)$ being independent of *t*, φ_0 a constant and g'' denoting the change in envelope, due to the filtering in the demodulation process.

At this stage the direction of blood flow can be determined by comparing the phases of the *I(k,t)* and *Q(k,t)* signals. If the phase of *I(k,t)* is 90° ahead of the phase of *Q(k,t)*, then flow is directed towards the transducer, and in the inverse situation the flow is reversed.

A complex envelope *E(k,t)* can be formed with the two in-phase and quadrature components. At a depth of interest corresponding to the time t_x, a sampled complex Doppler signal *E(k)* can be calculated:

$$E(k) = I(k,t_x) + iQ(k,t_x) = g''(t_x - t_0 - k\frac{2v_xT}{c}).e^{-i2\pi f_d kT} \quad \text{Equation 2.21}$$

This signal is made of the product of a slow-time varying envelope g'' with a complex sinusoid of frequency f_d, proportional to v_x.

Taking the Fourier transform of *E(k)* leads to a Doppler spectrum, representing the Doppler frequencies at a particular depth, related to the distribution of scatterer velocities. As the Doppler signal is sampled at the PRF, the measured frequency shifts need to satisfy the Nyquist limit [64]:

$$f_{d,\max} < PRF/2 \quad \text{Equation 2.22}$$

where $f_{d,max}$ is the maximum measurable frequency shift.

Phase estimator

Although the fast Fourier transform is the most common Doppler spectrum analysis technique, the majority of methods implemented in scanners are based on parameter estimators. In practice most of them are based on the autocorrelation method, first described by Kasai [65] which estimates the mean angular frequency $\bar{\omega}$ from the first moment of the power spectrum *P(ω). P(ω)* is related to the autocorrelation $R(\tau)$ by the Wiener-Khinchine's theorem:

$$R(\tau) = \int_{-\infty}^{+\infty} P(\omega)e^{j\omega\tau}d\omega \quad \text{Equation 2.23}$$

Kasai showed that an estimate of the mean angular frequency $\bar{\omega}$ of a Doppler signal can be approximated by Equation 2.24.

$$\bar{\omega} = \frac{\varphi(t)}{T} \quad \text{Equation 2.24}$$

where $\varphi(t)$ is the argument of the autocorrelation and *T* the time interval between two successive pulses. The mean velocity can finally be calculated using Equation 2.11.

This technique is computationally faster and more accurate than using the Fourier transform and requires only a few samples. The precision on the estimation is given by the number of pulses transmitted for one line.

2.2.3 Colour flow imaging

For a two-dimensional representation of the blood flow, colour Doppler images are usually created. For such images the velocities are estimated along several lines of sight and colour coded [64]. The velocity map is then overlaid on a conventional grey scale B-mode image, as shown in Figure 2-6 for example. Usually, the colours red and blue are used to represent the flow directions toward or away from the transducer. The power of the returned Doppler signal can also be displayed in a 2-dimensional colour image, commonly known as power Doppler [66]. In this mode, the colour map displays the integrated power of the Doppler signal which is related to the number of red blood cells creating the Doppler frequency shift. This technique has shown an improved sensitivity to flow; it however does not provide any flow velocity or direction information.

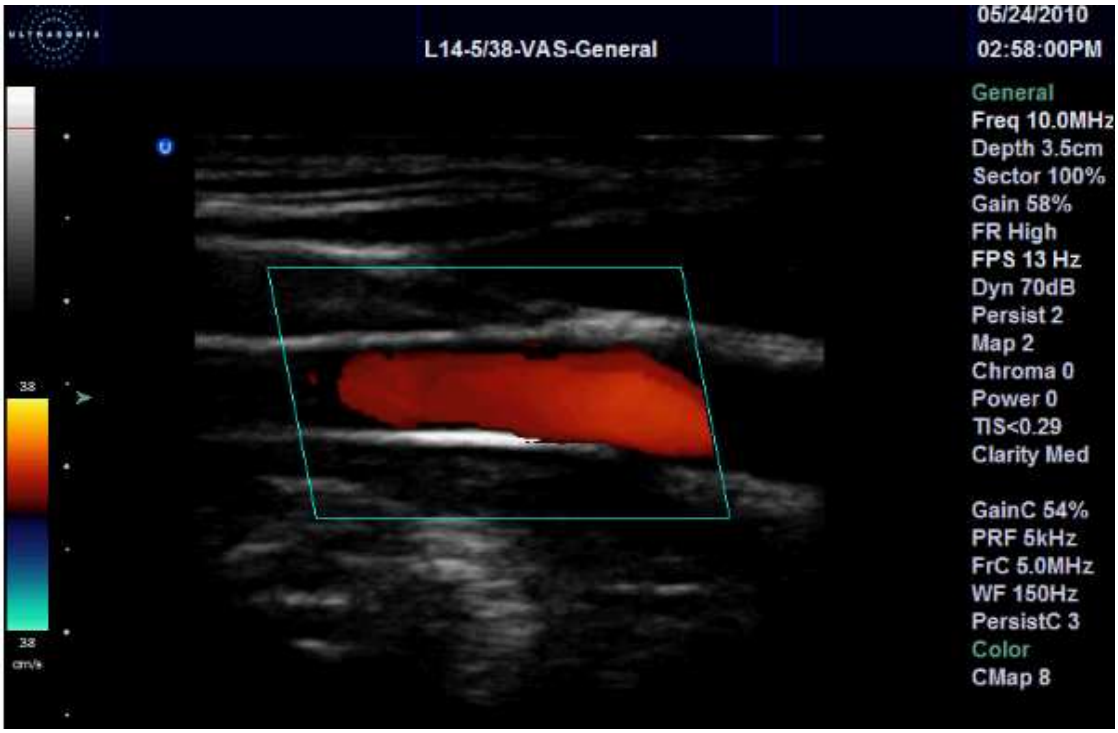

Figure 2-6: Colour Doppler image of my carotid, taken with a L14-38 linear probe of the Sonix RP 500 research scanner (Ultrasonix Medical Corporation, BC, Canada). The image shows the velocity map overlaid onto a B-mode grey scale image. The colour bar on the left hand side shows the velocity range that can be displayed (here from -38 to +38 cm/s). Both the flows moving towards and away from the transducer can be displayed, as shown by the positive or negatives velocity values. A frame rate of 13 frames/s was achieved, as indicated on the right hand side. This rate can be changed by varying parameters, such as the field of view, the depth of imaging, or the number of Doppler pulses sent per line of sight.

In practice, for one line of sight, all the *N* echoes are collected for processing [67] and are first band-pass filtered in order to remove electronic noise. Quadrature demodulation is applied to the echoes. The calculated *I* and *Q* signals are then resampled at a lower sampling frequency and complex envelopes are calculated. The Doppler signal is then constructed by collecting one sample at a particular depth of interest t_x for each of the *N* envelopes. This process is repeated for all the different depths along the line. A windowed Fourier transform is then applied to each Doppler signal in order to obtain Doppler spectra. The frequency shift corresponding to the highest measured Doppler frequency peak in each spectrum can be plotted as a function of the axial distance. This frequency is directly related to the velocity of the flow, as shown by Equation 2.11.

As an illustration of the above described theory, the pulsed Doppler process was here applied on a flow phantom. Four different flow rates were tested: 0 cm/s, 7 cm/s, 17.5 cm/s and 35 cm/s, corresponding to the maximum velocity expected. Pulsed Doppler was programmed on a Sonix RP research scanner and the collected echoes were post-processed via Matlab™. The four velocity profiles calculated along one line of sight across a latex tube are represented on Figure 2-7.

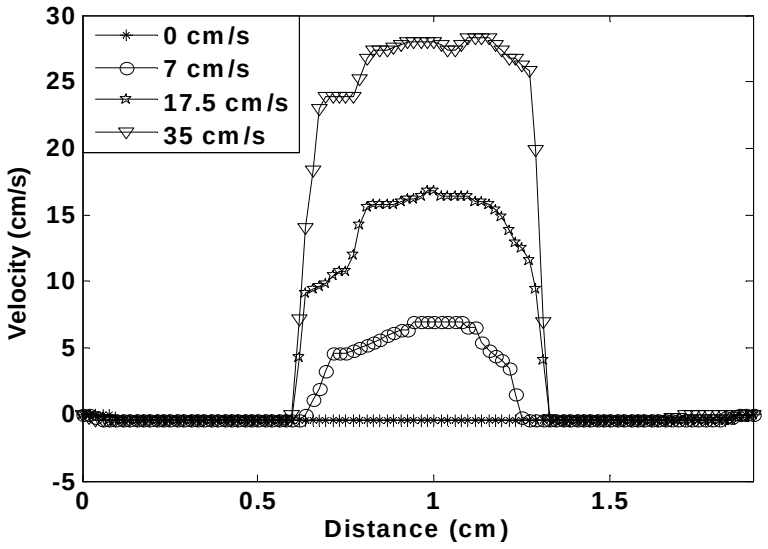

Figure 2-7: Velocity profiles across a latex tube, 1 cm in diameter. The legend represents the expected maximum velocities for the 4 different flow rates tested. The echoes were originally collected at a sampling rate of 40 MHz. The *I* and *Q* channels were resampled at the lower rate of 4 MHz. The final profiles were smoothened by a median filter of order 20 (function medfilt1 in Matlab).

In this example it can be observed (Figure 2-7) that the lower velocities of the flow near the vessel wall were not estimated. This is a common limitation of the Doppler

technique since the high signal from the stationary wall can mask the one from slower moving scatterers. In practice high pass filters can be applied to the Doppler signals in order to remove this clutter signal. The filtering will however also remove echoes from slowly moving scatterers.

2.2.4 Nonlinear Doppler

2.2.4.1 Harmonic Doppler

It was shown that in the presence of contrast agents, power Doppler could be combined with harmonic imaging by demodulating the received echoes at the second harmonic component of the transmitted frequency [68], [69]. This technique enables a better clutter rejection since the echoes arising from tissue contain little harmonics. A comparison with conventional power Doppler showed that harmonic Doppler was better adapted for slow flow imaging and produced less clutter signals [70].

2.2.4.2 Pulse inversion Doppler

In pulse inversion Doppler, the transmitted pulses are inverted copies of each other and successive pulses are transmitted into the tissue at a PRF as for pulsed Doppler. After echo reception either conventional or harmonic Doppler processing [50] is performed. Doppler shifts arising from linear scattering and nonlinear scattering are then separated into two different regions in the resulting Doppler spectra. Using a polynomial expansion model to simulate the response of a microbubble, it was shown that the odd harmonic components of the microbubble echo, as well as linear tissue signal, have a Doppler shift $f_{d,odd}$, as shown in Equation 2.25.

$$f_{d,odd} = \frac{2v}{c} f_0 + \frac{PRF}{2} \qquad \text{Equation 2.25}$$

Echoes originating from even harmonics were shown to have a Doppler shift $f_{d,even}$, as shown in Equation 2.26.

$$f_{d,even} = \frac{2v}{c} f_0 \qquad \text{Equation 2.26}$$

Pulse inversion Doppler was shown to have the advantage over conventional harmonic Doppler to function over the entire bandwidth, achieving a better resolution and to work at low driving pressures.

2.3 Targeted contrast agent detection techniques

One of the current problems in ultrasound molecular imaging with targeted contrast agents is to selectively detect and separate the attached microbubbles from all the other signals. The latter are mainly originating from freely circulating agents or tissue and noise. The research behind the detection of the attached agents has taken two directions which are interconnected. The first is based on a better understanding of the differences in the acoustic properties between attached agents and free agents. Knowledge in this area could be exploited in the second area, in the development of selective imaging methods for the detection and discrimination of the attached bubbles. The following paragraphs will review the latest advances in both areas.

2.3.1 Targeted contrast agent acoustic behaviour

Optical and acoustical observations showed differences in the behaviour of targeted bubbles against free bubbles. Optical high speed camera observations have shown microbubbles in contact to a wall to oscillate asymmetrically in the plane normal to the surface and symmetrically in the plane parallel to the surface [36]. The same optical observation was done with microbubbles attached to a surface. The bound bubbles were also shown to have a smaller maximum expansion than free bubbles [71]. By means of optical tweezers, bubbles placed adjacent to a rigid wall were shown to have a 50% decrease in their oscillation amplitude compared to the same bubble away from the boundary [34]. Acoustical observations have shown adherent contrast agents to scatter a high amplitude at the fundamental frequency and to have a different frequency content compared to free agents. This observation was attributed to different effects: the vicinity of the wall causing an expected shift in the resonant frequency of the bubble [72] as well as the viscous boundary layer at the wall contributing to the damping of the oscillations [35].

A better understanding of the differences in behaviour between free and attached bubbles such as differences in resonant frequency or amplitude could help improving their specific detection techniques.

2.3.2 Signal processing techniques

One of the first solutions for imaging targeted microbubbles, Figure 2-8, is to wait for the clearance of the freely flowing agents before imaging the attached ones [73].

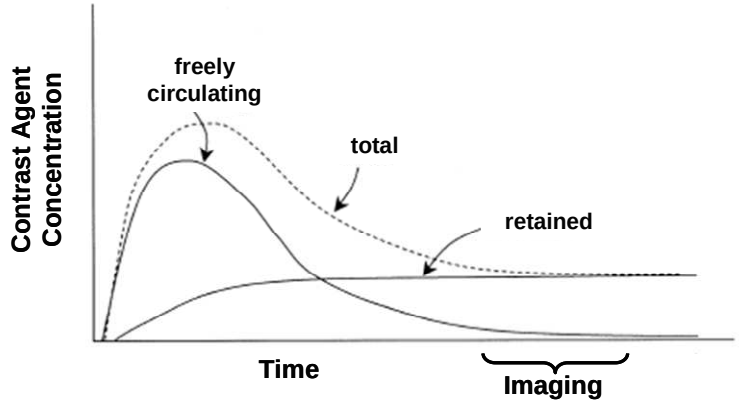

Figure 2-8: Schema representing the protocol for imaging retained microbubbles. After injection of the bolus, the imaging is performed when most of free flowing agents are cleared. Figure adapted from [19].

However imaging cannot be performed so long as the unbound bubbles remain in circulation. This process can require a waiting period of several minutes, which can lead to a loss of bubbles due to gas diffusion and therefore a reduction in scattering.

One method named “image-push-image” [29] allows a more rapid imaging of the targeted bubbles. It is based on an image subtraction process described in Figure 2-9. Adherent microbubbles are first attached to a surface by means of a series of radiation force pulses. Several images are taken before and after bubble attachment. Before radiation force the images contain signals from free flowing bubbles and tissue (F+T), and after radiation force they contain free flowing bubbles, attached bubbles and tissue (F+B+T), as shown in Figure 2-9. Averaging the received echoes over multiples pulses was shown to suppress the flowing agent signal and act as a slow-time low-pass filter [29]. Therefore estimates of the tissue signal only and of the tissue and bound bubbles could be taken. Subtracting both images leads to an image of attached bubbles only. The main limitation of this technique is its performance in the case of tissue motion since it is based on signal subtraction.

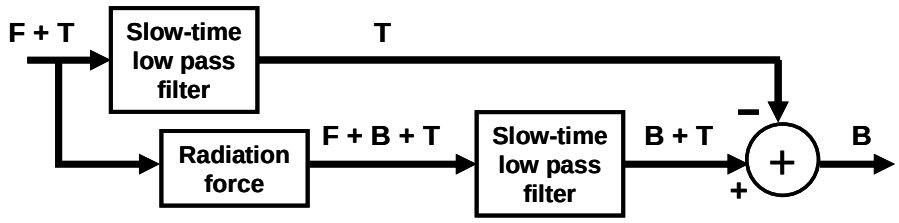

Figure 2-9: Signal processing steps for the detection of bound agents. F denotes free circulating bubbles, B, bound bubbles and T, tissue. Figure adapted from [29].

A second technique was proposed by [29] which is based on a combination of filters in order to remove tissue and freely flowing bubble signals. The technique does not require radiation force; however the targeted bubbles need to be bound before it can be applied. A series of B-mode images are first recorded. A fast time high pass filter is then used to remove tissue signals. This filter acts as a harmonic filter in order to reject linear tissue signals and keep the harmonic signals from the free and bound bubbles. This process is then followed by a slow-time low pass filter which averages several images in order to suppress the signal of flowing microbubbles and therefore leaving the signal of the bound bubbles.

This technique operates in fast time and therefore is less affected by tissue motion than the previous one. However the main drawback is the suppression of the fundamental signal arising from the attached bubbles during the first high pass filtering, leading to a weaker signal from the targeted bubbles. Referred to as the “harmonic” method [29], this technique belongs to a more general signal processing method, described by the schematic in Figure 2-10.

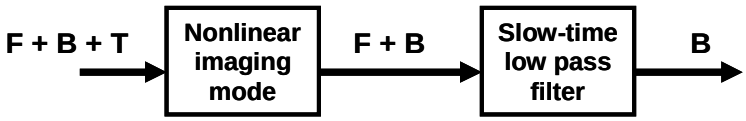

Figure 2-10: General signal processing steps for the detection of bound agents. F denotes free circulating bubbles, B, bound bubbles and T, tissue. The first nonlinear imaging mode suppresses linear tissue signals, leading to signals from freely flowing and bound bubbles. The slow-time filter then removes the flowing bubbles, resulting in a remaining signal from the bound bubbles.

Harmonic filtering can be replaced by other contrast imaging modes in order to improve the signal received from the targeted bubbles. Pulse inversion was used by Patil *et al.* [31] in combination with slow-time averaging for flowing bubble signal cancellation. These pulses were sent alternatively with radiation force pulses used to push the bubbles to the vessel wall in order to increase their attachment rate. As shown by Needles *et al.* [32] subharmonic imaging can also be used as a nonlinear imaging method for tissue discrimination, also in combination with radiation force pulses. Hu *et al.* [33] used of a new ultrasound array which also enabled the separation of adherent bubble echoes from flowing ones and tissue. Their nonlinear imaging mode was based on the transmission of low centre frequency pulses and echo reception at a high centre frequency (TLRH). This technique is based on the detection of higher order harmonics from the adherent bubbles and suppresses tissue signals including nonlinear tissue harmonics.

2.4 Summary

The detection of targeted contrast agents implies an understanding of the scattering behaviour of microbubbles. Indeed, their distinction from tissue is based on their nonlinear scattering properties in contrast to the generally linear properties of tissues. It was therefore necessary to introduce or remind their most common detection modalities. Furthermore, by definition, targeted contrast agents are adherent to the vessel walls and do not flow. This characteristic has been used for the development of the current targeted microbubble detection techniques, which were reviewed here. These techniques are mostly based on the succession of a slow time filter which rejects moving agents and a nonlinear contrast agent modality which cancels tissue signals. However no technique has been developed yet which makes use simultaneously of the movement information and the nonlinear behaviour of the contrast agents. The area of flow imaging was therefore also presented and signal processing methods were described for velocity estimation. Combining Doppler imaging with a nonlinear contrast modality could possibly allow the separation of targeted microbubbles from free flowing ones and tissue.

Chapter 3 Pulse subtraction Doppler[1]

3.1 Introduction

Microbubbles are ultrasound contrast agents characterised by their ability to backscatter a large signal from blood in a nonlinear manner. Most types of microbubbles take the form of gas encapsulated by a shell for stability, suspended in a saline solution to allow intravenous administration. To date, their main clinical applications include the enhancement of echoes from the blood pool, the imaging of blood perfusion in tissue and the assessment of blood flow using traditional Doppler ultrasound [74].

Harmonic Doppler [53] and pulse inversion Doppler (PID) [50] make use of the nonlinear properties of the microbubbles to differentiate between moving tissue and microbubbles. PID enables the use of the full transducer bandwidth in order to detect echoes at the fundamental frequency (f_0) originating from microbubbles and tissue, as well as higher order harmonics from microbubbles only. This technique overcomes the limitations of harmonic Doppler in which a trade-off between contrast and image resolution is necessary [50].

In PID, a series of N pulses is sent at the pulse repetition frequency (PRF), with each pulse being an inverted copy of the previous one. This causes the signals from linear and nonlinear moving scatterers to be represented in different frequency bands in the calculated Doppler spectrum. The Doppler shifts due to the scattered odd harmonics such as the f_0 and the 3rd harmonics ($3f_0$) are represented in the [-PRF/2 -PRF/4]U[PRF/4 PRF/2] region and the Doppler shifts due to the even harmonics are represented in the remaining region: [-PRF/4 PRF/4], provided that a revised Nyquist limit, $f_{d,max}$ < PRF/4, is satisfied for the scatterer velocities, where $f_{d,max}$ represents the maximum detectable Doppler shift [50]. Nonlinear scatterers give rise to an additional

[1] Three publications resulted from this work:

V. Mahue, J. M. Mari, R. J. Eckersley, and M. X. Tang, "Comparison of Pulse Subtraction Doppler and Pulse Inversion Doppler," IEEE Transactions on Ultrasonics Ferroelectrics and Frequency Control, vol. 58, pp. 73 - 81, 2011.
V. Mahue, J. M. Mari, R. Eckersley, and M.-X. Tang, "Comparison of Pulse Subtraction Doppler and Pulse Inversion Doppler," in IEEE International Ultrasonics Symposium, Rome, Italy, 2009, pp. ref. P1-A-02.
V. Mahue, J. M. Mari, R. J. Eckersley, C. G. Caro, and M. X. Tang, "Pulse subtraction Doppler," in International Congress on Ultrasonics, Proceedings, Amsterdam, 2009, pp. 749-753.

peak in the PID Doppler spectrum. This is due to the fact that while neighbouring linear echoes alter their phase by 180 degrees due to the phase alternation of the driving pulses, some part of the nonlinear signal does not alter its phase at all.

One of the limitations of PID is that the transducer bandwidth needs to be broad enough to detect both the fundamental frequency and the higher order harmonics. In addition, in PID, the nonlinear part of the Doppler spectrum is only due to even harmonics, and therefore in most cases restricted to the second harmonics ($2f_0$). By detecting both odd and even order components in multipulse sequences, more nonlinear energy could be preserved and could improve the sensitivity to nonlinear scatterers. This approach has been exploited by Eckersley *et al.* [51], Phillips *et al.* [55] and Shen *et al.* [75], where pulse inversion (PI) and amplitude modulation (AM) [54] are combined to achieve an enhancement of nonlinear signal.

In this chapter the use of a novel imaging sequence, pulse subtraction Doppler (PSD) is presented and compared with PID.

3.2 Theory

PSD is related to the pulse subtraction time delay imaging technique, a contrast agent detection method introduced by Borsboom *et al.* [56] and Shi *et al*. [76]. Borsboom showed that the pulse subtraction method enables to distinguish linear from nonlinear scattering. It is based on a sequence of three pulses that cancel each others when two of the pulses are subtracted from the third pulse. When applied to the detection of contrast agents, these pulse sequences cancel tissue signal.

3.2.1 Pulse subtraction principle

This three pulse sequence developed by Boorsboom can also be simplified into a two pulse sequence [56]. Pulse subtraction, as it will be used in this study is based on the following multipulse sequence: A first short pulse p_1 of length T is followed by a second longer pulse p_2. p_2 is formed by concatenating N time-shifted copies of the shorter pulse p_1, as shown in Equation 3.1. An example pair of pulses is shown in Figure 1-1.

$$\begin{cases} p_1(t) \\ p_2(t) = \sum_{n=1}^{N} p_1(t - nT) \end{cases} \qquad \text{Equation 3.1}$$

$$\begin{cases} E\{p_1\} \\ E\{p_2\} = E\left\{\sum_{n=1}^{N} p_1(t-nT)\right\} \\ E_V = \sum_{n=1}^{N} E\{p_1\}(t-nT) \end{cases}$$

Equation 3.2

The echo received from pulse p_2, E{p_2} can be expressed as the echo received by N time shifted versions of p_1. A “virtual” echo E_V is then constructed from E{p_1}, as expressed in Equation 3.2. For a linear system the echo E{p_2} will be the same as E_V.

Figure 3-1 displays examples of the three echoes for linear and nonlinear systems. For purely linear responses, E{p_2} and E_V are identical and therefore their difference is zero. For a nonlinear system, such as microbubble contrast agents, a signal will remain after subtraction. This is because microbubbles exhibit different phase responses when exposed to excitations of different lengths [56], [77]. Thus after the virtual pulse construction the phase of the linear superposition of the shorter echo is different from the phase of the long echo, after the first partition. The signal residuals after subtraction, for both linear and nonlinear scatterers, are represented at the bottom of Figure 3-1.

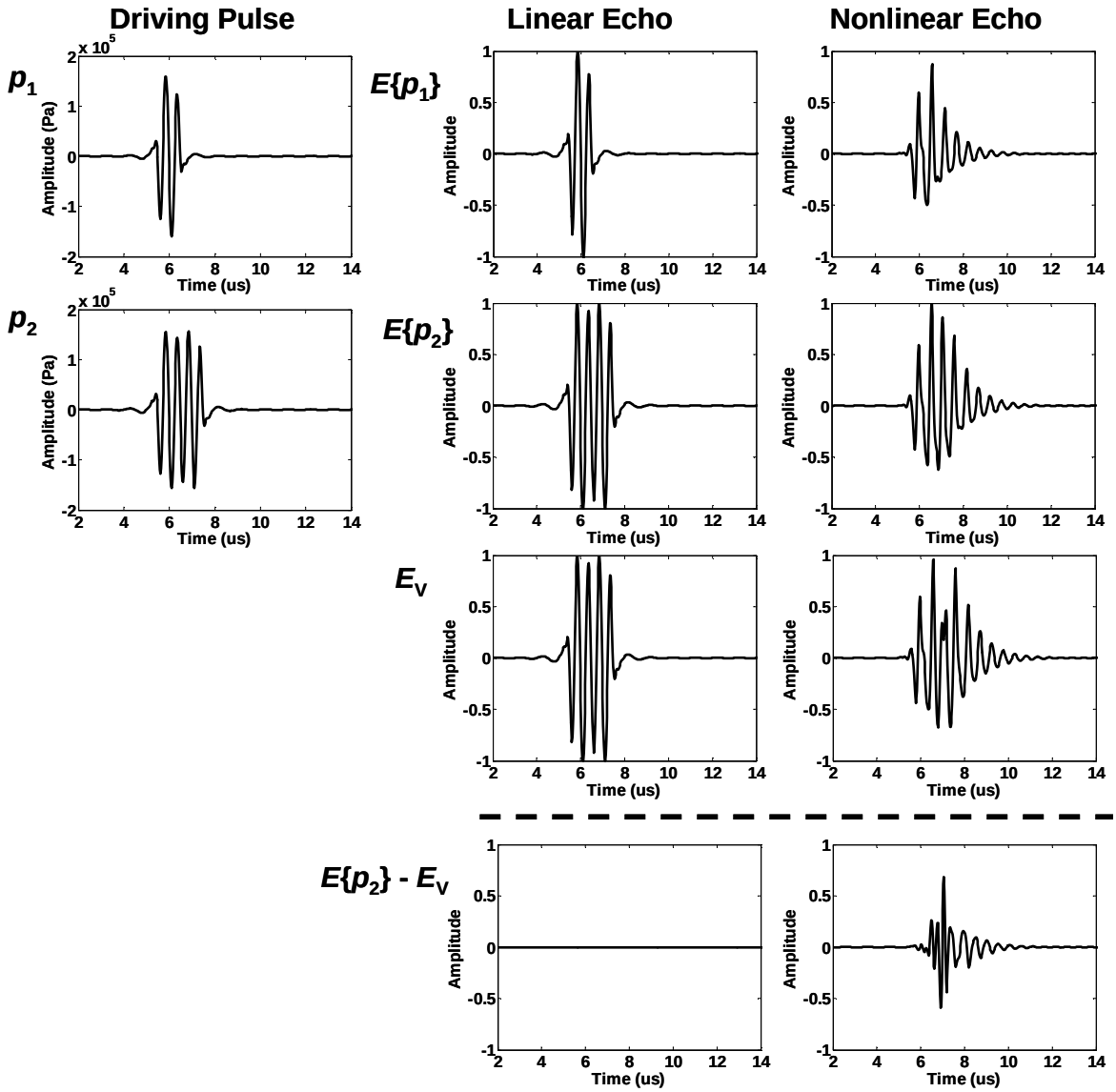

Figure 3-1: Principle of Pulse Subtraction using a two-cycle and a four-cycle driving pulse. The linear echoes are represented as specular reflectors and the nonlinear echoes are simulated echoes from a single microbubble model, based on a modified Rayleigh-Plesset equation. The amplitudes of the echoes are all normalised by considering the maximum between $E\{p_1\}$ and $E\{p_2\}$.

3.2.2 Pulse subtraction Doppler principle

For pulse subtraction Doppler, a series of N pulses is sent along a single line of sight, alternating between p_1 and p_2 with a fixed PRF. Before conventional Doppler processing is applied, each short echo is transformed into a virtual echo by the process described above in Equation 3.2. Echoes resulting from linear scatterers will be equivalent to normal pulsed Doppler echoes. For a non-moving linear target, all the lines will be identical. However, for nonlinear scatterers, the differences in the scattering of successive pulses will introduce additional information in the Doppler spectrum. For a linear scatterer, the Doppler spectrum is expected to have one peak,

contained in the region [-PRF/4 PRF/4] and for a nonlinear scatterer the Doppler spectrum is expected to have an additional peak in the [-PRF/2 -PRF/4] U [PRF/4 PRF/2] region. This repartition of the linear and nonlinear peaks is inverted to the one in PID, as the transmitted pulses in PSD have all the same phase. As for PID, the maximum detectable Doppler shift for PSD is also limited by the revised Nyquist frequency of PRF/4. As for PID, the nonlinear peak contains nonlinear signals only and the linear peak contains linear as well as nonlinear signal. Each frequency band then presents the properties of standard Doppler spectrum. For example the presence of scatterers with different velocities will broaden the peaks in their respective bands.

A series of simulations and experiments were carried out to demonstrate the validity of the new technique and to compare it with PID.

3.3 Methods

3.3.1 Simulations

A simulation study was conducted to assess pulse subtraction Doppler as a technique for separating linear from nonlinear moving or non moving scatterers. A modified Rayleigh-Plesset (RP) equation based on de Jong's constant thickness model [44] was used to simulate the acoustic response to the Doppler pulse sequences of a microbubble, 3 µm in diameter and with shell properties similar to SonoVue^{TM} (shell friction and elasticity parameters: 0.45 10−6 kg.s^{-1} and 1.1 N.m^{-1}, respectively [78]), located at a distance of 5 cm. The Matlab code used is shown in the Appendix.

PSD and PID pulses were compared on the basis of equal resolution. The transmitted Doppler pulse sequences for PSD consisted of 32 driving pulses, alternating between one short 2 cycle sine wave (p_1) and one long 4 cycle sine wave (p_2). Both pulses had a centre frequency, f_0, of 2 MHz, corresponding to the microbubble resonant frequency, and a peak-negative pressure of 140 kPa, corresponding to a mechanical index (MI) of 0.1. Doppler echoes of a linear scatterer, modelled as a specular reflector being a direct copy of the transmitted pulse, were also simulated as control. To simulate the flow condition for both linear and nonlinear scatterers, the successive echoes were time-shifted by 33 ns, equivalent to a target velocity of 20 cm/s for a PRF of 8 kHz.

A second simulation was performed to compare PSD with PID. Echo signals for both techniques were generated with the RP equation, and an analysis of their Doppler spectra was performed for acoustic pressures ranging from 20 kPa to 150 kPa in steps

of 20 kPa, corresponding to an MI ranging from 0.01 to 0.11. The transmitted pulse sequences for PID used the same microbubble properties and pulse parameters as for PSD, except that the adjacent pulses were inverted copies of each other and their length was kept at 4 cycles. These pulse length parameters ensured that for the linear control simulation, the echo pairs arising from PSD and PID contained the same amount of energy. The pulses and the simulated echoes were band-pass-filtered using a custom filter (0.5-7 MHz 5 pole Butterworth) in order to simulate a broadband transducer of central frequency at 3.5 MHz.

The simulated Doppler echoes were post-processed with Matlab™ (The Mathworks Inc., Natick, MA).Using the same parameters as in the construction of p_2, virtual echoes were reconstructed from the short pulse transmission echoes. The construction of virtual echoes was applied to a whole Doppler line, by adding a time-shifted version of the short pulse echo line to the received short pulse echo line, in order to match the length of the long pulse echoes. Quadrature demodulation was then applied to both the 16 virtual echoes and the 16 long pulse transmission echoes. Finally complex Doppler signals sampled at the PRF were calculated. Quadrature demodulation was performed following two methods: by mixing the received echoes with a carrier at the driving pulse frequency on the one hand, and at the second harmonic frequency of the driving pulse on the other hand. The Doppler signals were then processed through a fast Fourier transform to obtain Doppler spectra for the two different types of scatterers. The amplitude of the nonlinear part of the Doppler spectrum, indicative of bubble-only scattering, was computed for PSD and PID. The peak amplitude of the nonlinear part of the Doppler spectrum is denoted the “nonlinear peak” and was used for the comparison of both techniques.

3.3.2 Experiments

In vitro experiments were performed in order to assess PSD as a technique for separating linear from nonlinear scatterers, in static and flow conditions, and PSD was compared to PID. A steady flow phantom was prepared from which Doppler data was acquired using a pulse-echo acquisition system (Figure 3-2). Doppler pulse sequences were designed and uploaded via GPIB interface to an arbitrary waveform generator (AWG32250, Agilent, Santa Clara, CA). They were amplified by an RF power amplifier (model A075, ENI, Rochester, NY) to drive a 3.5 MHz single element transducer focussed at 7.5 cm (Videoscan V380, Panametrics, Olympus, Waltham, MA). A thin latex tube of 9 mm in diameter (0.2 mm wall thickness), containing flowing or static SonoVue™ (Bracco Research, Switzerland) contrast agents (concentration: 200 µL/L),

was positioned in a water bath. The centre of the tube was located at 7.5 cm from the transducer. Echo signals were then acquired by a second V380 transducer, positioned confocally with the transmit transducer, amplified (model 5800, Olympus, Waltham, MA), recorded on an oscilloscope (DPO 4032, Tektronix, Beaverton, OR) with 8-bit precision, and transferred to a computer via USB interface for processing. A control suspension of cellulose particles (Sigmacell Type 20, Sigma-Aldrich Co.) was used as a linearly scattering fluid (10 g/L). Both fluids were pumped out (Eheim Universal Rotary Pump, model 1048) of a glass container and the flow velocity was adjusted via a flowmeter (flow rate range: 200-3000 mL/min, EW-32458-42, Cole-Parmer, Hanwell, London) to 900 cm^3/min.

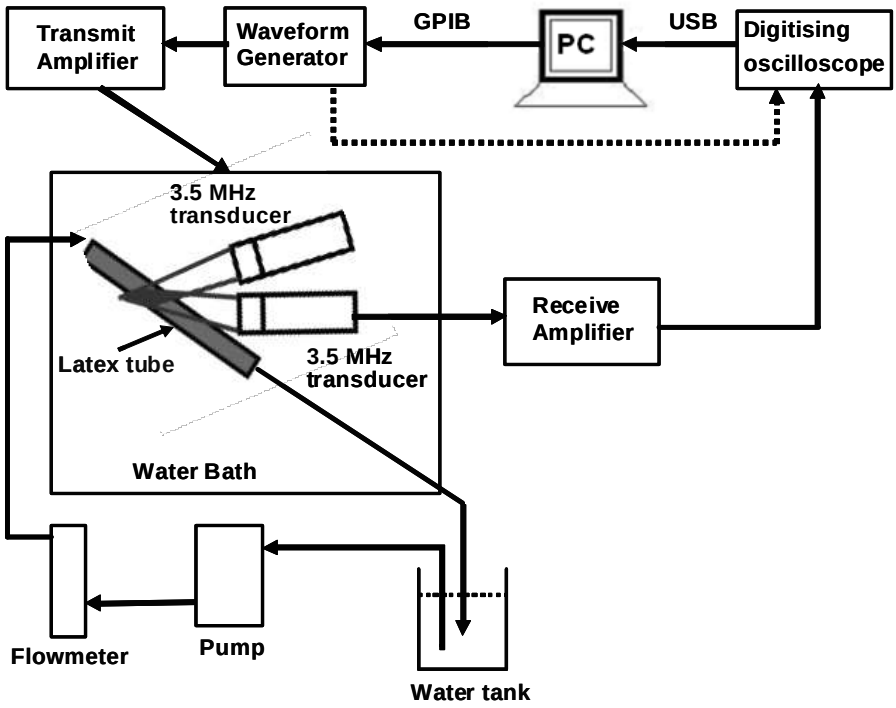

Figure 3-2: Experimental setup: Pulse-echo acquisition system for a flow phantom containing either a suspension of SonoVue™ microbubbles, or a control suspension of cellulose particles.

In order to characterise both single element transducers, their acoustic pressure waveforms in response to an impulse excitation were recorded with a calibrated needle hydrophone (0.5 mm Precision Acoustics LTD, Dorchester, UK) positioned at the focus and processed with Matlab™. The power spectrum obtained is shown in Figure 3-3 and was used to determine the characteristics of the filter implemented in the simulations. The acoustic pressure and therefore the MI at the focus of the transducers were also calibrated using the hydrophone by sending out a four cycle long sine wave.

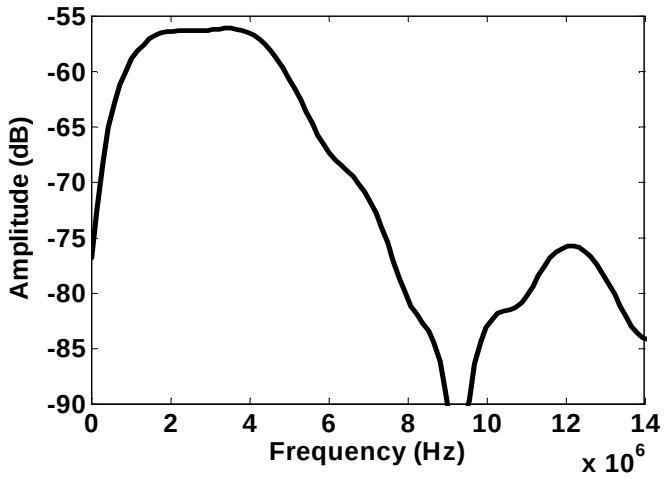

Figure 3-3: Measured frequency response of the single element transducers.

The driving pulses had the following parameters: for PSD, the transmitted pulses were two and four cycles long, and for PID all pulses were four cycles long. The centre frequency of the pulses for both techniques was 2 MHz, and the peak negative pressures used were 71 kPa and 141 kPa, corresponding to MIs of 0.05 and 0.1 respectively. These pulse parameters belong to the range of clinically used parameters for contrast imaging with regards to frequency, intensity and duration. Each Doppler pulse sequence consisted of 32 driving pulses with a PRF of 8 kHz. The number of 32 echoes recorded, was due to the limited memory size of the oscilloscope. For each Doppler technique, a total of 40 repeated acquisitions were recorded for further statistical analysis.

The Doppler echoes received from a sample volume at the centre of the tube as well as from the tube wall were post-processed with Matlab^{TM} in the same way as for the simulations. The quantity used for comparison was the contrast to tissue ratio (CTR). It was defined as the ratio of the spectrum amplitude at the nonlinear peak frequency in the Doppler spectrum of a contrast agent suspension divided by the amplitude at the same frequency of the spectrum for a cellulose particle suspension.

3.4 Results

3.4.1 Simulations

The following Figure 3-4 shows the simulated Doppler spectra obtained with a linear a) or nonlinear b) scatterer using a PSD pulse sequence in a static case. Only one peak was obtained for a linear scatterer, centred at 0 Hz (Figure 3-4 a) and an additional

peak located at PRF/2 was obtained for a nonlinear scatterer (Figure 3-4 b). In the case of a simulated moving linear scatterer, one peak was centred in the [-PRF/4 PRF/4] range, at the Doppler frequency f_d (Figure 3-5 a). This confirms that pulse subtraction Doppler is able to detect moving linear scatterers, in a way similar to traditional pulsed Doppler. In the case of a simulated moving nonlinear scatter, one additional peak, due to the nonlinear response of the scatterer, was located in the remaining region of the spectrum (Figure 3-5 b). This Doppler frequency was measured as 533 Hz, and therefore equivalent to a flow of velocity 20 $cm.s^{-1}$ (Figure 3-4 a), which is the value expected. This result demonstrates that PSD is able to discriminate nonlinear from linear moving scatterers, because, provided that f_d < PRF/4, their responses appear in different frequency bands of the Doppler spectrum.

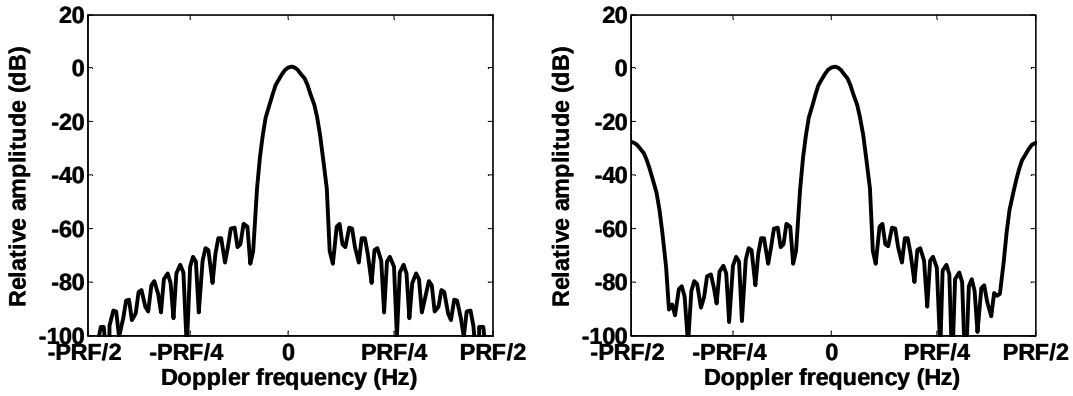

Figure 3-4: Simulated PSD spectra for of a) a linear static scatterer and b) a single static microbubble. Both demodulations were done at the fundamental frequency f_o and the driving pressure was of 150 kPa.

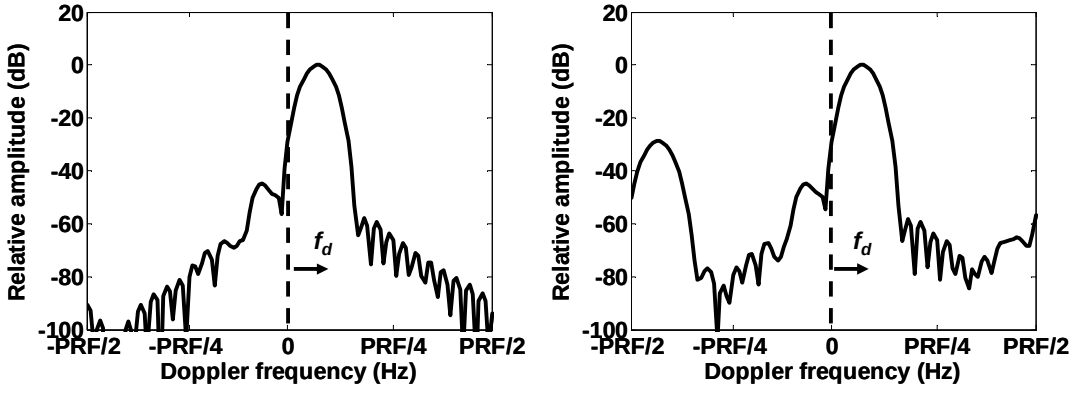

Figure 3-5: Simulated PSD spectra for of a) a moving linear scatterer and b) a single moving microbubble. Both demodulations were done the at fundamental frequency f_o and the driving pressure was 150 kPa. The Doppler frequency f_d is also represented on each graph by an arrow.

Figure 3-6 a) and b) show the simulated amplitudes of the nonlinear peaks in the PSD and PID spectra as a function of the incident peak negative pressure at 2 MHz, for two different demodulation frequencies. It can be seen that both PSD and PID amplitude increases with incident acoustic pressure. When quadrature demodulated at f_o PSD produces a higher nonlinear peak than PID over the entire pressure range. Using quadrature demodulation at $2f_o$, PID presents higher nonlinear peak amplitudes compared to PSD, as shown in Figure 3-6 b). In this case, PID enables a better detection of nonlinear scattering versus PSD in terms of harmonic detection and has a CTR which is higher than the one achieved by PSD at f_o demodulation. The difference in vertical scale in the two graphs is significant and should be noted.

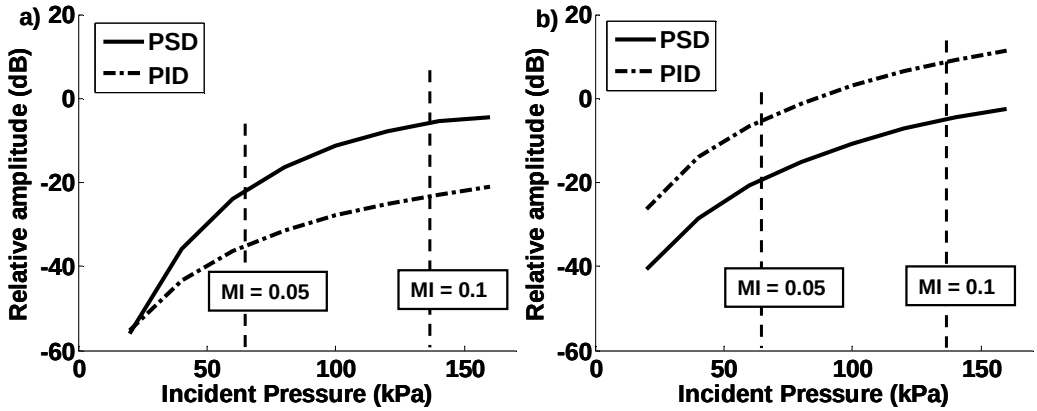

Figure 3-6: Simulated amplitudes of the nonlinear peaks for PSD and PID as a function of the driving pressure for a quadrature demodulation at a) f_0 and b) $2f_0$. The dotted lines represent the two pressures at which PSD was compared to PID in the experiments.

3.4.2 Experiments

Experimental pulse subtraction Doppler spectra calculated from a sample volume at the tube wall and from inside the tube containing static microbubbles, are represented in Figure 3-7 a) and b), respectively. In Figure 3-8, Doppler spectra for flowing cellulose particles and SonoVue™ microbubbles are presented. Both results qualitatively agree with the simulated results presented in Figure 3-5. The difference in relative amplitude observed for both simulated and experimental data could be explained by the fact that only a single microbubble response was simulated and the experimental measurements were conducted on a volume containing a multitude of scatterers.

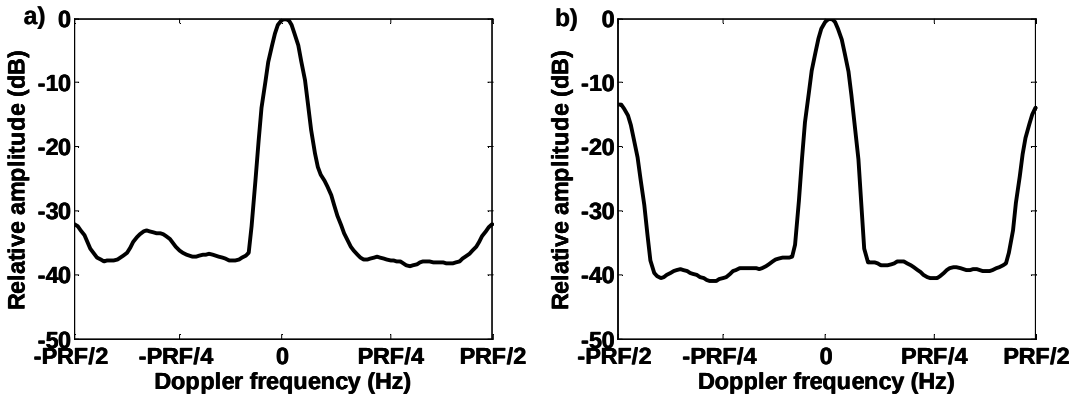

Figure 3-7: Pulse subtraction Doppler spectra for: experimental data from a static linear tube reflector (a) and from a static sample of suspension of SonoVue™ microbubbles located in the middle of the tube (b). Both demodulations were done the fundamental frequency f_o and the driving pressure used was of 150 kPa.

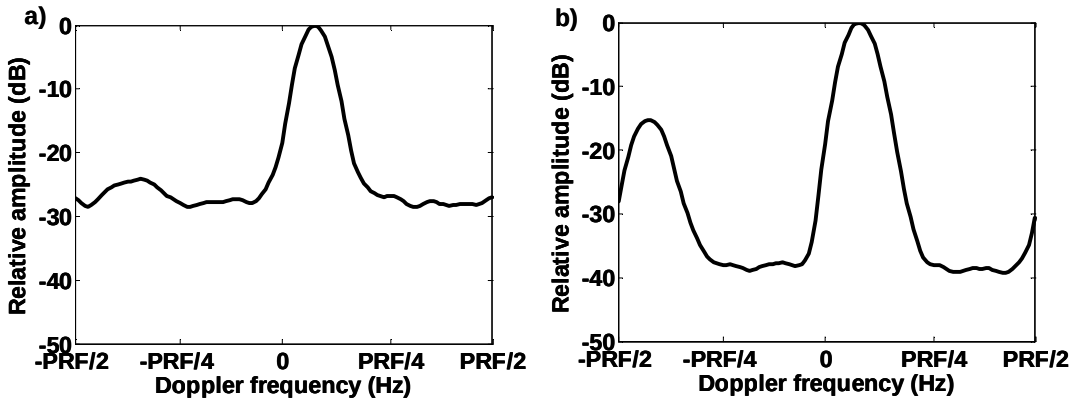

Figure 3-8: Pulse subtraction Doppler spectra for: experimental data from a flow sample located in the middle of the tube, for linear scattering cellulose particles (a) and a suspension of SonoVue™ microbubbles (b). Both demodulations were done the fundamental frequency f_o and the peak negative driving pressure used was 150 kPa.

The CTRs for PSD and PID have been represented in the bar charts Figure 3-9 for the two different demodulation frequencies. The trend in these results agrees with the simulation results in Figure 3-6. These results show that PSD at f_0 demodulation performs better than PID, with a CTR which is 1.9 (± 0.2) times higher at 0.05 MI and 3.3 (± 0.4) times higher at 0.1 MI. For a demodulation at 2 f_0 PID performs better than PSD with a CTR which is 3.5 (± 0.4) times higher at 0.05 MI and 3.1 (± 0.4) times higher at 0.1 MI. This CTR has also been shown to be higher than the CTR obtained by demodulating PSD at f_0 by a factor of 2.4 (± 0.3) at 0.05 MI and 1.9 (± 0.3) at 0.1 MI. Overall, taken in their optimum processing conditions at 0.1 MI, PID has a CTR up to 1.9 (± 0.4) higher than PSD.

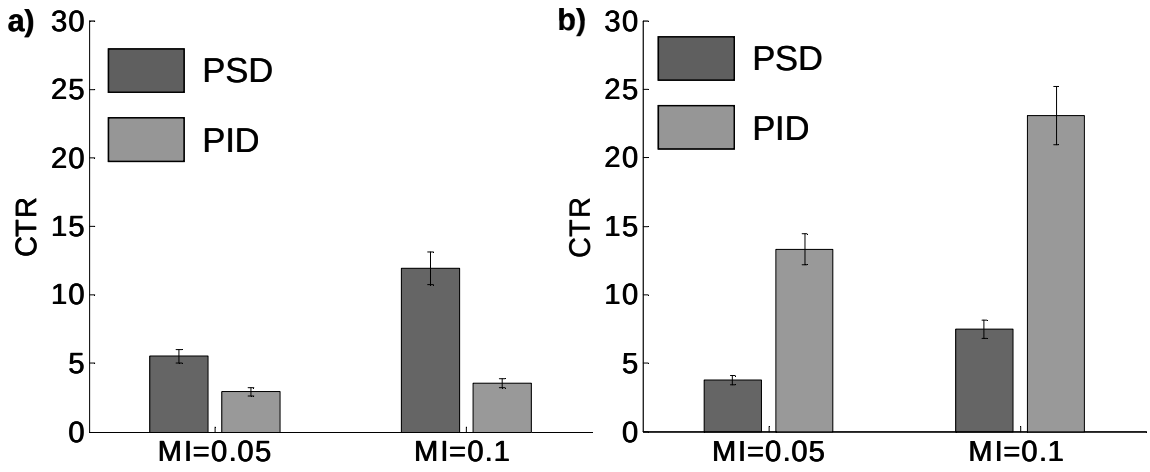

Figure 3-9: Mean (± standard error of mean) averaged over 40 samples of the CTR for PSD and PID, by demodulating at f_o (a), and at 2 f_o (b) for the two MIs.

3.5 Discussion

In this work, pulse subtraction Doppler has been presented as a technique capable of separating linear from nonlinear scatterers under static and flow conditions. This Doppler scheme is a new extension of the pulse subtraction time delay imaging method [56], adding velocity estimates to nonlinear scattering detection. The use of a virtual pulse combined with quadrature demodulation allows nonlinear Doppler processing and a production of dual-band spectra. A comparison with PID has shown PSD to be superior in distinguishing between tissue and bubble flow if the RF echoes were demodulated, as for conventional Doppler, at the fundamental frequency of the driving pulses. By demodulating at the second harmonic frequency, PID was shown to have a higher CTR than PSD.

For a standard pulsed Doppler system, the relative phase change information from consecutive echoes is used to extract the Doppler shift which reflects target motion. Doppler shifts from linear and nonlinear scatterers appear at the same frequency in the Doppler spectrum, and therefore cannot be separated. In order to differentiate these, in both PSD and PID, consecutive pulses alternate in polarity. In PSD the result is that linear scatterers appear the same for alternate pulses while in PID consecutive linear echoes are inverted in phase. This results in a Doppler spectrum in PSD where linear scatterers appear at f_d, but the alternating response from nonlinear scatterers appears shifted by PRF/2. For PID, the location of the linear and nonlinear components in the spectrum is inverted as the transmitted pulses have alternating phases.

The explanation for the differences between PSD and PID when demodulating with either f_0 or $2f_0$ is as follows. If we consider straightforward PI imaging it is recognised that only even order harmonics contribute to the detected nonlinear signals [50]. In PID this manifests itself as a difference in the alternating phase of the odd harmonics, while the even ($2f_0$) harmonics do no alternate. Therefore demodulation at $2f_0$ is required for efficient detection of non-linear scattering. Conversely, in PSD, differences between consecutive echoes due to nonlinear scattering appear in both even and odd harmonics (at f_0 and $2f_0$). This can explain the relative success of PSD when demodulating echoes at f_0.

In the framework of this *in vitro* study, the transducer pass-band was centred at 3MHz and the pulses were transmitted at 2 MHz. This approach ensured the success of PID, as it enabled an increased detection of second harmonics. The detection of nonlinear fundamental however was not optimum as the receive transducer bandwidth was not centred on the fundamental frequency of the echo. Pulse transmit efficiency and receive sensitivity of the nonlinear fundamental signal could therefore be improved by transmitting the pulses using a transducer centred at f_0. It can also be deduced that depending on the transducer characteristics and its ability to detect harmonics, PSD could prove itself as a more useful alternative in the detection of nonlinear signal. In addition, the PSD and PID pulses have been compared on the basis of equal resolution, determined by the length of the longer driving pulse in PSD. The actual energy transmitted into the medium is 25% less in PSD than in PID. PSD also has drawbacks, such as cancelling non-linear bubble response components in the initial part of the short and long pulses. Some cancellation is also occurring in the decay part of the long and short pulses. It has been shown by Chetty *et al.* [79] that shell properties of the bubbles can vary over the course of insonation. Therefore the decay parts may not always cancel in the experiments as shown by the simulations (Figure 3-1), depending on the level and duration of insonation. These cancellation characteristics reduce the amount of useful microbubble signal which contributes to the nonlinear signal. The combination of other nonlinear techniques with PSD could solve this problem.

PSD is also straightforward to implement, and was implemented on a Sonix RP 500 research scanner (Ultrasonix Medical Corporation, BC, Canada) as it will also be shown in chapter 5. PSD provides an alternative approach on scanners which suffer from the inability to produce perfectly inverted pulses, as it does not require phase inversion or amplitude modulation [54]. The experiments in this study have been conducted using a single element pulse-echo system as the Sonix RP showed poor

linearity in the production of pulse inversion sequences and, furthermore, the single element system allowed a more precise control over the transmitted pulse shapes.

Simpsons et al [50] have shown for PID that clutter arising from vessel walls or tissue can be rejected as their Doppler shifts are located in the [-PRF/2 PRF/2] region of the spectrum. PSD enables the same discrimination in the presence of stationary bubbles and tissue as nonlinear and linear scattering appear in different frequency bands of the spectrum. Likewise, in the presence of slow-tissue movements the double band characteristics will still apply. A simple way of performing clutter rejection is to ignore the frequency band containing the linear tissue signal. This filtering is simplified in PID as the technique involves demodulation at $2f_0$, which removes the linear components in the spectrum. Furthermore, Doppler techniques are limited in the detection of slow-moving targets (due to the PRF, number of pulses, window length, and pulse length). This limitation also applies to the non-linear Doppler approaches presented here. Furthermore, the length of the transmitted pulses in Doppler ultrasound affects the axial resolution of the measurement. For velocity detection a section of the demodulated signals (virtual echo and long echo) are extracted. The pulse length fundamentally determines the axial resolution for the velocity estimation. If inside the sample volume the velocity gradient is high, this will lead to spectral broadening. This is a common issue in classical pulse Doppler, which is independent of nonlinear scattering.

However, the nonlinear Doppler techniques have limitations in the distinction of slowly moving microbubbles from non-moving ones as both signals appear in the same frequency band. Tackling this issue could be of interest for the detection of targeted contrast agents. Indeed, one of the major challenges in molecular imaging with contrast agents is the detection of attached microbubbles against the background signals made of freely circulating agents and tissue [80]. One major limitation with nonlinear Doppler would be the difficulty of distinguishing slow flowing microbubbles near the vessel wall for example, from non moving targeted microbubbles. Future *in vitro* and *in vivo* work will look into using nonlinear Doppler for providing some solutions. This will include single bubble experiments providing a way of comparison with the simulation results.

3.6 Conclusions

Pulse subtraction Doppler is a new Doppler technique which was shown to allow nonlinear imaging of contrast agents as well as estimating flow velocity. In order to assess its efficacy, simulations and experiments were performed and PSD was compared with the current available technique, pulse inversion Doppler. The results

show that PSD has the same properties as PID: PSD is able to differentiate bubble motion from tissue motion. For Doppler processing conducted at the fundamental frequency, the contrast to tissue ratio in PSD was on average 3.3 (± 0.4) times higher than PID at an MI of 0.1. At the harmonic frequency, PID has shown to have a 3.1 (± 0.4) times higher CTR than PSD. Overall, taken in the best test conditions performed in this study, PID has a CTR up to 1.9 (± 0.4) times higher than PSD. The CTRs for both techniques have also been shown to increase with increasing MI. While PID is more naturally discarding linear echoes when demodulating at $2f_0$, for the same axial Doppler resolution, PSD requires less energy transmission into the medium. This makes it less likely to disrupt certain types of microbubbles or alter their acoustical properties. PSD also offers an alternative technique on scanners which cannot perform phase inversion or with transducers with insufficient bandwidth to receive harmonics. Future work will try to exploit the properties of these techniques in order to isolate signals arising from targeted microbubbles in the context of molecular imaging.

Chapter 4 Generalised contrast imaging and nonlinear Doppler

4.1 Introduction

As described in section 1.2, the use of microbubble contrast agents has highly improved the diagnostic ability of ultrasound imaging and has many applications [16]. The main contrast modes used in clinical scanners are multipulse sequences which are based on a linear relation between the pulses. Pulse inversion (PI) [50], amplitude modulation (AM) [54] and pulse inversion amplitude modulation (PIAM) can for example be found on Philips iU22 scanners and Cadence Contrast pulse sequencing (CPS) can be found on Siemens Sequoia scanners [81]. Improving the contrast and hence the image quality can lead to a better diagnosis but also sets many challenges related to the imaging application and the equipment capabilities.

One of the challenges in contrast imaging is linked to the many effects which occur during acoustic propagation though tissues. Deep tissue imaging for example is usually limited by attenuation occurring during ultrasound propagation, which reduces the contrast to tissue ratio (CTR) [82]. Attenuation increases with frequency and makes the imaging of higher order harmonics more difficult. Increasing the mechanical index (MI) would compensate for this effect, but would in turn increase microbubble destruction for superficial areas. The use of a higher MI also increases nonlinear propagation [83], [84] which would also contribute in reducing the CTR. Since tissues can produce harmonics, these will mix with the ones produced by the microbubbles and cannot be separated [85]. Finally, the MI was designed to inform the sonographer about possible mechanical damage in tissue arising from the presence of gas bodies [12]. Regulations [86] limit the maximum MI to be used during an imaging session to ensure a safe scan.

A second type of contrast imaging challenge is defined by the linearity of the equipment. If the hardware transmission chain is not perfectly linear, some spectral components appear in the transmitted signals and will be preserved in the tissue backscattered echoes [87]. These additional signals will lead to a non-perfect cancellation of linear tissue signals and the CTR will therefore be affected. The ability of the equipment to precisely control the transmitted amplitude, phase, frequency and pulse length of the desired contrast sequence can therefore be a limiting factor in the

choice of a pulse sequence. For example, an imprecise control of the phase will reduce the ability of pulse inversion to cancel linear tissue signals in order to isolate microbubble signals [88].

Another relevant hardware limit to contrast imaging is the bandwidth of the ultrasound probe, which is the frequency range over which the probe is capable of transmitting and receiving ultrasound. Narrow bandwidth probes can hinder the detection of harmonics [89], and certain types of pulse sequences based on the measurement of higher order harmonics may therefore not perform at their full potential.

The sensitivity of the system to noise can also affect the CTR. Weak echoes from scatterers, such as those seen when performing deep tissue imaging, may not be distinguishable from the noise level. As described by Crocco *et al.* [87], the system noise can strongly affect the performances of multipulse techniques, and the pulse sequence must be chosen accordingly.

Finally, tissue motion generally occurring due to breathing and heart beats is another limiting factor in contrast imaging. Since linear scattering cannot be suppressed properly when motion is present, this non-cancellation will be detected as a nonlinear signal. Transmitting sequences of more than two pulses [90], [55] can improve the rejection of clutter and improve the signal to noise ratio. In colour Doppler imaging, tissue motion creates an additional Doppler frequency of large amplitude in the spectrum. This clutter signal can be removed by high pass filtering the Doppler signal [91], [92]; however such filtering can also remove the slow moving blood. Combining power Doppler with an initial second harmonic filtering of the echoes was shown to enable a better reduction of Doppler clutter signals arising from tissue motion [93]. Although they can be partially removed using appropriate wall filters, the presence of nonlinear tissue harmonics still affects the performance of harmonic Doppler.

Pulse inversion Doppler (PID) was shown to overcome the problem of tissue motion. When applicable, PID also has the advantage of working over the entire bandwidth of the transducer [50], which overcomes the trade-off between contrast and resolution. As described in 2.1.2.2, phase inverted pulses are transmitted into the tissue [50], and it has been shown that for successive echoes, the odd harmonic components of the echo change sign with the transmitted pulses, whereas the even harmonic components do not. The harmonic decomposition of the echoes was explained to give rise to two different Doppler frequencies $f_{d,odd}$ and $f_{d,even}$ for the even and odd harmonic components respectively. This is shown in Equation 4.1 and Equation 4.2:

$$f_{d,odd} = \frac{2v}{c} f_0 + \frac{PRF}{2} = f_d + \frac{PRF}{2}$$ Equation 4.1

$$f_{d,even} = \frac{2v}{c} f_0 = f_d$$ Equation 4.2

where f_d is the Doppler frequency for normal pulsed Doppler, as shown in Equation 4.3.

$$f_d = \frac{\Delta\varphi}{2\pi} PRF = \frac{2v}{c} f_0$$ Equation 4.3

where $\Delta\varphi$ is the phase shift between successive echoes, f_0 is the transmitted frequency, v the velocity of the scatterer, c the speed of sound and PRF the pulse repetition frequency.

In PID, the Doppler spectrum was therefore shown by Simpson *et al.* [50] to be separated into two regions: one containing Doppler signals arising from nonlinear scattering, corresponding to $f_{d,even}$ frequencies and one arising from both linear and nonlinear scattering, corresponding to $f_{d,odd}$ frequencies.

However, it was shown in section 3.4 that transmitting alternatively short and longer pulses and performing pulse subtraction Doppler (PSD), also enabled a separation in the Doppler spectrum of nonlinear and linear scattering. In PSD, however, the transmitted pulses had the same initial phase. Linear scattering was found to have a Doppler frequency of f_d, and nonlinear scattering a Doppler frequency at $f_d + PRF/2$, which is an inverted repartition of the spectrum compared to PID. The theory provided by Simpson *et al.* [50] for the explanation of the PID spectrum is restrained to pulse inversion and is not applicable to explain the repartition of the scattering in the PSD spectrum.

As explained above, contrast imaging sets many challenges with regards to imaging application and equipment capabilities. The current imaging modalities are not yet sufficient to satisfy all medical imaging requirements. The motivation of this chapter is to develop tools for the selective choice of a contrast mode, with the ultimate goal of improving targeted contrast agents imaging, and for taking into account the imaging constraints. This is done by the introduction of a more generalised form of nonlinear Doppler and a general explanation of the dual band spectrum these techniques provide.

4.2 Nonlinear Doppler theory

Standard multipulse contrast techniques are based on a linear relation between the pulses, such as amplitude, phase and pulse length. This work extends these ideas to form generalised pulse pairs.

4.2.1 Driving pulses

In the generalised nonlinear Doppler technique, two pulses p_1 and p_2 are sent at a pulse repetition frequency (PRF) consecutively into the tissue and then repeated to form a Doppler sequence. The two pulses are shown in Equation 4.4 with the second pulse p_2 being constructed by any linear combination of pulse p_1.

$$\begin{cases} p_1(t) \\ p_2(t) = \sum_{n=1}^{N} a_n p_1(t - \Delta t_n) \end{cases} \qquad \text{Equation 4.4}$$

For a given pulse p_1, a second pulse p_2 is the concatenation of N copies of p_1, with the n^{th} copy shifted in time by Δt_n and amplitude scaled by a_n. Of course the pulse pair p_1 and p_2 could be different linear combination of a third pulse p_3, but this would lead to similar considerations under a more complex parameterisation, and is not treated here.

It is easily seen that current pulse pair sequences known to enhance the CTR such as PI, AM, PIAM and PS are particular cases of Equation 4.4. Table 4-1 summarises the existing detection methods and their corresponding coefficients for the general nonlinear Doppler technique, as defined by Equation 4.4.

Table 4-1: Current contrast agent detection techniques and their pulse design parameters.

	PI	AM	PIAM	PS
N	1	1	1	>1
a_n	-1	0.5	-0.5	1
Δt_n	0	0	0	*T = constant (length of p_1)*

4.2.2 Echo processing

Once the echoes $E\{p_1\}$ and $E\{p_2\}$ from p_1 and p_2 respectively are received, a “virtual” echo E_V can be constructed using $E\{p_1\}$ to compensate for the pulse length, amplitude and phase differences between p_1 and p_2, as shown in Equation 4.5.

$$\begin{cases} E\{p_1\} \\ E\{p_2\} = E\left\{\sum_{n=1}^{N} a_n p_1(t-\Delta t_n)\right\} \\ E_V = \sum_{n=1}^{N} a_n E\{p_1(t-\Delta t_n)\} \end{cases}$$ Equation 4.5

Linear static scattering can be suppressed by subtracting $E\{p_2\}$ from E_V.
In such case

$$E\left\{\sum_{n=1}^{N} a_n p_1(t-\Delta t_n)\right\} = \sum_{n=1}^{N} a_n E\{p_1(t-\Delta t_n)\}$$ Equation 4.6

However for nonlinear scattering the residue signal R will be non zero after subtraction (Equation 4.7).

$$R = E\{p_2\} - E_V$$ Equation 4.7

This characteristic can be used when combining the general pulse sequence with Doppler.

4.2.3 Effect of noise

As described by Crocco *et al.* [87] the introduction of noise by the system during transmission and reception can affect the performances of multipulse techniques. Indeed, the noise can be considered as white Gaussian noise and uncorrelated from echo to echo. The noise level will also be affected by the compensation process during which the virtual echoes are created. Different pulse combinations will induce different noise levels in the residue. The standard deviation of the noise present in the virtual echo σ_v can be expressed as a function of the standard deviation σ of the noise in one echo, using the general properties of normal distributions. If σ is considered as constant between successive echoes, σ_v will be weighted by the p_2 pulse construction coefficients and can be expressed as in Equation 4.8.

$$\sigma_V = \sqrt{\sum_{n=1}^{N} {a_n}^2 \sigma^2}$$ Equation 4.8

After subtraction of $E\{p_2\}$ from E_V, the noise level of the residue R will take the form:

$$\sigma_R = \sqrt{\sum_{n=1}^{N} (a_n{}^2 + 1)\sigma^2}$$ Equation 4.9

4.2.4 Nonlinear Doppler processing

While the Doppler frequency repartition in PID can be explained by the phase inverted transmitted pulses [50], the dual frequency band repartition for the PSD sequence cannot be explained in the same way. A generalised approach is needed and will be developed in the following section. The cases of a linear scatterer and a nonlinear scatterer will first be analysed.

4.2.4.1 Linear case

When processing the signals issued form a linear scatterer, after the construction of the virtual echo, the Doppler echoes E_V and $E\{p_2\}$ are equivalent to echoes originating from a linear scatterer in normal pulsed Doppler, and the complex Doppler signal *E(k)* takes the form as described by Equation 2.21:

$$E(k) = g''(t_x - t_0 - k\frac{2v_x T}{c}).e^{-i2\pi f_d kT}$$ Equation 4.10

The sampled Doppler *E(k)* signal is made of the product of *g"*, a slow-time varying envelope, with a complex sinusoid of frequency f_d, the Doppler frequency, which is proportional to v_x, the velocity of the scatterer at the depth of computation. *T* represents here the time interval between pulses (*1/PRF*), *c* the speed of sound in tissues and t_0 the time corresponding to the initial position of the scatterer. The in-phase channel of the complex envelope is represented in Figure 4-1 a). Therefore, at a certain depth of interest corresponding to a time t_x, taking the Fourier transform of E(k) leads to a Doppler spectrum, containing one Doppler frequency peak located at f_d, proportional to the scatterer velocity, as shown in Figure 4-1 b).

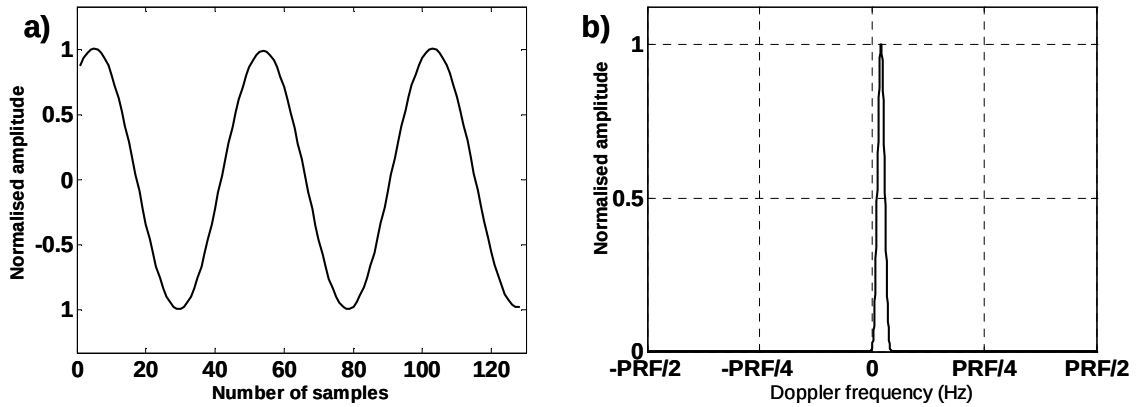

Figure 4-1: a) Simulated in-phase channel obtained when using a nonlinear Doppler sequence on a linear scatterer moving at a constant velocity. The Doppler signal was calculated based on 128 echoes. Motion was simulated by including a 10 ns time shift between each echo lines. For a PRF set to 10 kHz, the corresponding simulated velocity was of 7.7 cm.s^{-1}. b) Corresponding Doppler spectrum with one Doppler peak.

However, in the case of a nonlinear scatterer, another type of Doppler signal will be observed.

4.2.4.2 Nonlinear case

In the case of Doppler imaging a nonlinear scatterer, the envelope g'' will not remain constant from echo to echo. It will vary every two pulses between g_1'' and g_2'', corresponding to the envelopes of the echoes E_v and $E\{p_2(t)\}$ respectively. At time t_x the complex Doppler signal can be written as follows:

$$\begin{cases} E(k) = g_1''(t_x - t_0 - k\dfrac{2v_xT}{c})e^{-i2\pi f_d kT} & \text{for } k \text{ even} \\ E(k) = g_2''(t_x - t_0 - k\dfrac{2v_xT}{c})e^{-i2\pi f_d kT} & \text{for } k \text{ odd} \end{cases} \qquad \text{Equation 4.11}$$

This complex Doppler signal can be seen as the product of the oscillation of two slow-time varying envelopes g_1'' and g_2'' at a rate of *PRF/2*, with a complex sinusoid of frequency f_d, as shown by the in-phase channel in Figure 4-2 a). This product expresses itself in the Doppler spectrum by two Doppler frequency peaks: one located at f_d, containing linear scattering as well as a portion of harmonic components, and one peak located at f_d + *PRF/2*, containing only harmonic components, as shown in Figure 4-2 b).

The velocities can only be correctly estimated if their corresponding Doppler frequencies follow the revised Nyquist limit [50], as shown in Equation 4.12.

$$f_{d,\max} \leq \frac{PRF}{4}$$ Equation 4.12

where $f_{d,max}$ corresponds to the maximum measurable Doppler frequency.

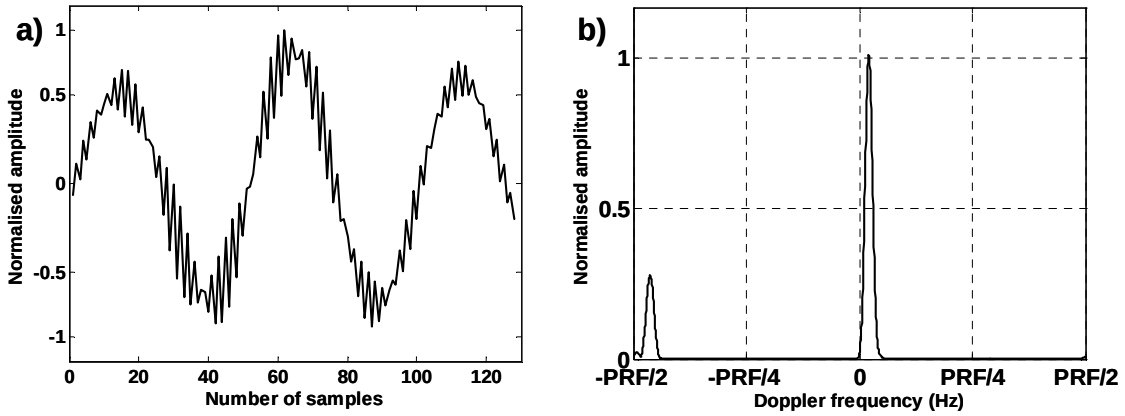

Figure 4-2: a) Simulated in-phase channel obtained when using a nonlinear Doppler sequence on a simulated single microbubble moving at a constant velocity. The Doppler signal was calculated based on 128 echoes. Motion was simulated by including a 10 ns time shift between each echo lines. For a PRF set to 10 kHz, the corresponding simulated velocity was of 7.7 cm.s^{-1}. b) Corresponding Doppler spectrum with two Doppler peaks.

4.2.4.3 Relation between the residue and the amount of nonlinear energy in the Doppler spectrum

As described by Simpsons *et al.* [50], pulse inversion is a specific case of PID, where only two pulses are transmitted along one line of sight. The sum of the echoes is represented in one band of the spectrum and its difference in the other band. Similarly, in the proposed nonlinear Doppler approach, the envelope oscillation in the Doppler signal is directly related to the residue *R* of the echoes. In the case of two transmitted pulses only, the residue of the echoes will be represented in the nonlinear part of the spectrum. Studying the energy contained in the residue signal is therefore equivalent to studying the energy content of the nonlinear part of the spectrum. In the particular case of linear scatterers the residue is null, leading to one single frequency peak in the spectrum.

4.2.5 Summary

In this section a novel way to describe multipulse sequences was proposed. It was shown that the pulse sequences described by are all Doppler compatible but are also directly applicable to contrast imaging without Doppler processing. The Doppler spectrum for a linear scatterer was shown to be equivalent to a Doppler spectrum

originating from a linear scatterer in normal pulsed Doppler. For a nonlinear scatterer, it was shown that the Doppler spectrum can be separated into two regions: one region due to nonlinear scattering only, and one, due to linear as well as nonlinear scattering.

4.3 Methods

The following simulation study investigates several transmission pulse pairs and their effect on the contrast. Since the driving pulses have different initial properties such as pressure, energy and pulse length, the contrast was normalised in order to account for these differences. The sensitivity of the pulse combinations to noise is also studied.

4.4 Simulations

A simulation study was conducted in order to assess different nonlinear Doppler sequences, designed following the model described in section 4.2.1. A modified Rayleigh-Plesset (RP) equation based on de Jong's constant thickness model [44] was used to simulate the acoustic response to nonlinear pulse sequences of a microbubble, 3 µm in diameter and with shell properties similar to SonoVue^{TM} (shell friction and elasticity parameters: S_f = 0.45 10^{-6} kg.s^{-1} and S_p = 1.1 N.m^{-1}, respectively [78]), located at a distance of 5 cm.

The pulses and the simulated echoes were band-pass-filtered using a custom filter (0.5 – 7 MHz bandwidth, 5 pole Butterworth) in order to simulate the broadband transducer of central frequency 3.5 MHz, used in the experiments in chapter 3 (Figure 1-1).

4.4.1.1 Pulse sequences

A few nonlinear pulse pair sequences, based on the transmission of two pulses were tested in the simulations. Pre-existing modes such as PI [53], AM [94], PIAM [51] and PS [24], [25] were modelled for comparison purposes. Novel combinations of all these pulse sequences such as pulse inversion pulse subtraction (PIPS), amplitude modulation pulse subtraction (AMPS), and a combination of all the modes, pulse inversion amplitude modulation pulse subtraction (PIAMPS) were also tested. The latter are represented in Table 4-2 with their corresponding pulse design coefficients. These techniques were also compared with standard harmonic imaging.

Table 4-2: Novel contrast agent detection techniques and their pulse design parameters.

	PI PS	AMPS	PIAMPS
N	>1	>1	>1
a_n	-1	0.5	-0.5
Δt_n	*T = length of p_1*	*T = length of p_1*	*T = length of p_1*

More complex combinations are possible for different values of N, a_n, and Δt_n, but were not tested in this study in order to reduce the computational cost.

4.4.1.2 Pulse design parameters

The pulse sequences described in section 4.4.1.1 were formed with a given set of parameters in order to reduce the possible number of combinations. The responses to the pulse pair sequences were modelled via the Rayleigh-Plesset equation. The pulse parameters used were the following:

Centre frequency: All the driving pulses had a centre frequency of 2MHz, corresponding to the microbubble resonant frequency.
Driving pressure: Two peak negative pressures were used (75kPa and 150kPa), corresponding to MIs at 2MHz of 0.05 and 0.1 respectively. These values of MI were chosen to be low so that it is unlikely the microbubbles are destroyed.
Pulse length: Two different pulse lengths were used: a short length L_1 of 3 cycles and a longer length L_2 of 6 cycles corresponding to typical B mode and Doppler imaging pulse lengths [95].

4.4.1.3 Contrast

The contrast was then calculated for each of the tested pulse sequences. In this study a measure of the amount of contrast generated by a single microbubble was defined by the area underneath the envelope of the residue R (Equation 4.7). The amplitude of the envelope is the parameter which determines the brightness in a contrast enhanced image and the width its response duration. The area underneath the envelope, which would be proportional to the product of both amplitude and width, was therefore computed. Similarly, the envelope of the harmonic signal was considered for computing the contrast in harmonic imaging mode.

4.4.2 Types of criteria

The efficiency of each pulse sequence will depend on the favoured clinical application and ultrasound system characteristics. In order to compare the pulse sequences, the amount of contrast produced by each pulse pair was therefore normalised accordingly. The following section describes some comparison criteria relevant to standard clinical applications as well as to the imaging system properties.

4.4.2.1 Pulse design criteria

A limited number of criteria, among the more classic, were chosen for the comparison of the nonlinear pulse sequences. Depending on the application and imaging constraints, several parameters can be taken into account during the design of the transmitted pulses. A few of them were considered in this study:

Resolution (Lmin): This parameter is related to the pulse length of the transmitted pulses, and thus to the imaging resolution, hence the name of the parameter. In this study it was defined by the number of cycles of the shortest pulse of the pulse pair, since its echo could be used for the production of a high resolution B-mode image.

Peak negative pressure (P-Max): The maximum peak negative pressure of the pulse sequence is commonly considered as the parameter most likely to affect the stability of the bubble. Since the centre frequency was kept constant, the MI was directly proportional to this parameter, as shown in Equation 1.1.

Resolution and peak negative pressure (AreaTrans): This criterion was set in order to account for both the resolution and the MI. This criterion was represented by taking the area under the driving pulses, proportional to the product of the pulse length with the peak negative pressure.

Total transmitted energy (ETrans): For patient safety reasons, the total energy transmitted into the tissues should be kept to a minimum. The energy of the driving pulses is a parameter linked to the thermal index (TI) as described in [96], which depends on the pulse length and peak intensity. The total energy transmitted was therefore considered and was defined as the sum of the energies contained in both p_1 and p_2 pulses.

A summary of the different pulses tested and their corresponding criteria is given in Table 4-3.

Table 4-3: Summary of the nonlinear pulse sequences tested. The amplitudes (a_1, a_2) and pulse lengths (L_1, L_2) indicated in number of cycles are given for the two transmitted pulses p_1 and p_2 respectively. The corresponding transmitted energy (Etrans), peak negative pressure (p^-) and resolution are also provided.

		Pulse design parameters				Pulse design criteria			
Number	Technique	a_1 (kPa)	L_1	a_2 (kPa)	L_2	E Trans	P- Max (kPa)	Lmin	Area Trans
1	PI	150	3	-150	3	147	150	3	187
2		150	6	-150	6	294	150	6	374
3		75	3	-75	3	36.75	75	3	93.5
4		75	6	-75	6	73.5	75	6	187
5	AM	-150	6	-75	6	183.75	150	6	281
6		150	6	75	6	183.75	150	6	281
7		-150	3	-75	3	91.875	150	3	140
8		150	3	75	3	91.875	150	3	140
9	PS	150	3	150	6	220.5	150	3	281
10		-150	3	-150	6	220.5	150	3	281
11		75	3	75	6	55.125	75	3	140
12		-75	3	-75	6	55.125	75	3	140
13	PIAM	150	6	-75	6	183.75	150	6	281
14		-150	6	75	6	183.75	150	6	281
15		150	3	-75	3	91.875	150	3	140
16		-150	3	75	3	91.875	150	3	140
17	PIPS	-150	3	150	6	220.5	150	3	281
18		150	3	-150	6	220.5	150	3	281
19		75	3	-75	6	55.125	75	3	140
20		-75	3	75	6	55.125	75	3	140
21	AMPS	75	3	150	6	165.375	150	3	234
22		-75	3	-150	6	165.375	150	3	234
23		150	3	75	6	110.25	150	3	187
24		-150	3	-75	6	110.25	150	3	187
25	PIAMPS	75	3	-150	6	165.375	150	3	234
26		-75	3	150	6	165.375	150	3	234
27		150	3	-75	6	110.25	150	3	187
28		-150	3	75	6	110.25	150	3	187
29	Harmonics	150	6			147	150	6	187
30		75	6			36.75	75	6	93
31		150	3			73.5	150	3	93
32		75	3			18.375	75	3	47

4.4.2.2 Contrast criteria

Due to the limited bandwidth of transducers, the total contrast was also separated in its different harmonic components by band-pass filtering the residue. For the nonlinear fundamental (2 MHz), second harmonic (4 MHz) and third harmonic (6 MHz) contrasts, the residue for each pulse sequence was band-pass filtered between [0.5MHz-3MHz], [3MHz-5MHz] and [5MHz-7MHz] respectively. The contrasts for each component were then calculated separately.

Noise was also added to each of the simulated echoes in order to study its effect on the contrast to noise ratio (CNR). The noise was chosen to be white Gaussian noise of mean zero and standard deviation 2.5. This value corresponds to the relative noise level observed on real data acquired with the pulse echo system, described in section 3.3.2. For each pulse sequence each simulation was repeated 20 times. The mean CNRs were then estimated by averaging the contrast obtained after noise addition and dividing it by the corresponding noise level.

For all the different pulse sequences tested, the contrast and the CNR were normalised according to different pulse design criteria: transmitted energy peak negative pressure, minimum pulse length and a combination of the total pulse length and driving pressure.

4.5 Results

In the following graphs, the contrast was normalised by the different initial criteria and is represented as a function of the pulse combination number, described in Table 4-3. The different imaging modes are represented in different colour bands. For each mode, four different pulse sequences were possible, due to the different transmission parameters, described in Table 4-3. Pulse sequences will be compared by calculating their relative contrast level differences in dB. In certain cases the spectral components of the residue signals will be extracted and represented.

For all the pulse combinations tested in this study, the calculated total contrast is represented in Figure 4-3 a), as well as its decomposition into its individual harmonic components. The contrast in the nonlinear fundamental is shown in b), the second harmonic in c) and the third harmonic in d).

As shown by Figure 4-3 a), the highest total contrast was obtained for PI imaging, which transmits two six cycle long pulses at 0.1 MI (n° 2). It was shown to be 1.3 dB higher than the highest PIPS (n° 18), 1.9 dB higher than PIAM (n° 15) and 2.7 dB higher than PIAMPS (n° 25).

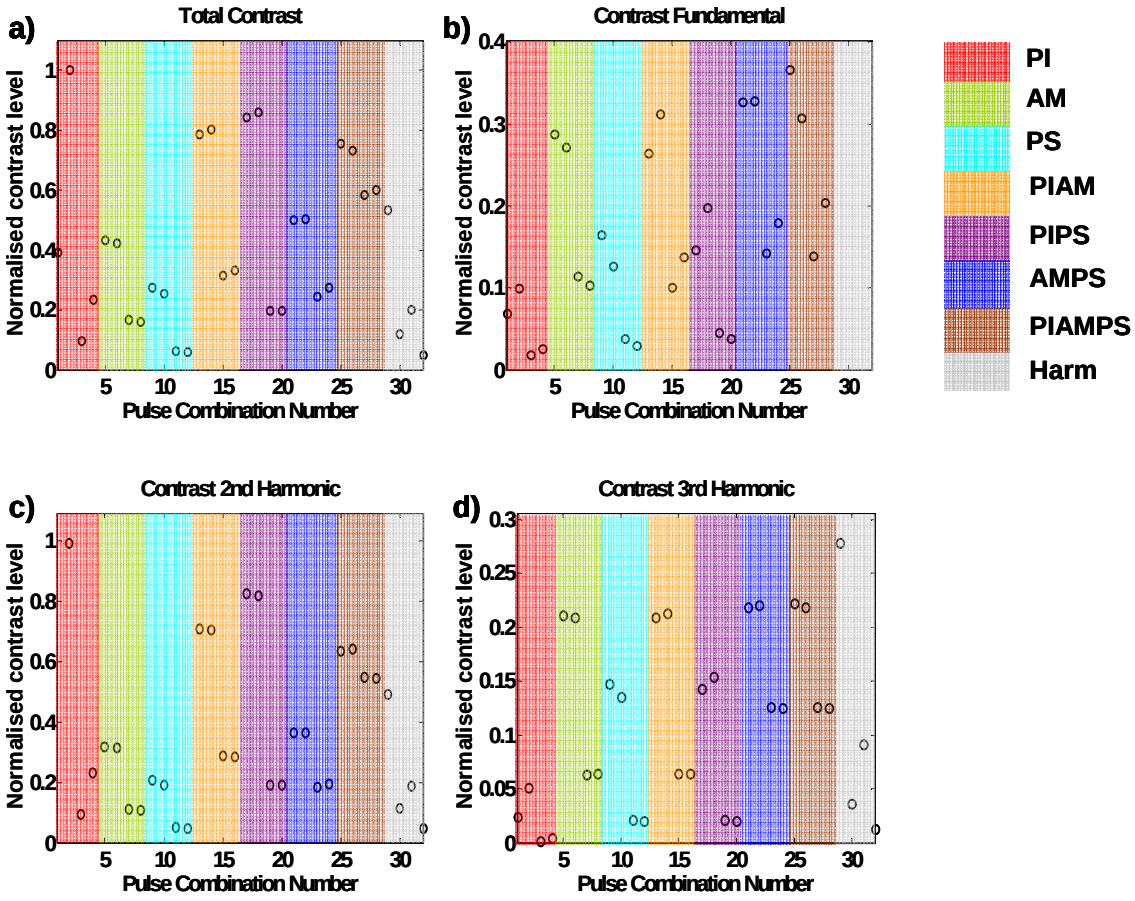

Figure 4-3: a) Total contrast and its decomposition into the three nonlinear harmonics: b) nonlinear fundamental, c) second harmonic and d) third harmonic, as a function of the pulse combination sequence. All the contrast levels were normalised by the highest total contrast obtained. The pulse combination number refers to the pulse sequence number described in Table 4-3.

However when it comes to nonlinear fundamental contrast, the residue signal is very small for PID and non-existent in harmonic imaging, since it is suppressed with the tissue signal. As shown in Figure 4-3 b), PIAMPS (n° 25) obtains the highest nonlinear fundamental. It is 0.9 dB higher than AMPS (n° 22), 1.4 dB higher than PIAM (n° 14) and 2.1 dB higher than AM (n° 5).

At the second harmonic, the highest level of contrast was obtained for PI imaging (n° 2) as shown in Figure 4-3 c). It is 1.6dB higher than PIPS (n° 17), 2.9 dB higher than PIAM (n° 13), 3.8 dB higher than PIAMPS (n° 25) and 6.1dB higher than for second harmonic imaging (n° 28). For the sequences tested, the highest levels of contrast

were mostly achieved by pulse sequences made of phase inversion, which is shown by the similar trends between Figure 4-3 a) and c).

Detecting higher harmonics has been shown to improve the contrast to tissue ratio [89], and the image resolution [97]. The maximum contrast at the 3rd harmonic component was obtained for harmonic imaging, as shown in Figure 4-3 d). A few other techniques such as AM, PIAM, AMPS, PIAMPS achieve a 3rd harmonic detection 2.2 dB (±0.2dB) lower.

The difference in the harmonic repartition between pulse sequences displayed in Figure 4-3 is illustrated in Figure 4-4 and Figure 4-5 specifically for PI with PIAMPS. The driving pulses for PI and PIAMPS are shown in Figure 4-4 a) and Figure 4-5 a) respectively. The simulated echo responses of a bubble and the calculated residue are shown in b). Finally, the frequency spectra of the residues *R* are shown in d) and represent the different harmonic components for the two pulse sequences. For PI, the residue response is located at the second harmonic and its amplitude is twice that of the single echo, as shown in Figure 4-4 d).

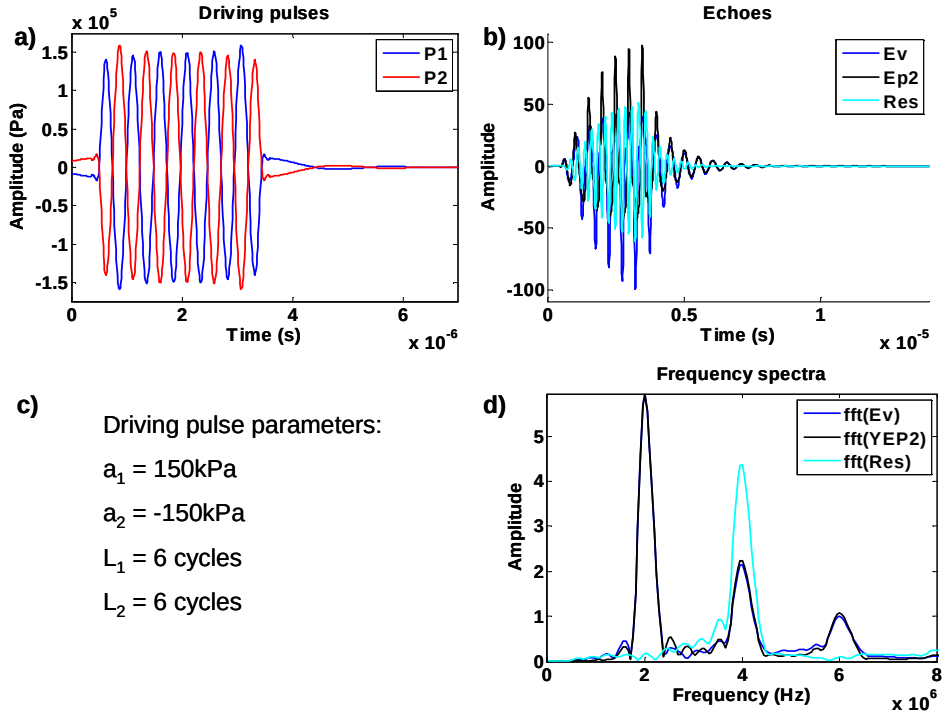

Figure 4-4: PI pulse pair sequence, a) driving pulses, b) echoes and residue, c) pulse parameters, d) frequency spectra of the echoes and the residue.

However the residue for PIAMPS is distributed among the three harmonic components (fundamental, second harmonic and third harmonic), as shown in Figure 4-5 d).

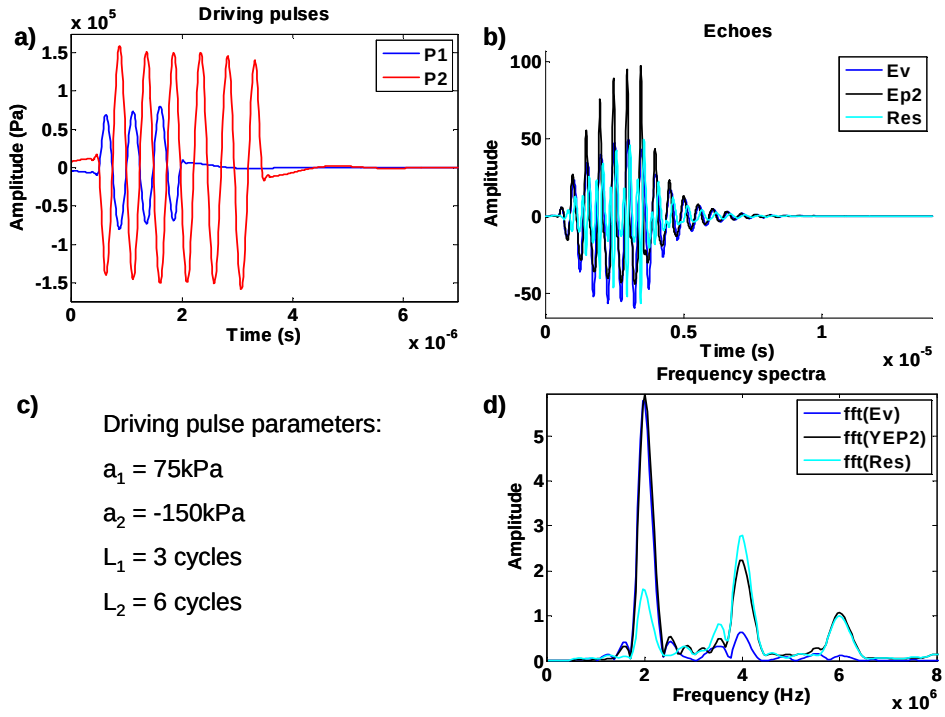

Figure 4-5: PIAMPS pulse pair sequence, a) driving pulses, b) echoes and residue, c) pulse parameters, d) frequency spectra of the echoes and the residue.

The total contrast shown in Figure 4-3 was then normalised by the different pulse design parameters in order to account for the transmitted energy (E Trans), peak negative pressure (P- Max), minimum pulse length (Lmin) and a combination of the peak negative pressure and pulse length (Area Trans). Figure 4-6 a) shows the total contrast after normalising it by the total transmitted energy.

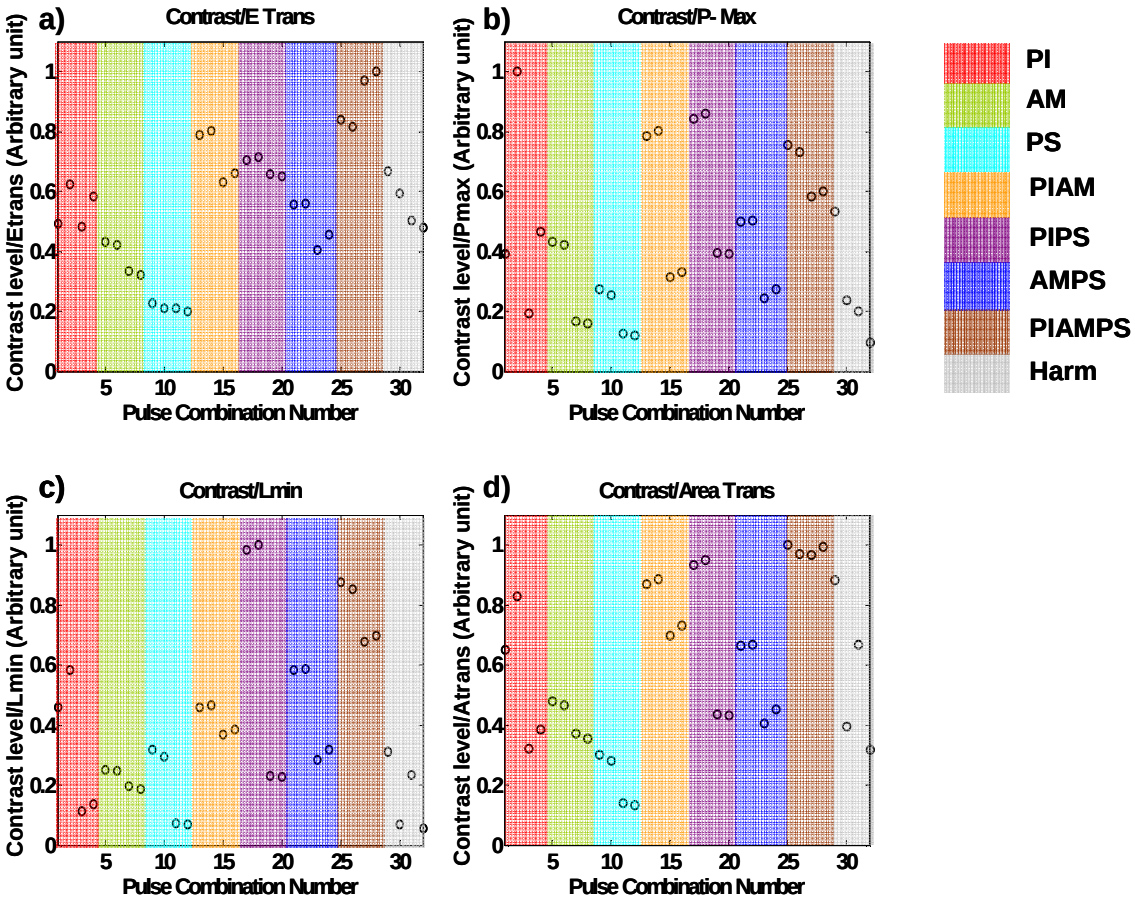

Figure 4-6: a) Total residue contrast normalised by the transmitted energy, b) the max transmitted pressure, c) the minimum pulse length used and d) the transmitted pulse area.

The highest contrast was attained by PIAMPS (n°28) , followed by PIAM (n°15) which is 1.5 dB lower. If the energy transmitted into the tissue is to be considered, these pulse combinations could be preferred over PI (n°2), since they require less energy transmission. Although other PI combinations (n°1, 3 and 4) require less energy, their contrast to energy ratio was lower.

When normalising by the maximum incident peak negative pressure, as shown in Figure 4-6 b), PI performed best. Since PI, PIPS and PIAMPS have the same maximum negative driving pressure level of 150 kPa, their relative normalised contrast is the same as for the total contrast.

When normalised by the minimum pulse length, as shown in Figure 4-6 c) PIPS (n°17) and PIAMPS (n° 25) offered the best contrast. The short transmitted pulse of the sequences offers a good resolution which can be used for B-mode imaging as well as to provide contrast for nonlinear Doppler imaging.

When combining the entrance criteria by accounting for the total pulse lengths and the total negative pressures, Figure 4-6 d) shows that PIAMPS offers the best contrast. It is 1 dB higher than for harmonic imaging, 1.5 dB higher than for PIAM, 2 dB higher than for PIPS, 2.5 dB higher than for AMPS and 4.7 dB higher than for PI.

For each of the three harmonic components (nonlinear fundamental, second harmonic and third harmonic) the contrast was normalised by the same pulse design parameters and represented in Figure 4-7.

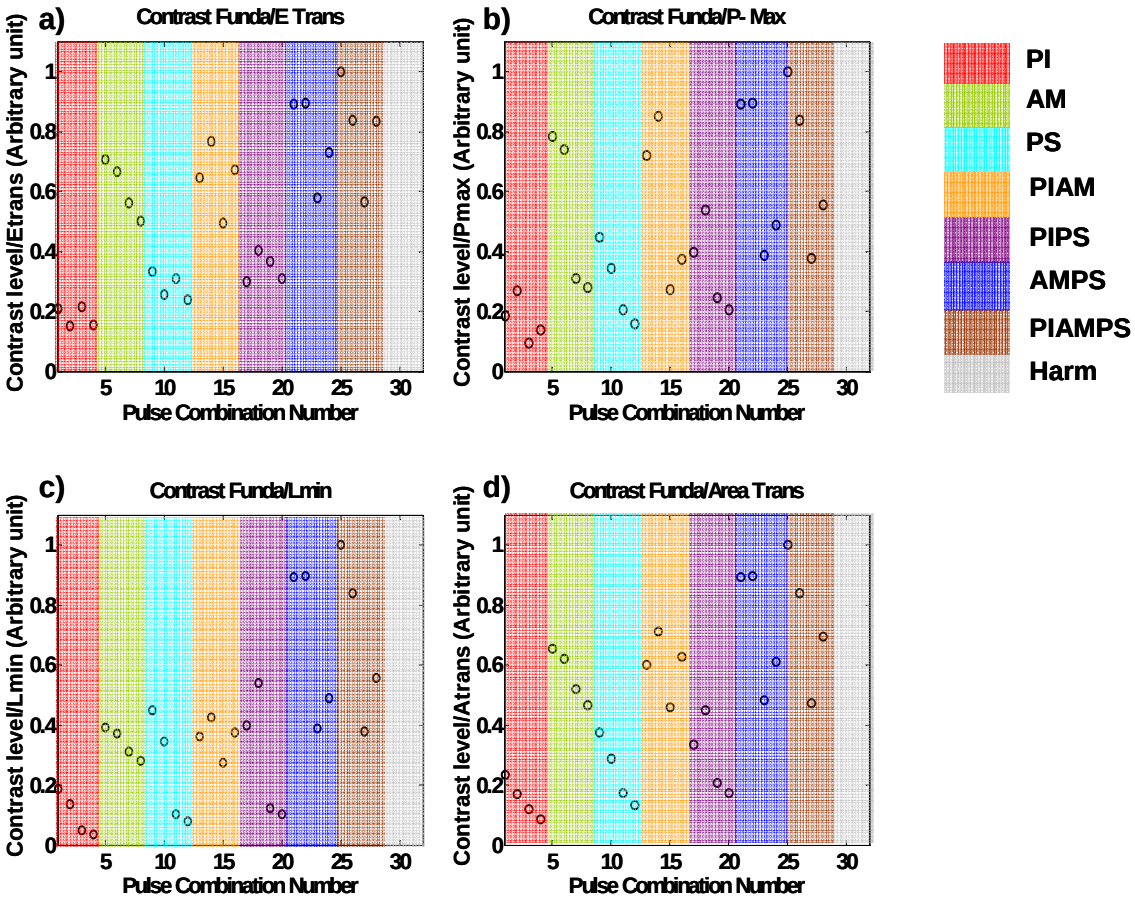

Figure 4-7: a) Nonlinear fundamental contrast normalised by the transmitted energy, b) the maximum transmitted pressure, c) the minimum pulse length used and d) the transmitted pulse area.

For the nonlinear fundamental, as shown in Figure 4-7, PIAMPS (n° 25) followed by AMPS (n° 22), PIAM (n° 14) and AM (n° 5) are the pu lse combinations which provided the best nonlinear fundamental contrast for all the normalisations.

The same normalising process was applied to the contrast originating from the second harmonics and is presented in Figure 4-8.

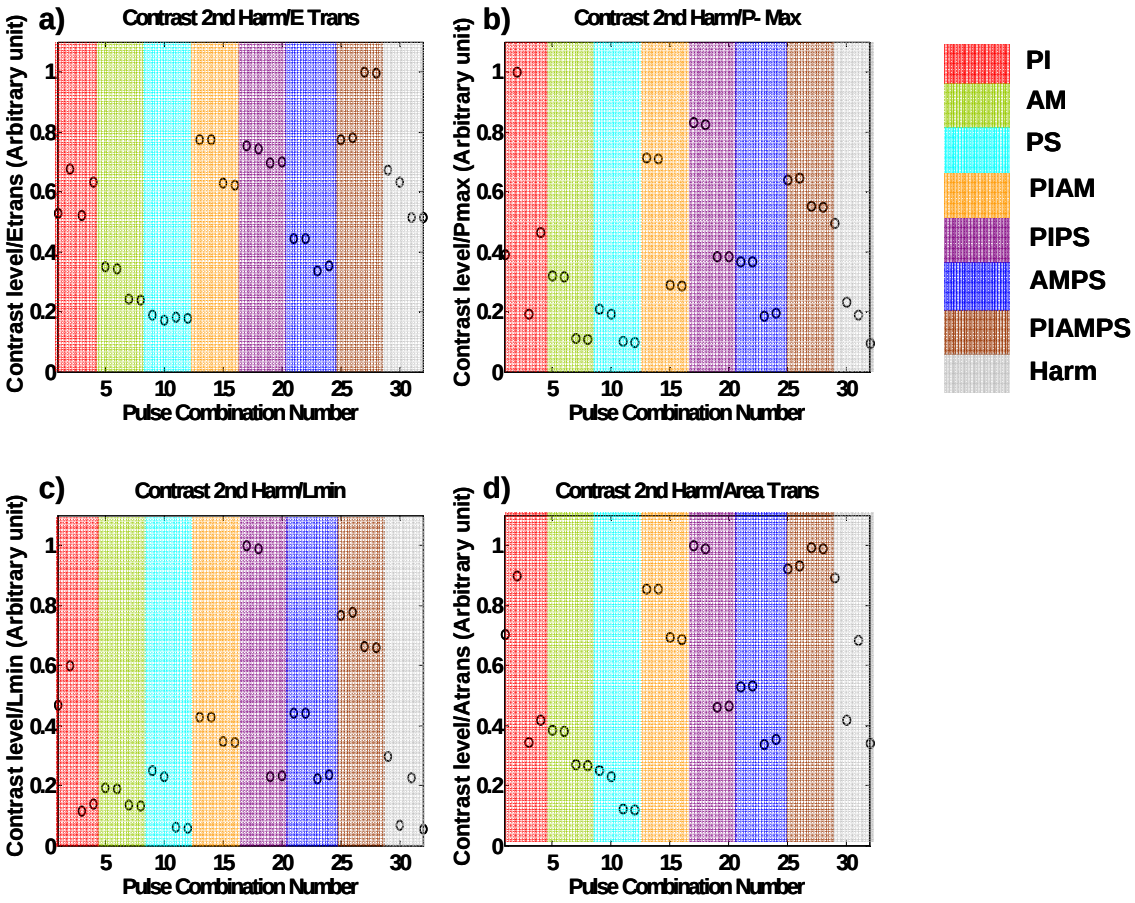

Figure 4-8: a) Second harmonic contrast normalised by the transmitted energy, b) the maximum transmitted pressure, c) the minimum pulse length used and d) the transmitted pulse area.

When normalising by the transmitted energy, the best contrast was obtained for PIAMPS (n°27). PIAMPS was followed by PIAM (n°14) and PIPS (n°17) and by PI (n° 2). The pulse combinations based on phase inversion performed better than the others such as AM, PS, and AMPS.

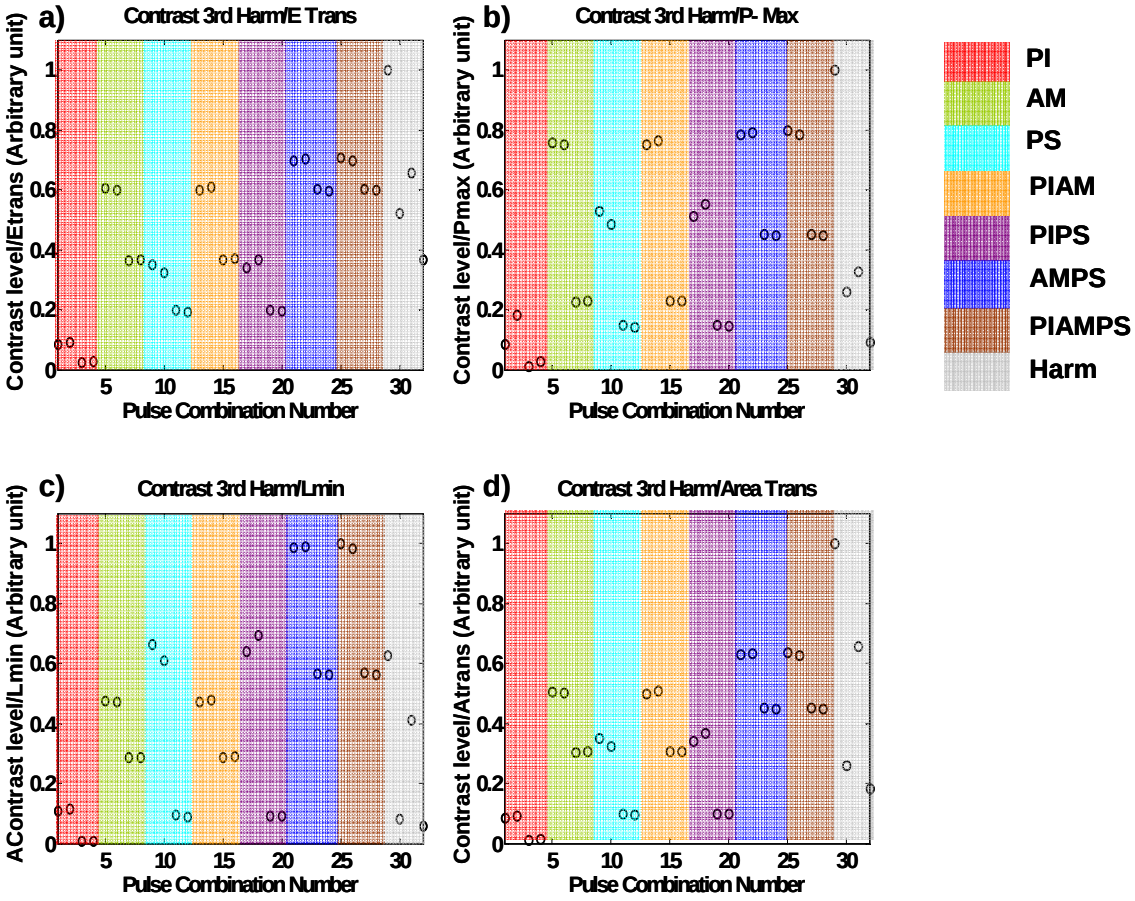

Figure 4-9: a) Third harmonic contrast normalised by the transmitted energy, b) the max transmitted pressure, c) the minimum pulse length used and d) the transmitted pulse area.

Figure 4-9 represents the third harmonic contrast normalised by the pulse characteristics. After normalising by E Trans, P- Max and Area Trans, as shown in Figure 4-9 a), b) and d) respectively, the maximum contrast was obtained for third harmonic imaging. However when the length of the driving pulses was considered, PIAMPS and AMPS provided the best solution (Figure 4-9 c)).

The effect of the multipulse sequence on the noise level was also studied. Depending on the operations needed for the virtual echo construction, the noise level in the residue will vary. For all the pulse sequences tested, the predicted noise level of the residue was calculated using Equation 4.8 and represented in Figure 4-10 a). It can be compared with the standard deviation measured from the simulation, represented in Figure 4-10 b). The noise level was highest for PIAMPS, AMPS and PIAM sequences and lowest for PI and harmonic imaging. Both figures a) and b) have similar relative noise levels. The lower noise level observed in the simulated harmonic contrast imaging compared to the predicted level is due to the fact that during high-pass filtering, some noise was removed at the fundamental. This process is not accounted for in Equation 4.8.

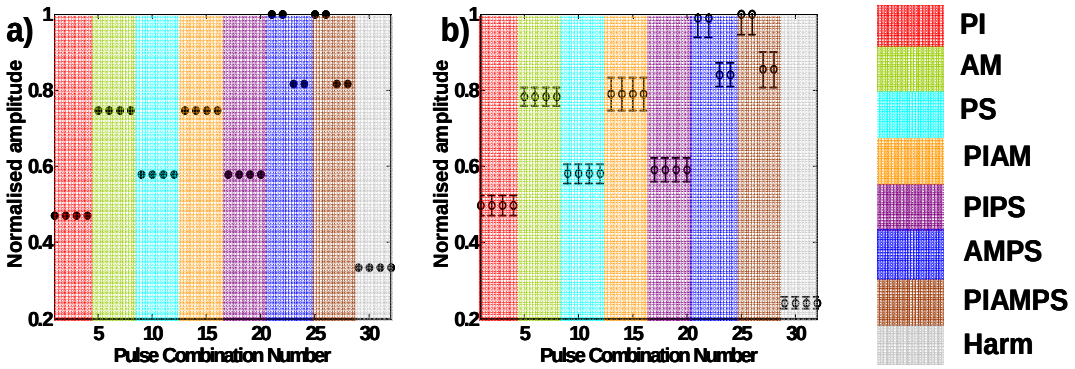

Figure 4-10: Variation of the standard deviation (std) of noise in the residue signal as a function of pulse pair combinations. The stds were all normalised in both graphs by the highest noise level. a) represents the noise levels predicted by Equation 4.8 and b) the averaged noise levels calculated over 20 samples from the simulations.

The contrast to noise ratios (CNR) are represented in Figure 4-11. The total CNR in a) was found to be the highest for harmonic imaging, since this imaging technique had the lowest noise level. Its ratio was 2 dB higher than for PI, 3.2 dB higher than PIPS and 4.6 dB higher than PIAM. PIAMPS performed less well than in Figure 4-3 since it requires more operations for the construction of the virtual echoes and therefore introduced a higher noise level to the residue.

However for fundamental imaging, as shown in Figure 4-11 b), the highest CNR was obtained for PIAM imaging, followed by AM (0.15 dB lower), PIAMPS (0.4 dB lower) and PIPS (0.56 dB lower). Harmonic imaging is non-existent at the fundamental frequency and was therefore not represented on the graph.

The CNR at the second harmonic frequency was highest for PI imaging. It was 2.1 dB higher than harmonic imaging, 2.75 dB higher than PIPS and 5.7 dB higher than PIAM. At the 3rd harmonic component, the CNR was highest for 3rd harmonic imaging.

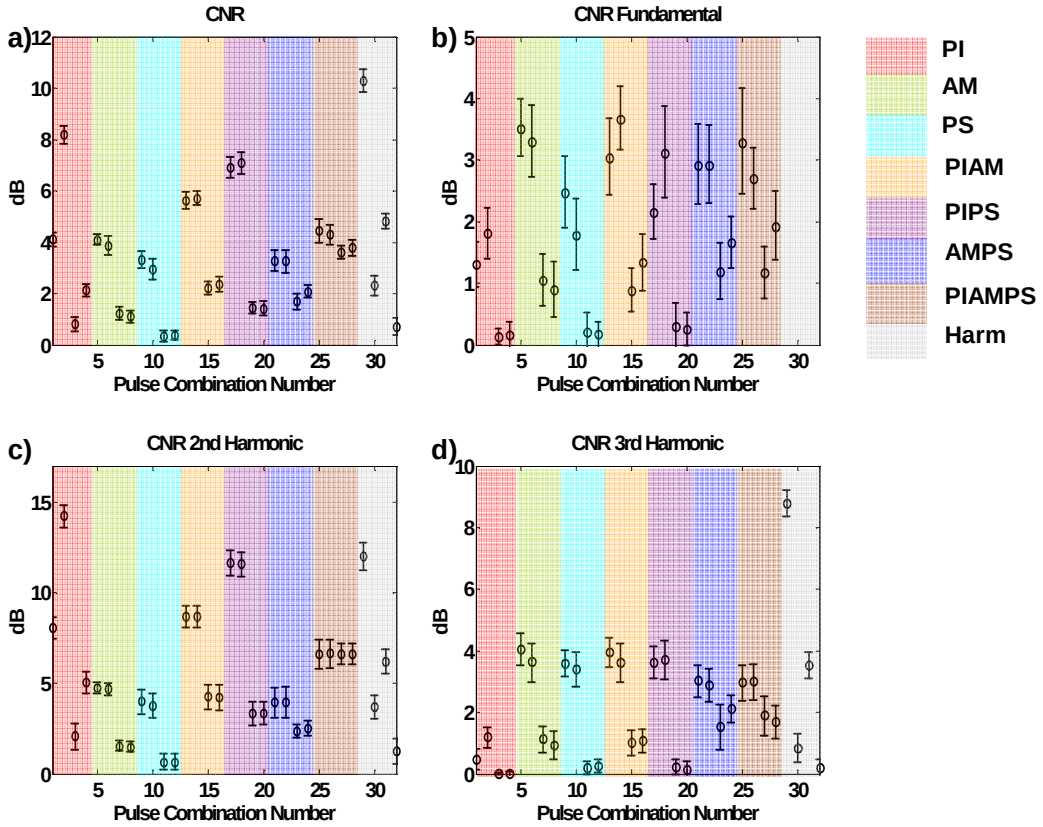

Figure 4-11: a) Total CNR and its decomposition into the three nonlinear harmonics b) nonlinear fundamental, c) second harmonic and d) third harmonic.

4.6 Discussion

4.6.1 Harmonic analysis

Decomposing the contrast into its harmonic components may help to decide on the pulse sequence to choose with regards to the transducer bandwidth. At the second harmonic, the highest contrast was obtained by PI imaging. By comparing Figure 4-3 a) and c) it can be seen that the pulse sequences containing phase inversion achieved the highest level of contrast, and most of the contrast was contained at the second harmonic. This can be explained by the fact that the generation of harmonics is proportional to the square of the incident pressure [44].

However at the nonlinear fundamental, PIAMPS was found to provide the highest contrast. Enhancing the nonlinear fundamental can be particularly useful for bandwidth limited transducers which do not detect second harmonics. Although being 8.7 dB lower than the contrast obtained by PI at the second harmonic, the nonlinear fundamental has also the advantage of improving the sensitivity and tissue penetration

since it is attenuated less than the harmonics. This could prove to be particularly useful for deep tissue imaging.

At the third harmonic the highest contrast was obtained by harmonic imaging. Detecting the 3rd harmonics can add to the contrast [89] and can improve resolution [97]; however it also requires an imaging system with a large enough bandwidth and narrow-band pulses. The use of dual bandwidth probes could enable higher harmonics detection [89]. In this simulation nonlinear propagation and attenuation were not taken into account and the contrast of the third harmonic in a real situation may be lower.

4.6.2 Comparison criteria

This study also revealed that comparing pulse sequences in a fair way can be a difficult task. Since PI (6 cycles, 0.1 MI) was the pulse sequence which achieved the highest contrast but with also the highest transmission energy, the pulse sequences could have also been compared on the of basis equal transmitted energy. However this would have induced the creation of pulse pairs of different peak negative pressure or different lengths. Since the bubble nonlinear scattering is not proportional to the applied pressure [44], compensating for this effect would have been more difficult. Therefore it was chosen to form the pulse sequences with a given set of parameters: two different pulse lengths, two amplitudes, two phases and one central frequency.

To account for the different driving pulse parameters, the contrasts were normalised by the minimum pulse length, maximum peak negative pressure, a combination of both pulse length and peak negative pressure and by the transmitted energy. The choice of these comparison criteria were made with regards to standard clinical applications. Although the different criteria target different imaging aspects, one single aspect may be covered by several criteria. The total transmitted energy for example is related to the patient safety aspect but also includes the peak negative pressure in its calculation, related to the microbubble destruction likelihood only.

In this study the pulse parameters chosen had a limited risk factor for the patient and for the microbubble destruction, since the driving pressures were kept low (under 0.1 MI). However in a general approach consisting in testing many complex sequences, of varying amplitudes, the safety criteria become important.

Figure 4-3 has shown that PIAM, PIAMPS and PIPS were achieving similar total contrast levels. However for the same contrast level, the transmitted pulses had

different energy contents. Indeed, as shown in Figure 4-6, PIAMPS provided the best contrast to energy ratio. Such a pulse sequence should be preferred over PI imaging if the amount of energy transmitted needs to be kept to a minimum. Especially in Doppler imaging, where the pulse repetition rates can be high and the imaging time longer, it may be important to choose an appropriate pulse sequence to obtain a good contrast without transmitting too much energy into the tissue. Accounting for the pulse length, the pulse combinations based on pulse subtraction PIPS and PIAMPS become advantageous. Adding the peak negative pressure into consideration, PIAMPS offered the best contrast to transmitted area ratio.

The contrasts at the different harmonics were also normalised by the same criteria. At the nonlinear fundamental, PIAMPS provided the best total contrast ratios for all the normalisation criteria and at the second harmonic, as shown in Figure 4-8, PIAMPS also provided the best contrast to energy ratio. It has to be noted that the contrast to energy ratio obtained for second harmonic imaging was of similar amplitude than for PI. This can be explained by the fact that PI transmits twice more energy into the medium than harmonic imaging which only needs the transmission of one pulse. Since the contrast in PI is mainly created by the sum of the second harmonic components contained in the two echoes [50], its contrast is doubled compared to second harmonic imaging. Normalising both techniques by their respective transmission energies shows that these techniques perform similarly. However, choosing one technique over the other depends on several factors. Pulse inversion overcomes the trade-off between contrast and resolution, characteristic of harmonic imaging [50]. Indeed, PI allows the transmission of broad-band pulses leading to a better resolution, whereas harmonic imaging requires narrow-band pulses in order to reduce the overlap between fundamental and harmonic frequencies.

4.6.3 Hardware nonlinearities

For imaging systems which cannot from precisely control the transmission parameters, alternative pulse sequences could be used. For example if the phase inversion shows nonlinearities, pulses such as AM, PS, AMPS or harmonic imaging could be used instead. The highest contrast for these alternative sequences was obtained by AMPS, as shown in Figure 4-3. The effect of system nonlinearities was studied by Crocco *et al.* [87] who modelled hardware nonlinearities by adding to the transmitted pulses a component whose carrier frequency is double the pulse carrier and whose envelope is the square of the pulse envelope. He also showed that CPS4 (four pulses with

amplitude coefficient 0.5, -1, 1 and -0.5) was robust against the nonlinearities since it only preserved the third harmonic component.

4.6.4 Effect of noise

White Gaussian noise was added to the echoes and CNRs were calculated. The noise was modelled additive and independent of the pulse transmit parameters and of standard deviation corresponding to an experimentally observed level. However in practice the noise level may also depend on the equipment. Pulses which required most operations in the construction of the virtual echo had the greatest noise level in the residue, as shown Figure 4-10. For example, pulse combination AMPS (n° 21) in Figure 4-10 requires the amplification of E{p_1} by a factor of two, followed by the sum with its time-shifted version. Finally, E_V is subtracted from E{p_2}. PI on the other hand, only requires the subtraction of both echoes, leading therefore to an increase of the standard deviation of the noise level by a factor of sqrt(2). Crocco *et al.* [87] have studied the effect of a random noise on the CTR for CPS [55] and PI multipulse sequences. They have also explained the limiting performance of multipulse techniques with regards to the increase of the noise level during the linear scattering cancellation process. They also studied the effect of body motion and showed that the CPS3 sequence (three pulses sent with amplitude coefficients 0.5, -1 and 0.5) was more robust to noise and tissue motion than PI and CPS4. This additional study could also provide useful information for the nonlinear Doppler sequences.

Harmonic imaging had the lowest measured noise level in simulation since it is not based on any pulse pair sequence but on high pass filtering, which removes noise at the fundamental frequency.

In practice, the signal at the 2nd and 3rd harmonics would also be attenuated, and furthermore the CNR would contain additional contributions from nonlinear propagation through tissue. The bandwidth characteristics would also limit the amount of harmonics detected. The relative high CTR obtained for harmonic imaging shown in Figure 4-11 a) therefore needs to be carefully interpreted.

4.6.5 Effects of ultrasound propagation

Nonlinear propagation and attenuation were not considered in these simulations and would play an important role in estimating the contrast to tissue ratio. Since nonlinear propagation is dependent on the applied driving pulse pressure, the contrast to tissue

ratio would mostly be affected by the higher MI pulses [83]. Nonlinear propagation in a tissue medium could be simulated by solving the Khokhlov–Zabolotskaya–Kuznetsov (KZK) equation to calculate the CTR [98], as it was done by Borsboom *et al.* [56] during the study of pulse subtraction time delay imaging. In their paper the bubble was excited by the driving pulses after they have been propagating in the nonlinear medium and CTRs were calculated. Future studies should incorporate the effect of echo recombination on tissue nonlinearities.

4.6.6 Pulse combinations

It was also shown that when based on linear operations, nonlinear Doppler pulse sequences could be created for the detection of nonlinear scattering and velocity estimation. The pulse sequences tested in this study were restricted to particular cases of the model, corresponding to existing detection modes such as PI, AM, PS, and their combinations, some of which created new imaging modes. More complex modes could be developed, where the driving pulses p_1 and p_2 do not need to be linear combinations of each other. Based on an elementary pulse of one cycle, pulses could be designed containing changes in phase, amplitude and length within the pulse. In order to suppress linear scattering, both resulting echoes need to undergo a combined reconstruction, based on the parameters needed for the elaboration of both pulses. Other contrast modes based on the transmission of more than two pulses as well as coded pulse sequences [99], [100] were not considered in this study. Their combination with these imaging modalities and Doppler could potentially enhance the contrast to tissue ratio. Optimising the CTR by varying the transmission pulse parameters as a function of initially set imaging conditions and equipment constraints would be a future way of choosing the most appropriate pulse for the desired application.

4.6.7 Single bubble simulation

Finally, this study was based on the simulation of one single microbubble. In order to be closer to an *in vivo* situation, the nonlinear response of a bubble population would need to be simulated. The concentration and size distribution of bubbles, depth of imaging may play a role in the CTN ratio. Future *in vitro* work should focus on testing the scattering properties of a bubble cloud to the pulse sequences.

4.7 Conclusion

A generalised nonlinear Doppler approach based on the construction of combined linear pulse pair sequences was derived and tested in a simulation study. The Doppler spectrum for a linear scatterer was shown to be equivalent to a Doppler spectrum originating from a linear scatterer in normal pulsed Doppler. For a nonlinear scatterer, it was shown that the Doppler spectrum can be separated into two regions: one region due to nonlinear scattering only, and one, due to linear as well as nonlinear scattering. The contrast from a single microbubble was obtained for different pulse combinations and the pulse sequences were compared with regards to criteria specific to technical and medical ultrasound imaging requirements.

This work demonstrates that, for a well characterised ultrasound system and a particular clinical application, an appropriate choice of the contrast specific pulse sequence can improve the sensitivity. This work also demonstrates that there is no ideal nonlinear sequence to be used by all scanners, but rather that a dedicated pulse pair has to be designed, and ***can*** be designed, and optimised depending on the technical limitations and the specific clinical application. However an increased complexity of the pulse sequence impacts the sensitivity to noise and an appropriate trade-off must be found between the sophistication of the pulse pair and its final efficiency.

.

Chapter 5 Towards the detection of targeted microbubbles with nonlinear Doppler

5.1 Introduction

The emerging field of molecular imaging with ultrasound offers great potential in the diagnosis of diseases such as inflammation, cancer and thrombus. At the molecular level, cells express specific receptors related to a particular disease. At the sites of inflammation in blood vessels, for example, typical receptor expressions include vascular cell adhesion molecule-1 (VCAM1) and E-selectin [101]. Currently, targeted microbubbles for research purposes are mainly produced by modifying their shells with the introduction of molecules such as biotin that allow the attachment of ligands which can bind to specific receptors. The strong bond which biotin can form with streptavidin is commonly used to attach the ligands to the microbubble. As these ligands can easily be labelled with biotin, they can bind to streptavidin which can as well bind to the biotinylated microbubble shell [17].

The main challenges in the field of ultrasound molecular imaging lie in the design of microbubbles of strong targeting efficiency and specificity. It is also important that microbubbles attached to cells emit a strong enough acoustic signal for clinical imaging. Finally, the strong signal from flowing bubbles obscures the signal from adherent bubbles. Robust techniques for the detection and distinction of attached bubbles from free-flowing bubbles and surrounding tissues are therefore also needed, and not yet fully developed [29].

One of the first signal processing solutions for detecting targeted microbubbles for molecular imaging has been to inject the contrast agents as a bolus and to wait for the clearance of the freely flowing ones before imaging the attached ones [19]. However this process is inefficient as it requires a long waiting time, typically between 8 and 15 minutes for the unbound bubbles to be eliminated. Further techniques, such as the “image-push-image” and the “harmonic” methods [29] are faster as they do not require to wait for the clearance of free flowing bubbles. The first method is based on subtracting images before and after the attachment of agents, which is achieved through radiation force pulses. One drawback of this technique is its inefficiency under

tissue motion conditions, which is a common issue in medical imaging, since the patient is never totally still.

The second technique uses a combination of filters to detect the bound bubbles. A fast-time high pass filter is first used to remove linear scattering tissue. It is then followed by a slow-time low pass filter which acts as an averaging filter over several images in order to suppress the signal of flowing microbubbles and therefore leaving the signal of the bound bubbles. The main drawback of this technique is the rejection of the fundamental signal arising from the attached bubbles during the first high pass filtering, and therefore leading to a weak signal from the targeted bubbles. The most recent techniques are based on the same slow time averaging filtering but incorporate different fast time filtering for the tissue rejection, such as pulse inversion [31], subharmonic filtering [32] or a low frequency pulse transmission and high frequency echo reception [33].

Another approach to improve the detection of targeted bubbles is the study of the difference in responses of the bound bubbles with regards to the free bubbles and to make use of this information in their detection. It has been shown through optical [71], [34], [36] and acoustical [35] observations that targeted bubbles behave asymmetrically when close to a boundary in comparison to free bubbles.

Pulse subtraction Doppler (PSD) was previously shown in chapter 3 to differentiate linear from nonlinear scatterers in the Doppler spectrum, as well as detecting their velocities. The objective of this work is to test PSD on a flow phantom for the discrimination of static microbubbles from free flowing ones and to display both types of bubble information in an image. PSD was then tested on a different phantom using magnetic microbubbles, which have been showing potential for therapeutic applications. Finally, preliminary work was also performed with experimental targeted microbubbles.

5.2 Imaging of static microbubbles

The aim of this study was to demonstrate the feasibility of using PSD for detecting targeted microbubbles. A flow phantom was created to model a flow of microbubble contrast agents in the presence of static and nonlinear microbubbles.

5.2.1 Methods

5.2.1.1 Flow phantom circuit

A flow phantom was constructed enabling the circulation of flowing SonoVue^{TM} contrast agents as well as the trapping of static microbubbles inside the upper wall. The phantom was assembled with a double layer of a thin latex tube (9 mm in diameter, 0.2 mm thickness), allowing the injection and capture of contrast agent modelling targeted bubbles, as shown in Figure 5-1.The flow phantom setup consisted of the same elements as described in section 3.3.2. The four following cases were considered during the experiment:

- The tube without stuck bubbles and without flowing bubbles,
- The tube with stuck bubbles and without flowing bubbles,
- The tube without stuck bubbles and with flowing bubbles,
- The tube with stuck bubbles and with flowing bubbles.

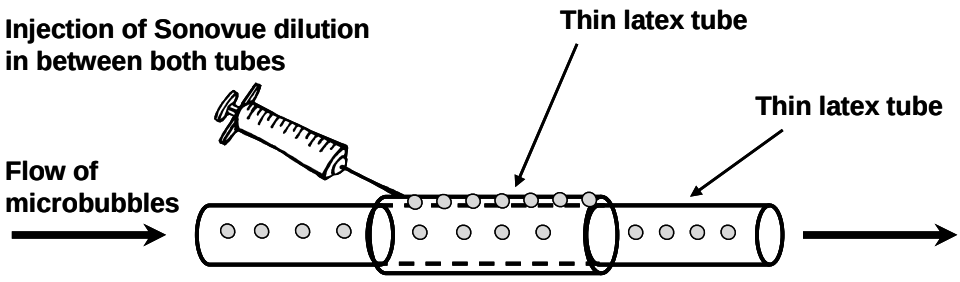

Figure 5-1: Experimental flow phantom which allows an injection of static contrast agents at the upper wall.

The tube was positioned in a water bath at the focus of a L14-38 linear probe of the Sonix RP 500 research scanner (Ultrasonix Medical Corporation, BC, Canada). The probe was mounted in the water bath at an angle with the tube of 55 ± 5^{o}, and was used to transmit predefined PSD pulse sequences and receive the echoes. The flow rate was set via the flowmeter (flow rate range: 200-3000 mL/min, EW-32458-42, Cole-Parmer, Hanwell, London) to 800 cm^3/s, corresponding to an expected mean velocity of 21 cm/s.

5.2.1.2 Ultrasound exposure

The pulse parameters used were the following: the centre frequency of the pulses was set to 5 MHz; the power level was set to correspond to a peak-negative pressure of 170 kPa and an MI of 0.07. Higher powers were avoided as they produced nonlinear

scattering from the tube walls. The PSD pulses alternated between one short p_1 pulse and one long p_2 pulse, constructed as the sum of p_1 and its time-shifted version. The reflected echoes from a linear scattering membrane of the two transmitted pulses are shown in Figure 5-2 a). Figure 5-2 b) shows the cancellation of the echoes after the construction of the virtual echo.

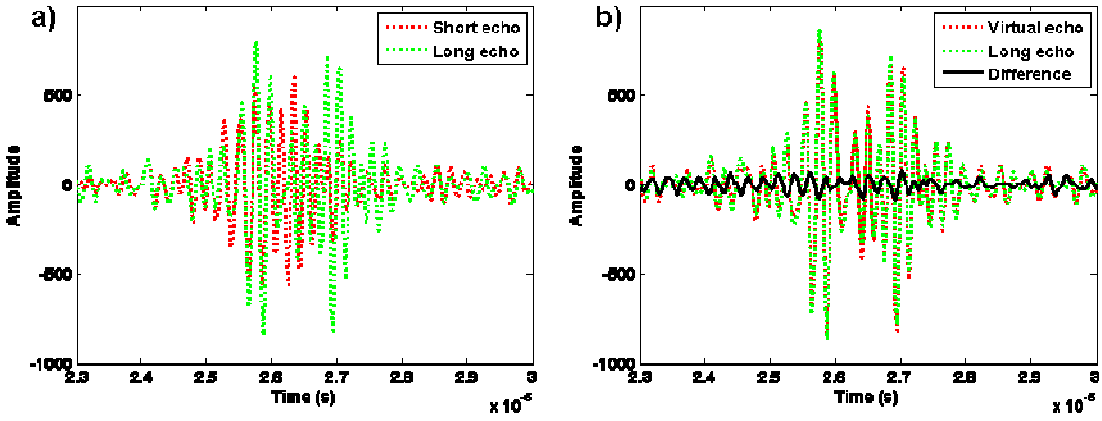

Figure 5-2: a) Received echoes from a linear interface for the short pulse p_1 (red dotted line) and long pulse p_2 (green dotted line); b) Residue signal (black line) after subtracting the virtual echo (red dotted line) from the long echo (green dotted line).

Each Doppler sequence consisted of 64 pulses and the sequence was repeatedly fired along the 14 central lines of the probe. For one line, the beam was formed by using 32 probe elements for transmission and reception. A B-mode image was also created within the sequence along the 52 central lines. The arrangement of the lines is shown in Figure 5-3. The choice in the number of B-mode and Doppler imaging lines was a compromise between the different Doppler acquisition parameters. The PRF between each pulse was defined by the depth of imaging which was set to 4 cm and additional time required by the system to perform the acquisitions. The PRF was therefore calculated to be 13.3 kHz, as the product of the frame rate (14 frames/s) with the number of lines acquired for one frame.

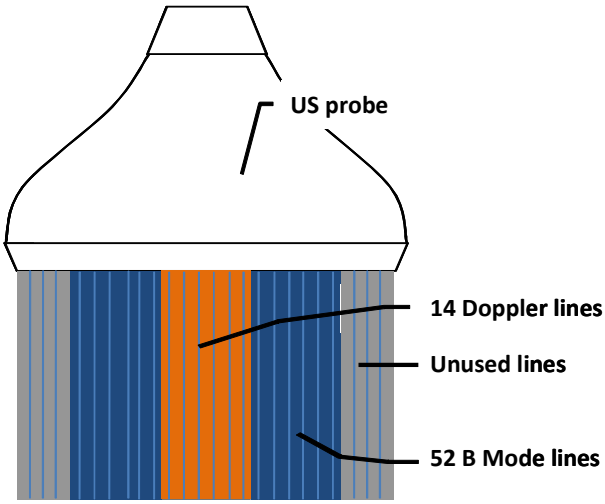

Figure 5-3: Arrangement of the Doppler lines and B-Mode lines in the ultrasound probe. Each beam along one line was fired using 32 elements for transmission and reception.

5.2.1.3 Doppler echo processing

The 64 collected Doppler echoes were then post processed for each line with Matlab™ to obtain dual band Doppler spectra at different depths. The detailed steps of the pulse subtraction Doppler processing are explained in section 3.2.2. Such processing splits the Doppler spectrum in two sub-bands. In one frequency band of the spectrum, the Doppler frequencies are indicative of nonlinear scattering only and the other band the spectrum contains the linear scattering as well as some nonlinear scattering of the bubbles. The imaging of the blood flow typically forms a peak in the appropriate band of the spectrum whose location (i.e. the Doppler frequency) is proportional to the velocity of the scatterers. The Doppler frequency information from the linear peak can be used to calculate the velocity of the scatterers at different depths. Static scatterers were defined as scatterers having a Doppler frequency of zero (Hertz). The amplitude in the nonlinear part of the spectrum at frequency zero thus indicates the presence of static nonlinear scatterers. This process was then repeated to the 13 other lines in order to obtain a 2-dimentional velocity map as well as a map of nonlinear static scattering.

5.2.2 Results

A drawing of a B-Mode image of the tube and its different elements is shown in Figure 5-4 a). A standard colour Doppler image was calculated from the measured Doppler data and is shown in Figure 5-4 b), displaying a grey scale B-Mode image of the tube as well as the red colour coded velocity map of the flow of contrast agents. The expected maximum velocity of 42 cm/s set by the flowmeter was found within the range

of the maximum velocity of 37 cm/s (± 7 cm/s, due to the uncertainty of the angle between the probe and the flow direction) measured in the centre of the tube. From this colour Doppler image only, information about the presence of stuck microbubbles at the wall cannot be drawn.

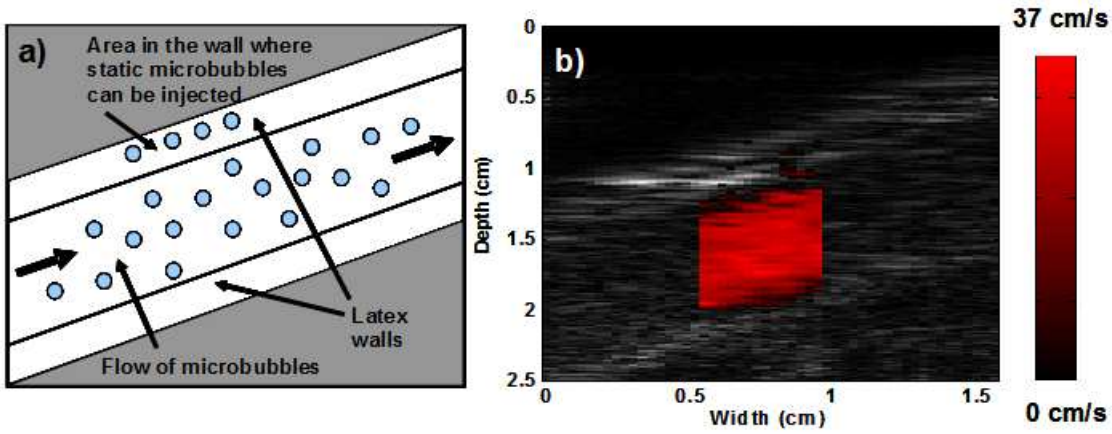

Figure 5-4: a) Schematic representing the latex tube flow phantom and b) its corresponding colour Doppler image constructed as an overlay of a velocity map in red onto a grey scale B-Mode image. The maximum velocity measured was 37 cm/s.

The information contained in the nonlinear region of the Doppler spectrum enables the discrimination of non-moving nonlinear microbubbles from flowing microbubbles and tissue. Comparing Figure 5-5 a) (no stuck bubbles and no flow) and Figure 5-5 b) (stuck bubbles and flow) shows that in no flow conditions the nonlinear signal from immobilised microbubbles can be detected. By averaging the intensity of the pixels over a region of the tube wall, it was shown that the intensity of the stuck microbubbles in b) was on average 10dB (±1dB) higher than when the bubbles are absent. In the presence of a microbubble flow, as shown in Figure 5-5 c) and Figure 5-5 d), the intensity of the nonlinear scattering was also around 10dB (±1dB) higher than in the absence of stuck bubbles in c).

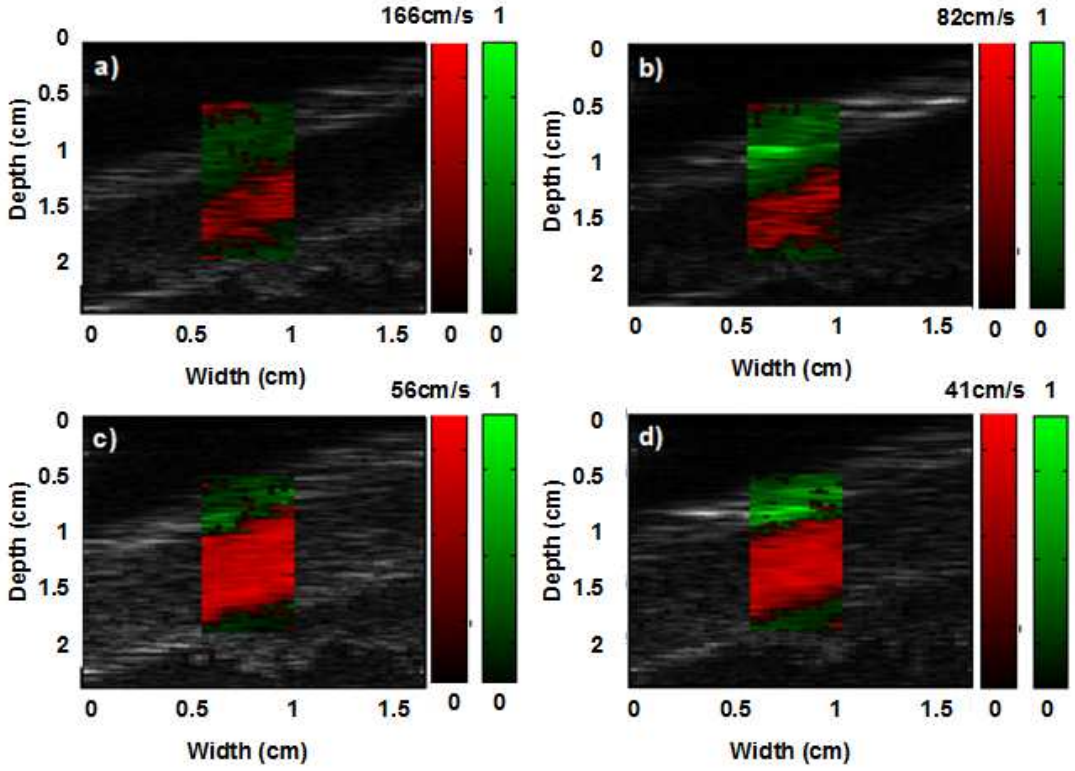

Figure 5-5: Grey scale B-Mode images with the velocity map overlaid in red and the nonlinear static scattering amplitude in green. The four tubing cases were represented. In a) no stuck bubbles and no flow, b) stuck bubbles and no flow, c) no stuck bubbles and flow, d) stuck bubbles and flow. The colour maps of the nonlinear scattering have been normalised to the maximum measured nonlinear amplitude. The velocity scale shows the maximum measured velocity. The high velocity values obtained in no flow conditions are due to the velocity estimation with a noise signal and do not represent an actual velocity.

5.2.3 Discussion

The PSD technique was used on a flow phantom to test the discrimination of stuck bubbles from freely flowing bubbles and tissue. This discrimination in this study relies on the static and nonlinear properties of the static agents. The flow phantom was made of three different elements: stuck bubbles injected at the tube walls, flowing bubbles and tubing, scattering linearly. This phantom model was used as a starting point for testing PSD, with the expectation that targeted microbubble solutions would become available for testing. However in the real context of a blood vessel, the targeted microbubbles would be bound to the endothelial cells of the vessel wall through ligands [102]. The number of bound bubbles per surface area may be far less than in the experiment here, leading to a weaker signal from the bubbles. Also, numerous studies have examined the difference in scattering of a bound bubble to a surface and a free bubble. It was for example shown that bubbles in vicinity of a surface oscillate asymmetrically [36] and experience damped oscillations as well as a resonance frequency shift [34]. The response signal from the bubbles in between the two tubes of

our phantom may therefore differ from the one of targeted bubbles. However the technique may not be affected by these differences since it is strictly based on the nonlinear and static properties of the adherent agents.

One main limitation of the technique is the separation between slowly moving scatterers near the vessel wall and static stuck microbubbles. In this nonlinear Doppler detection technique, static scatterers were defined as scatterers having a Doppler frequency of 0Hz ± F_{res}. The ability to separate slow motion from no motion is limited by the frequency resolution, F_{res} (F_{res} = 1/T), which depends on the length of the observation interval T. The observation interval corresponds to the product of the number of samples constituting the Doppler signal (N) and the time interval between each sample (T_i,). F_{res} can therefore be written as a function of the PRF: F_{res} = PRF/N. In this experiment, the PRF used was 13.3 kHz and the number of Doppler samples acquired per line was of 64. The frequency resolution was therefore of 208Hz, corresponding to a minimum detectable velocity of 5.6 cm/s (± 0.7 cm/s) at an incident angle of 55^o (± 5^o). Increasing the observation time by increasing the number of samples would improve the frequency resolution and reduce the overlap of slowly moving scatterers; however this would also reduce the frame rate.

This limitation is a common issue for the current techniques, which use averaging over multiple pulses in order to suppress the decorrelation between the frames, such as in [29] and [31]. In 2010, Hu *et al.* [33] considered different types of low-pass filtering approaches and set low-pass Doppler cut-off frequencies depending on the order of the filters in order to suppress the flowing bubble signal. But this method suffers the same limitation as the choice of the cut-off frequency will be a trade-off between rejecting stuck bubbles and including free ones.

Tissue motion could be less of a limiting factor compared to the existing techniques. In fact, in the nonlinear Doppler method the movement of tissue can be detected and its velocity measured within the linear band of the spectrum. The peak corresponding to the same Doppler shift in the nonlinear band would therefore contain the information about the nonlinear scattering. This nonlinear signal is comprised of the scattering from stuck microbubbles and a fraction of the slow moving ones within the velocity resolution cell, as well as possible tissue harmonics arising from nonlinear propagation. This process expresses an intrinsic “anti-clutter rejection filtering” property of non linear Doppler techniques such as PSD. The available detection techniques based on slow-pass filtering [29], [31], [32] or [33] do not measure the flow rate and would need realignment algorithms to compensate for tissue movement.

One fundamental difference between the PSD technique and other techniques is that PSD rejects flowing bubbles within a series of successively acquired Doppler echoes and performs velocity measurements at the same time, whereas the slow-time filtering techniques perform the averaging over several frames.

The choice of the tissue-rejection filtering can also be optimised. In [29] and [31] which present high-pass filter and pulse inversion sequences respectively, only the second harmonic signal of the attached bubbles is used. In [33], which presents high frequency imaging, the subharmonic signal of the bubbles is conserved. A judicious choice of the nonlinear pulse sequence, as described in chapter 4 could potentially increase the signal received from the targeted bubbles. Furthermore, if monodisperse microbubbles [103] become widely used as targeted agents, the nonlinear pulse sequence should play an important role.

5.2.4 Conclusion

This study has shown through a simple flow phantom the applicability of the nonlinear Doppler technique, PSD, for the detection and discrimination of static microbubbles from freely flowing ones and tissue. Different types of information could be displayed at the same time: nonlinear Doppler information could be overlaid on standard colour Doppler images.

The following sections aim at testing the technique on more realistic phantoms. The studies include work with magnetic bubbles and preliminary work with biotinylated microbubbles.

5.3 Imaging of magnetic bubbles

Recent studies have developed magnetic microbubbles by incorporating magnetic nanoparticles into their shell. These magnetically active bubbles have been shown, in vitro and under static conditions, to enhance gene delivery when in the vicinity of cells and when exposed to acoustic and magnetic fields [104]. These bubbles could provide a tool for therapeutic applications, as they can potentially be targeted to regions of disease to release drugs. Pulse subtraction Doppler sequences were here tested on a flow phantom made of magnetic microbubbles.

5.3.1 Methods

5.3.1.1 Microscopy images

Magnetic microbubbles were prepared by Dr. Eleanor Stride, from the Ultrasonic Group at University College London. The bubbles were magnetised through a sonication process by incorporating magnetic suspensions into their phospholipid shell, as described in [104]. The bubble population was then observed under a microscope (inverted microscope, type 090-135-001, Leica Microsystems, UK) at X40 magnification. Sixty images were captured and the size distribution of the bubble population was estimated following the sizing and counting methods described in [105]. The effect of a 1.5 T magnet array on the bubbles was also studied optically by introducing the magnet at the top of the microscope slide. A series of pictures was then taken over time.

5.3.2 Flow phantom circuit

A flow phantom was created by adapting the wall-less flow phantom model proposed by [106]. Agar (agar powder, Sigma-Aldrich, UK) was used as tissue mimicking material at a concentration of 3%. The agar powder was first mixed with distilled water to the desired weight per volume ratio, and the solution was heated up until close to its boiling point. It was then left to cool down to approximately 60ºC before it was being poured into a mould. The mould was made of a 10 cm x 5 cm x 4cm plastic box through which a plastic tube of 1 cm in diameter had been inserted longitudinally. Connectors were glued at each end of the box, which the plastic tube was taken out through when the solution had solidified.

The phantom was then connected through the connectors to a flow circuit, consisting of a pump (Eheim Universal Rotary Pump, model 1048) and a flowmeter (EW-32458-42, Cole-Parmer, Hanwell, London). It was then immersed in a water tank.

5.3.2.1 Magnet

A Halbach array consisting of five rectangular permanent magnets (10 mm x 310 mm x 325 mm, supplied by NeoTexx, Berlin, Germany) of transversal magnetisation 1.5T was positioned underneath the flow phantom, at less than a centimetre from the centre of the tube cavity. More details about the magnet can be found in [104].

5.3.2.2 Ultrasound exposure

Care was taken to place the probe of a Sonix RP 500 research scanner (Ultrasonix Medical Corporation, BC, Canada) at a minimum distance of 8 cm from the magnet in order to avoid any undesirable effects on the electronics of the scanner. A schematic of the wall-less flow phantom setup is represented in Figure 5-6.

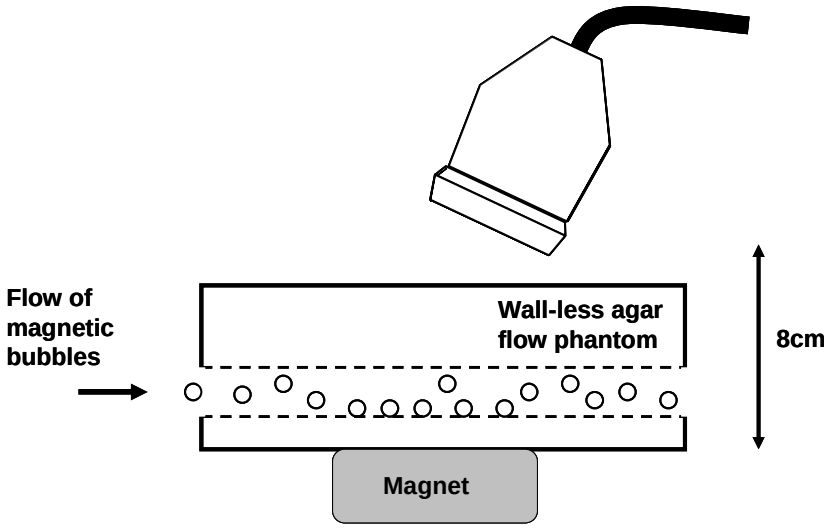

Figure 5-6: Experimental setup of the wall-less agar phantom used to target magnetic bubbles to the bottom wall.

Since the probe was tilted to allow Doppler imaging, the depth of imaging was set to 8.5 cm, corresponding to a frame rate of 20 frames per second. The driving frequency was set to 6.6 MHz and the MI to 0.06.

5.3.2.3 B-mode cine loop capture

A bolus of 200 µL of magnetic microbubbles was injected at the entrance of the first connector and the flow was turned on to 100 cm^3/min, corresponding to a mean velocity of 2.1 cm/s. Videos of the microbubble flow entering the region of the magnetic field were recorded.

5.3.2.4 RF capture

A similar agar phantom containing a square cavity was constructed for the RF data acquisitions in static conditions. The magnet array was placed at 0.5 cm underneath the cavity. This phantom allowed the imaging of a square cross-section and the bottom wall of the cavity to be a straight line. 200 µL of magnetic bubbles were injected inside the cavity. Once the bubbles were immobilised by the magnet at the bottom wall, the freely floating ones were removed by carefully flushing some saline through the cavity.
The research scanner was programmed to fire PSD sequences. Using the 128 elements of the linear probe, RF data was acquired for the empty cavity and in the presence of the immobilised bubbles at two different MIs, 0.07 and 0.35. Using the raw data, two dimensional images of the cavity were generated, as well as their corresponding nonlinear response (residue signal for one pulse pair) with and without the presence of magnetic bubbles.

The static scattering of a bolus of magnetic bubbles (200 µL) was also observed without the presence of a magnetic field by using PSD sequences on a latex tube (1cm in diameter) containing free magnetic bubbles and Doppler spectra were plotted as described in chapter 3.

5.3.3 Results

5.3.3.1 Bubble size distribution

The size distribution of one magnetic bubble population is presented in Figure 5-7. The bubbles had a mean diameter of 1.8 µm (±1.03 µm) and a concentration of 1.2 x 10^8 bubbles/mL. The reproducibility of the size distribution was not tested in this study and it is possible that the distribution varied from batch to batch.

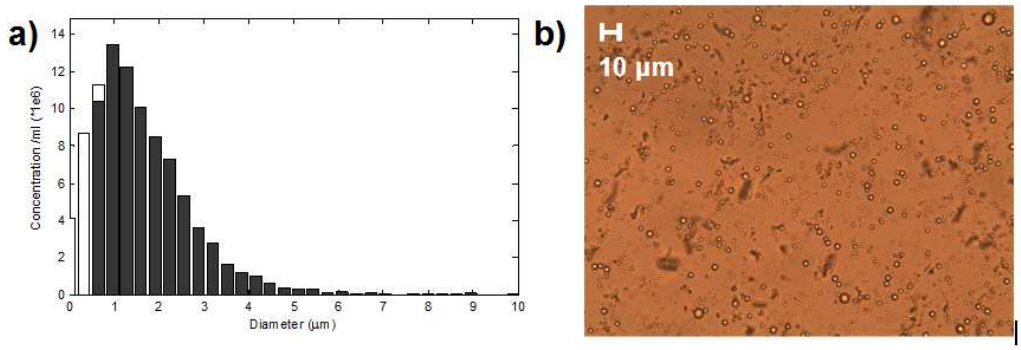

Figure 5-7: a) Size distribution of the magnetic bubble population, courtesy of Dr Helen Mulvana. The bubbles outside the range 0.5 to 10 µm were excluded. The original data is included in the plot as clear bars. b) A microscopy image of the bubbles X40 at time zero, before the introduction of the magnet.

5.3.3.2 Bubble behaviour under microscope

The microscopy images on Figure 5-8 show the displacement over time of the magnetic bubbles under a magnetic field. The images show that the bubbles form agglomerates with each other and some magnetic material aligns along the magnetic field lines. Three areas were circled in different colours and show that from frame to frame the bubbles move towards the magnet at different speeds. The blue circle points at a few bubbles which remain static. The red circled bubble appears to move at a greater speed than the green circled one.

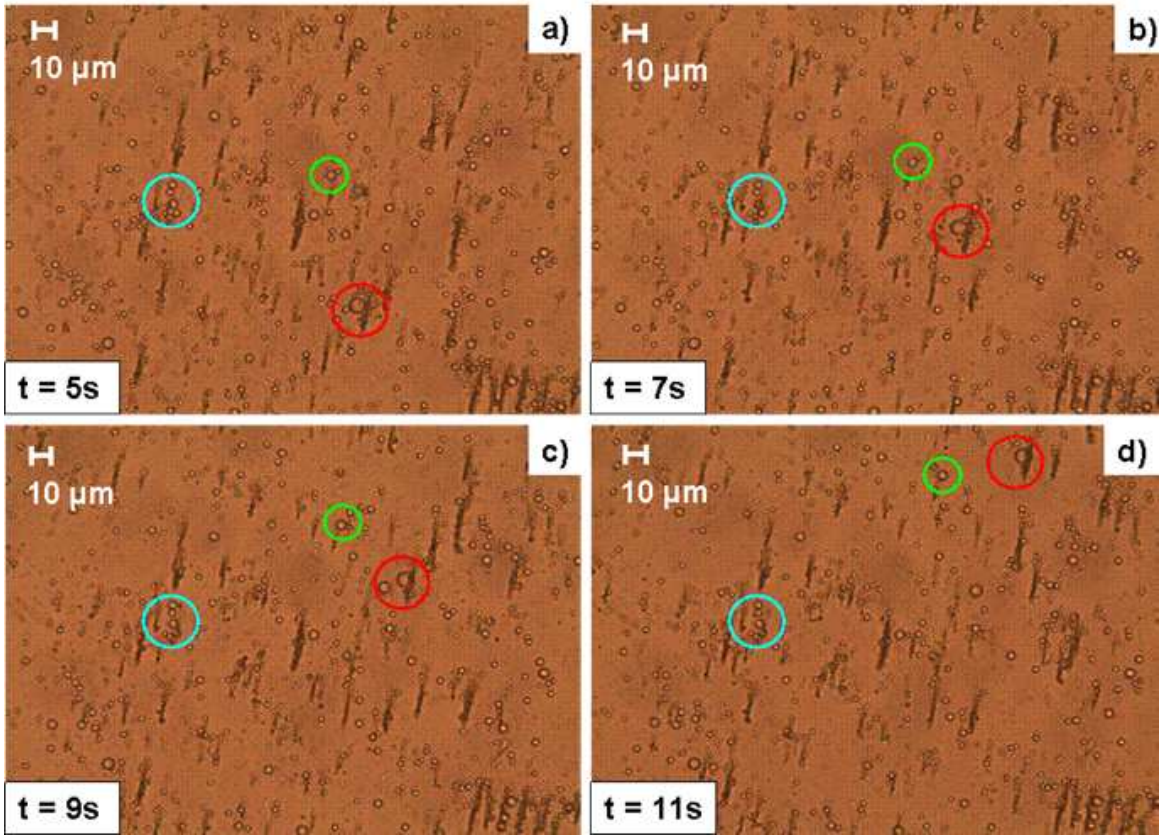

Figure 5-8: Microscopy images showing the response of magnetic bubbles over time to a magnetic field. The magnet was positioned at the top of the microscope slide.

5.3.3.3 B-mode cine loop capture

The arrival of the bolus of magnetic microbubbles in the cavity is shown on the video snapshots on Figure 5-9, frames b) to d). In Figure 5-9, the empty tube before the flow is turned on is shown in b). When the bubbles flow into the cavity, they deflect from a straight trajectory and travel towards the magnet where they eventually stop, as shown on c). In frame d), after the bolus has passed, the cavity is left with the top and bottom walls being brighter, compared to the original image b). The signal from the upper wall is due to the buoyant microbubbles. The signal at the bottom wall is due to the magnetic bubble immobilisation under the magnetic force.

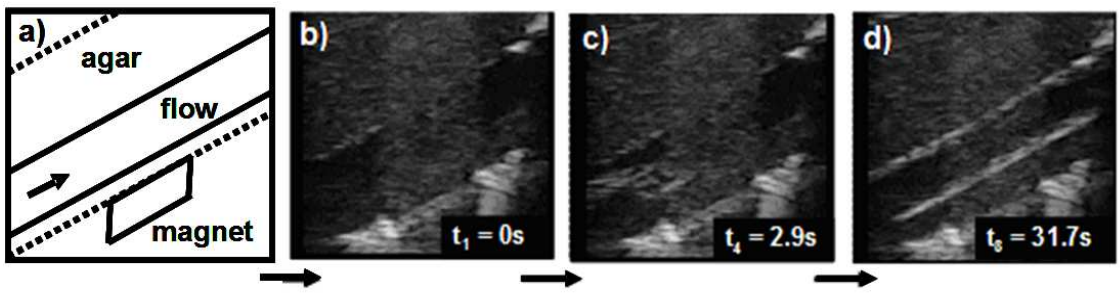

Figure 5-9: Frames taken at different time intervals showing the arrival of the magnetic bubbles in the tube and their attachment to the bottom of the tube. a) Diagram of the elements of the video images. b) Cavity before the flow is turned on. c) Bubbles flowing in and deviating towards the bottom of the tube. d) Bubbles immobilised at the bottom of the tube wall and floating at the top.

5.3.3.4 RF data

The presence of the magnetic bubbles in the phantom is also detectable by an increase in the scattering intensity on the B-mode images before and after immobilisation of the bubbles. By comparing the B-mode images on Figure 5-10 a) and b), both taken at an MI of 0.07, an increase of 30 dB (±10dB) is measured over a region at the location of the bubbles, due to a localised increase in bubble concentration, compared to the same region in the absence of bubbles. However on the corresponding nonlinear image in b), no nonlinear scattering is apparent at the immobilised bubble location. By using a higher MI of 0.35, a nonlinear residue is detectable in d). However at this high power, it is likely to be due to bubble destruction rather than to nonlinear scattering [107].

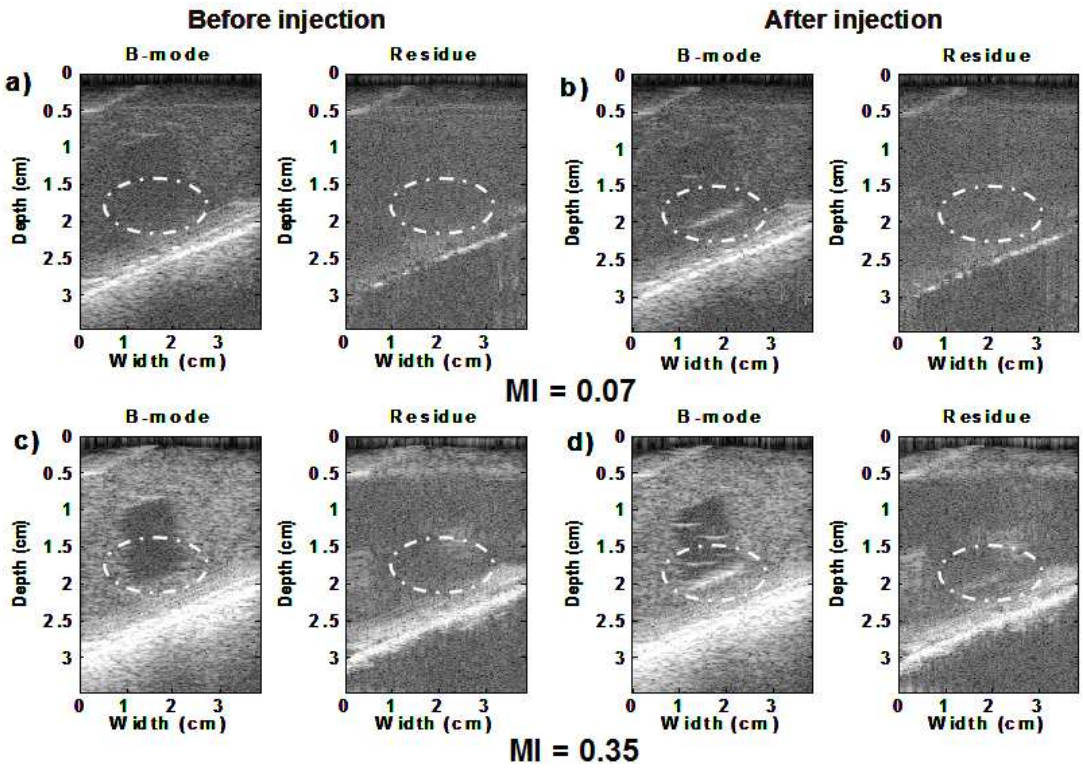

Figure 5-10: B-mode images of a square cavity cross-section with their corresponding nonlinear residue images. a) Without magnetic bubbles at an MI of 0.07 and b) with immobilised magnetic bubbles at the bottom of the cavity at the same power. Images c) and d) were done at an MI of 0.35. All the images were plotted with the same grey scale.

The Doppler spectrum in Figure 5-11 b) shows that the scattering of free and static magnetic bubbles is detectable inside the tube, at the location of 0Hz by comparison to the empty tube in Figure 5-11 a), where only the scattering from the tube walls is apparent. However no nonlinear scattering is detectable at PRF/2. Both observations from Figure 5-10 and Figure 5-11 seem to show that the magnetic bubbles used in this study scatter linearly, whether immobilised at a wall by the magnet or if free.

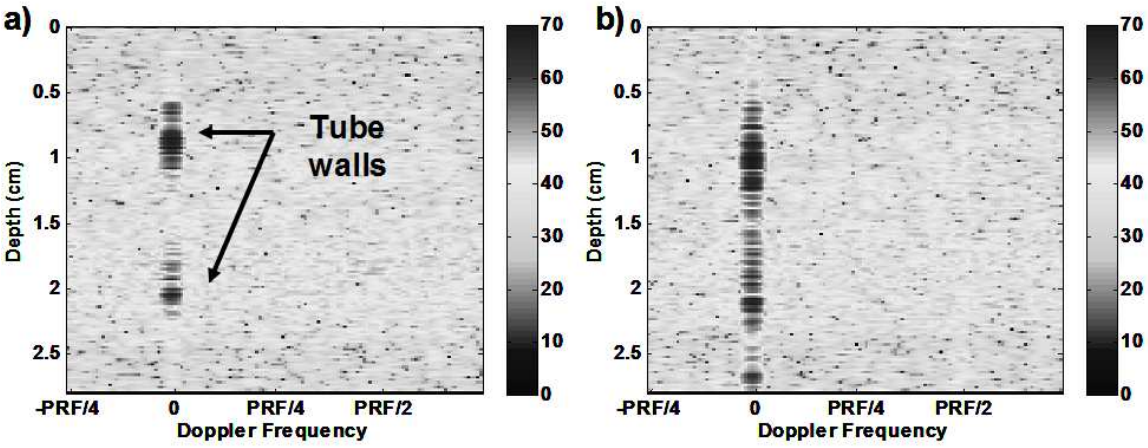

Figure 5-11: Nonlinear Doppler spectra as a function of depth after PSD processing was applied for a) an empty latex tube and b) the tube containing a solution of static magnetic bubbles. Linear signal is detectable at 0Hz. However in both cases no nonlinear signal is detectable at PRF/2.

5.3.4 Discussion

The microscopy images in Figure 5-8 show that the bubbles move with different speeds towards the magnet. This could be due to different levels of magnetisation and chemical composition such as the amount of magnetic nanoparticles contained in the shell or the gas/oil ratio. The video data in Figure 5-9 also shows that some of the bubbles did not attach to the bottom wall and either flew out of the field of view or floated up to the top of the vessel wall. The reason for the varied bubble trajectories can be explained by the numerous forces acting on them. The major forces acting on a bubble include: a magnetic force, a drag force, buoyancy, gravity and possibly radiation force. Depending on the chemical properties of the bubbles, such as the amount of magnetic nanoparticles or shell material and depending on its physical properties such as its size, resonant frequency and finally, depending on the ultrasound and magnetic field characteristics, all the bubbles will experience different forces and therefore will have different trajectories. Stride *et al.* [104] and Tortoli *et al.* [108] have described some of these forces in more details.

Regarding the scattering properties of the magnetic bubbles, Figure 5-9 shows that the bubbles can be detected in the B-mode image by a change in intensity. However there is no apparent nonlinear scattering of the bubbles whether immobilised at the wall or free, as shown by Figure 5-10 and Figure 5-11. As shown in Figure 5-8, the bubbles form aggregates under a magnetic field. The effect of microbubble coupling with neighbouring ones has been studied by [109], who showed that clustered microbubbles

could emit significantly fewer second harmonics than free bubbles. Other optical studies on the behaviour of microbubbles near a boundary or when coupling to other bubbles [34] showed that they experienced a change in their resonant frequency and in amplitude compared to free ones. These amplitude and resonant frequency differences could be used to develop contrast specific modes for a better detection of the immobilised bubbles. Stride *et al.* [110] have suggested modelling approaches of these bubbles in order to better understand their behaviour with regards to their chemical composition. Future *in vivo* work would also require a better understanding of the magnetic bubble acoustical behaviour and their immobilisation under different flow rates. Knowledge of the magnet strength required and its positioning with regards to the desired focus seem to constitute important preliminary steps. Finally, the acoustic parameters such as driving pressure, frequency and exposure time can be optimised.

5.3.5 Conclusion

In this study, several aspects of magnetic microbubbles were characterised: their behaviour under a magnetic field was assessed with microscopy observations and video recordings were done in flow conditions. It was found that the bubbles move at different speeds and some could be immobilised at the vessel wall. In this study the attached bubbles enhanced the signal at the wall by 30 dB (±10dB). Future work should study the effect of the magnet strength and flow rates on the degree of immobilisation.

Applying the PSD sequences to static magnetic bubbles has shown the bubbles to scatter linearly when next to a wall or if free. In this case PSD is not a suitable technique for distinguishing immobilised bubbles from flowing ones since they are not detectable in the nonlinear band of the Doppler spectrum. Future work should address this issue and could aim at varying the chemical composition of the microbubbles in order to increase their nonlinearity. Although many practicalities still remain, this experiment constitutes a step forward for future *in vivo* work.

5.4 Preliminary work on biotinylated bubbles

Some preliminary work was also performed with biotinylated microbubbles. The following experimental work was performed on in-house made microbubbles.

5.4.1 Methodology[2]

5.4.1.1 General properties of the biotinylated microbubbles

In-house developed microbubbles were made of a perfluorocarbon gas core encapsulated within a phospholipid surfactant polymer shell. The bubbles were prepared by Dr. Charles Sennoga, from the Ultrasound Group at Imperial College by sonicating a solution containing the microbubble shell chemicals in the presence of octafluoropropane gas [111]. By also incorporating biotin into the microbubble shell during preparation, the microbubbles can specifically attach to surfaces which are being coated with streptavidin. This process is depicted in Figure 5-12. The shell of these microbubbles was also labelled with a DiI fluorescent marker during preparation.

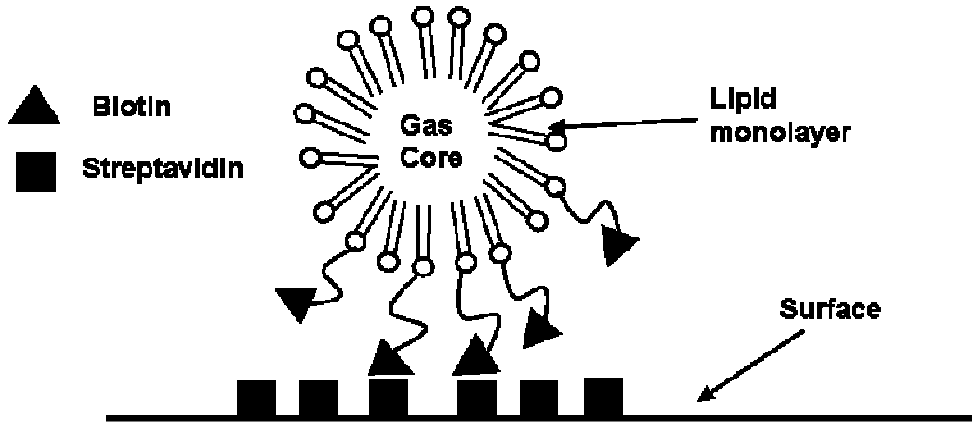

Figure 5-12: Biotinylated microbubble and its targeting to a streptavidin coated surface.

In order to attach a biotinylated bubble to a surface, the surface can be coated beforehand with streptavidin. The procedure for coating a surface with streptavidin is described below.

5.4.1.2 Coating of a surface with streptavidin

The streptavidin protein (Invitrogen, S888 Paisley UK) comes delivered as a 5mg solution in a vial, which needs to be stored at -20ºC. This quantity of streptavidin can be used for several surface coatings. Therefore it is important to aliquot the solution into several samples which can be stored and taken out of the freezer independently whenever needed.

[2] This methodology was developed by Dr. Charles Sennoga, from the Ultrasound Group, Imperial College London

First, twenty pieces of 1 mL Eppendorf tubes need to be sealed in small autoclave bags in order to be sterilised. The streptavidin aliquots can then be prepared in a tissue culture hood. One millilitre of sterile Phosphate Buffered Saline (PBS) is added to the 5 mg of streptavidin. Using the autoclaved tubes, twenty aliquots of volume 50 µL and concentration 5 mg/mL can be prepared, using the entire volume of streptavidin. The tubes are then sealed with parafilm and stored at -20ºC in the dark.

In order to coat a chosen surface with streptavidin, the surface first needs to be thoroughly washed with PBS. All excess PBS is then removed, but the surface should not be dried. The aim of this step is to ensure that the residual PBS does not affect the concentration of the protein added.

Depending on the size of the surface area which needs to be coated, one or more streptavidin aliquots can be used. Each 50 µL aliquot needs to be defrosted and diluted into 1950 µL of sterile PBS in order to make a 0.125 mg/mL solution of streptavidin.

A grease pen was used to draw a contour on the surface, delimiting a region of interest on which the streptavidin solution could be placed and would stay confined. The solution is then carefully added on the defined area. The surface was placed beforehand in a container, in which some tissues soaked in PBS have been placed. This prevents the surface from drying out. The surface is then incubated in a fridge at 4ºC for 24 hours.

In order to prevent non-specific (usually electrostatic) binding of biotinylated microbubbles to uncoated regions, these regions can be blocked with Bovine Serum Albumin (BSA). The BSA is a protein blocking buffer whose aim is to fill in the regions of the surface area which have not been coated with streptavidin. A 5% BSA solution is therefore prepared by dissolving 12.5 g of the powder in 250 mL of deionised water. After incubation, the streptavidin is removed from the surface by aspiration with a micropipette. The solution of 5% BSA is then added on the surface area. The container is placed back in the fridge for one hour incubation at 4ºC in the dark. This streptavidin surface coating process is also described in [112], [113].

5.4.1.3 Washing of microbubbles

On the day produced, biotinylated microbubbles were suspended in a saline solution containing biotin protein residues which were not incorporated in the shell. In order to avoid the binding of these remains to the streptavidin on the coated surface and

therefore in order to increase the number of microbubbles attaching to the area, these residues need to be removed [113]. This can be done by centrifuging the microbubbles, using a temperature controlled bucket-type centrifuge (Hettich Rotanta 460R, Newport Pagnell, UK). A solution of microbubbles is placed in the centrifuge which is programmed to work at 4ºC, for 5 minutes and at a rotary speed of 1200 RCF. These settings were similar to the ones used by Sugiura *et al.* [113]. The centrifuge induces the denser materials such as the biotin residue and other debris to go to the bottom and the microbubbles to float up. After the spinning, a volume of the bottom solution (around half of the initial volume in the Eppendorf) is very carefully aspirated with a syringe and discarded. An equivalent volume of PBS is then added back to the microbubble solution. This centrifuging process is then repeated three times. This final highly concentrated solution of washed microbubbles can now be aliquoted into several Eppendorfs for conservation and later use. After filling the Eppendorfs with the washed bubbles, these are frozen instantaneously in liquid nitrogen and then stored at -20ºC.

5.4.1.4 Targeting of microbubbles to the surface

After the BSA incubation, the BSA is removed and the surface area washed with PBS. A solution of washed microbubbles was then diluted (concentration not known) and applied on the surface. Whenever possible, the surface should be inverted to allow microbubble floatation against the surface and therefore a possible increase in adhesion to the biotin. After a few minutes any unbound microbubbles can be removed with chilled PBS.

5.4.2 Imaging

For the purpose of constructing a flow phantom with targeted bubbles, the material on which the bubbles need to adhere needs to be tested beforehand. One way to check the adhesion was to observe the microbubbles optically.

5.4.2.1 Microscopy

The procedure described in the methodology section 5.4.1 has been followed and first applied to a Petri dish surface. Washed biotinylated microbubbles were shown to attach to the surface coated with streptavidin, but not to the control section which was left uncoated. Pictures taken with a bright field microscope (inverted microscope, type 090-135-001, Leica Microsystems, UK) and magnification X40 are shown in Figure 5-13. They represent the attachment of targeted microbubbles to streptavidin on a) and no attachment on the control surface on b).

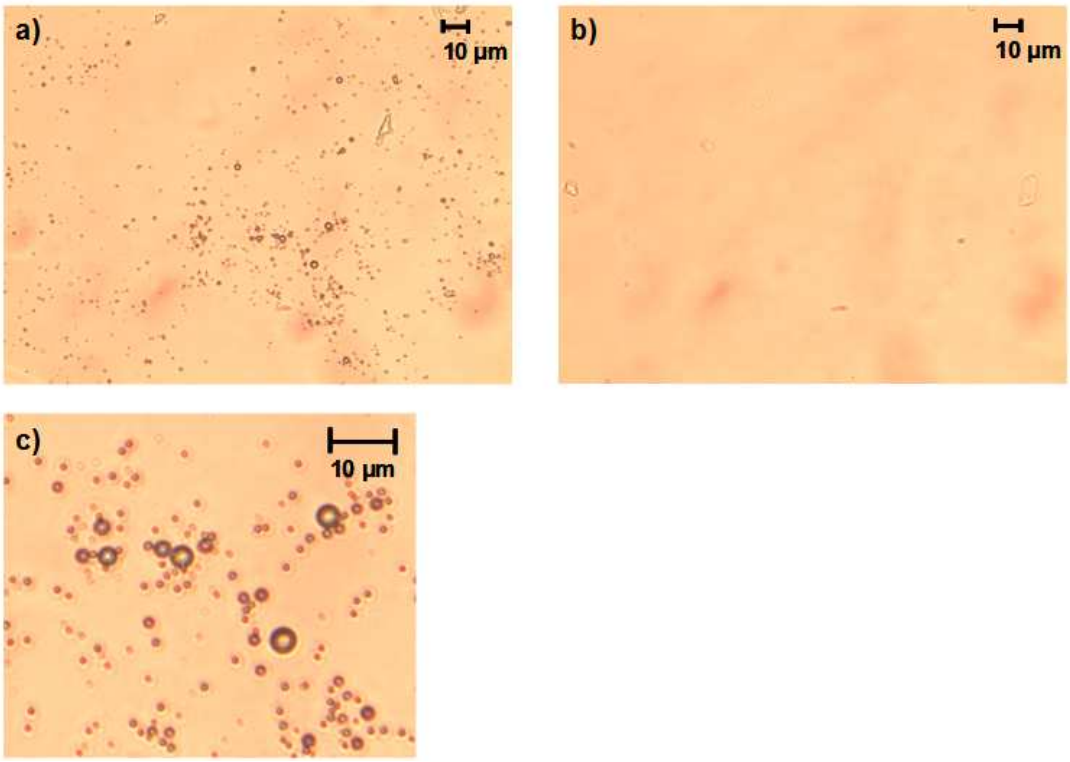

Figure 5-13: a) Biotinylated bubbles attached to the surface and b) bubbles not attached on the control surface. c) Zoom on the central area of the surface containing attached bubbles.

For the imaging of targeted microbubbles in the context of a flow, it is desirable to be able to attach the bubbles to other types of surfaces. The nonlinear Doppler experiments described in section 3.3.2 used a thin latex tube (0.2 mm wall thickness) in the flow experiments. Therefore this material was first tested as to whether microbubbles could be targeted to its surface. The tube was first cut open and one sample of the latex tube surface was taken and coated with streptavidin. Another sample was left uncoated for the control. The surfaces were then treated as the Petri dishes were and were then observed under the microscope. Figure 5-14 shows images taken from the optical observations of the latex tube coated with streptavidin a) and for the control experiment b).

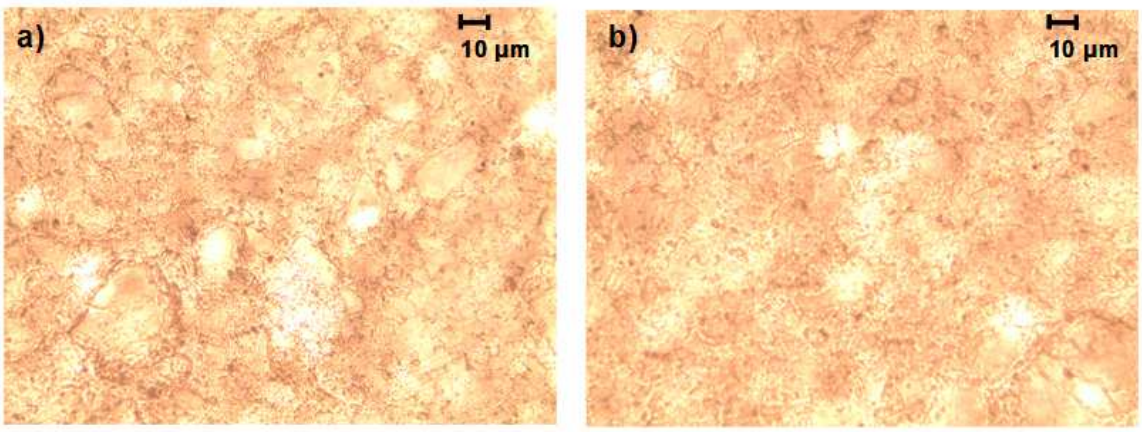

Figure 5-14: a) Streptavidin coated area on which attached microbubbles are expected. b) Control area where no bubbles are expected.

It is difficult to clearly see any microbubbles in the image a) of Figure 5-14. The irregular microstructure of the latex surface does not allow a clear optical observation of any potentially attached microbubbles. Both the streptavidin coated surface and the control look very similar. The use of another optical observation was therefore necessary to draw any conclusions concerning the attachment of microbubbles on latex.

5.4.2.2 Confocal microscopy

Another possible way of viewing the targeted microbubbles was to make use of their fluorescent properties. The shells of the microbubbles were dyed during preparation with DiI, a fluorescent tracer. DiI is known to be excited at 549 nm and to emit fluorescence at 565 nm. Its absorption and emission spectra are represented in Figure 5-15.

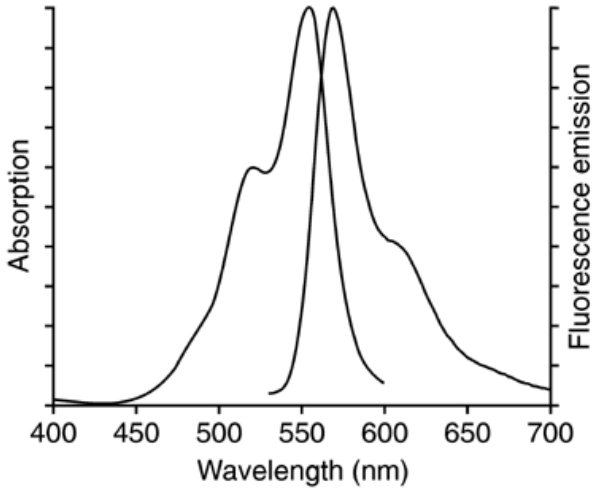

Figure 5-15: Absorption and emission spectra for DiI dye bound to a phospholipid bilayer membrane. This information was found on the Invitrogen website.

The microbubbles were first placed on a microscope slide and imaged with the confocal microscope (type SP5, Leica Microsystems, UK) by recording multiple slices parallel to the slide. An image of a slide is represented in Figure 5-16.

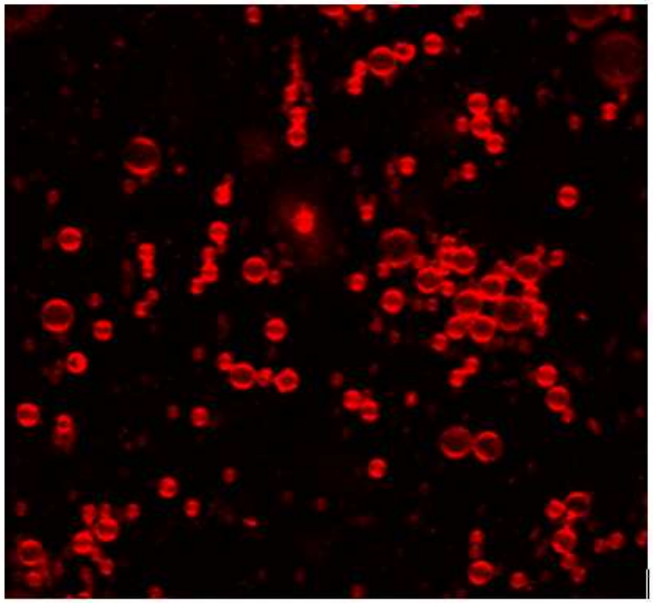

Figure 5-16: Fluorescence microscopy of DiI dye incorporated in the membrane of microbubbles. X63 objective (glycerol immersion)

The same recording was repeated on a streptavidin coated sample of the latex tube. A solution of biotinylated bubbles was applied on the surface and the microbubbles were allowed to float against the surface by inverting it. After a few minutes the unbound

microbubbles were removed by flushing with PBS. The confocal images did not show any remaining bubbles on the tube and it was therefore deduced that the biotinylated bubbles could not attach to latex. No reference was found on bubbles attaching to latex.

The attachment of biotinylated microbubbles was also tested on other materials, such as agar (agar powder, Sigma-Aldrich, UK), gelatine (Gelatin, G2500, Type A 300 bloom, Sigma-Aldrich, UK), and sylgard (Sylgard 184, Dow Corning, Midland, MI), which could enable the future construction of a wall-less flow phantoms as done by Needles *et al.* [32]. It was shown that the bubbles attach to these two materials. As represented in Figure 5-17, the bubbles did attach to the streptavidin coated agar a) but not for the control agar. The same observation (not shown here) was made for gelatine and sylgard surfaces.

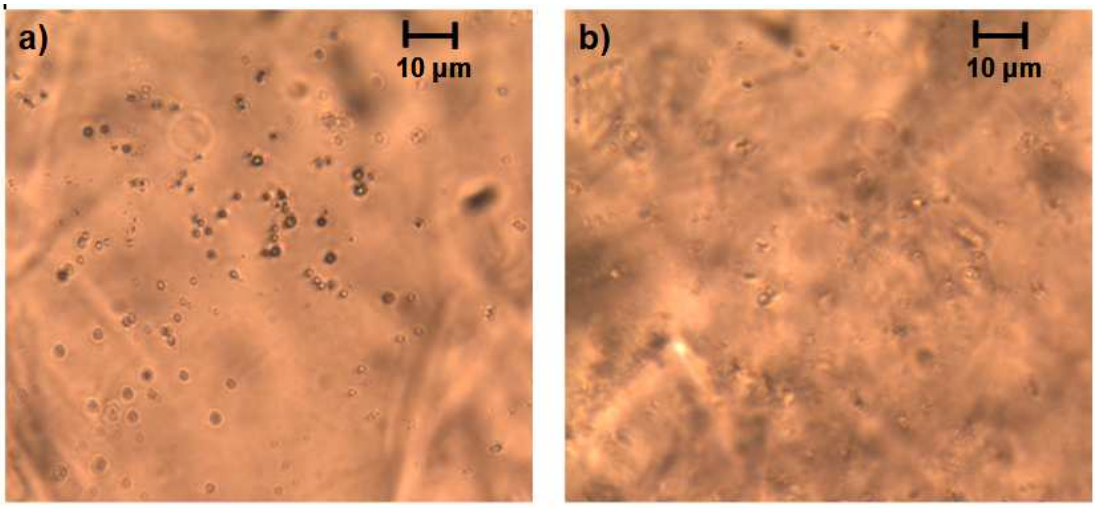

Figure 5-17: Attachment of biotinylated bubbles to an agar surface. a) Streptavidin coated surface and b) Control surface.

5.4.3 Conclusion

Some preliminary work was done with in-house made targeted microbubbles. The detailed process for attaching biotinylated bubbles to a streptavidin coated surface was described. Different types of surfaces were tested and the bubbles were shown to attach to a petri dish, agar, gelatine and sylgard, however not to latex. This information is useful knowledge for the design of flow phantoms for modelling targeted microbubbles in the presence of flowing ones and tissue. Immediate future work should test the nonlinear Doppler technique with such phantoms.

5.5 General conclusion

The first steps towards the detection of targeted contrast agents were undertaken by testing the nonlinear Doppler technique on several *in vitro* flow phantoms. First, an in *vitro* phantom was designed in order to assess pulse subtraction Doppler for the detection and discrimination of static nonlinear microbubbles in the presence of free flowing ones. It was shown that pulse subtraction Doppler enables such discrimination and the practicability for *in vivo* situations was discussed. The pulse subtraction Doppler sequences were then tested on a phantom containing magnetic bubbles. It was shown that the magnetic bubbles could be immobilised through a magnetic field to a specific region of interest under flow conditions. The bubbles also showed to be acoustically detectable and to scatter linearly at the driving pressure used. Although many practicalities still remain, this experiment constitutes a step forward for future *in vivo* work. Finally, preliminary work regarding experimental biotinylated microbubbles and their attachment to streptavidin coated surfaces was presented.

A better understanding of the acoustic behaviour of targeted bubbles when bound to a surface could enable their selective detection through the design of specific imaging sequences. The second approach taken in this thesis considered the influence of a membrane on the behaviour of bubbles in its vicinity.

Chapter 6 Oscillations of microbubbles in contact with an elastic wall

6.1 Introduction

Cardiovascular diseases are the main cause of death in the US and most European countries [114]. When heart problems are detected, atherosclerosis, the origin of the disease is usually at an advanced state. Therefore, early detection of inflammation which leads to the formation of plaques on the vessel walls could enable an early diagnosis of cardiovascular disorders. A change in the biomechanical properties of vessel walls such as Young's modulus, thickness and stiffness, have been shown to be related with the development of fibrosis and vascular calcification [115]. In the carotid artery, for example, the Young's modulus was shown to increase with age and with the development of atherosclerosis [116]. For healthy subjects the elastic modulus of the carotid artery was measured to increase on average from 60 kPa to 200 kPa between 30 and 65 years. For patients suffering from atherosclerosis the elastic modulus varied from 60 kPa to 500 kPa over the same age period.

Non-invasive techniques such as ultrasound elastography have been used to assess the elastic properties of arteries in order to detect early stage atherosclerosis [117]. Recent advances in contrast agent ultrasound molecular imaging have allowed the rapid quantification of vascular inflammatory changes that occur at different stages of atherosclerosis, by attaching VCAM-1 targeted microbubbles to endothelial cells of aortic plaque [18]. Although the binding is specific to the targeted molecular expression, imaging cannot currently selectively observe the attached bubbles, and one of the remaining challenges of ultrasound molecular imaging is the distinction of the targeted microbubbles from the background signal made of freely circulating bubbles and tissue [80]. A better understanding of the acoustic response of bubbles in the vicinity of a compliable vessel wall can improve the selective detection of targeted bubbles. At the same time, the understanding of the acoustic signature of near-wall microbubbles may allow the estimation in patients of the evolution of the stiffness of the vessel walls through time.

Rayleigh-Plesset-based simulations of microbubble dynamics usually assume that microbubbles remain spherical when surrounded by an infinite fluid or when contained

in a large vessel [118], [78]. However the behaviour of microbubbles in close proximity to a boundary such as a vessel wall has been the subject of many studies.

Theoretical simulations have shown the presence of a wall or tube to shift the microbubble resonance frequency. Sassaroli *et al.* [119] have shown how the resonance frequency of bubbles when confined in small rigid tubes decreases below its free value. When decreasing the vessel radius or when increasing the bubble radius, the natural frequency of the bubble decreases compared to the bubble in an unbound field. These results in the case of a rigid vessel were confirmed by Qin *et al.* [120] who also studied the additional cases of a bubble confined in a compliant vessel and in a vessel of increasing stiffness. They found that within an elastic vessel, the natural frequency of the bubble increases with decreasing vessel size and increases with increasing bubble size for a constant vessel diameter. With increasing stiffness, the study suggests that the natural frequency of the bubble oscillation decreases with the development of tumours. Martynov *et al.* [121] developed a simplified theoretical model for the dynamics of a bubble confined in an elastic blood vessel, based on a two degree of freedom system. They showed that the bubble in a finite-length elastic vessel can be characterised by two different natural frequencies. The study suggests that in order to maximise the microbubble response in long elastic vessels, they should be excited at frequencies higher than the frequency of an unconfined bubble. Experimental studies of a bubble confined in a range of different vessel diameters confirmed the simulations results from [122]. Caskey *et al.* [122] showed through high speed camera recordings at high insonation pressures that microbubbles in a tube with a diameter of the order of the bubble size expanded less than if confined in a larger tube. A similar study by Thomas *et al.* [123] at low driving pressures showed the same tendency.

High speed camera observations of the oscillations of single adherent microbubbles have shown their radial maximum expansion to be smaller than for free bubbles [71]. The same observation was made for a bubble in close vicinity of a wall [72] where it was shown that its oscillations were reduced by 50%. However these results disagree with a study on a population of targeted microbubbles [35], where it was found that the adherent microbubbles strongly increased the fundamental signal. It was suggested that this increase could be due to the coherent summation of scatter.

However, no experimental or numerical studies have been reported regarding the behaviour of microbubbles in contact with a large vessel wall of varying stiffness. This work is aimed at studying experimentally and numerically the effect of vessel wall

stiffness on the resonant frequency or amplitude of microbubbles oscillating in contact with the wall.

6.2 Methods

In this section a description of the methods used for the experiments and the simulations is provided. The fabrication process of the elastic membranes is first described as well as the measurement of their Young's moduli. The optical experiment and the numerical simulation are then detailed.

6.2.1 Preparation of the membranes

Two membranes of different Young's moduli (E) were prepared with Sylgard, a silicone elastomer (Sylgard 184, Dow Corning, Midland, MI). The Sylgard comes in a kit made of two components and is normally prepared by mixing a base with a curing agent in the ratio of 10:1, according to the manufacturer. The elastic properties of the material can be changed, as studied by [124] and [125] by using different mixing ratios. The aim was to prepare membranes with stiffness close to human blood vessel stiffness. Fung [126] showed that the Young's modulus can vary from 70 kPa to 450 kPa for the human aorta for example. Three mixing ratios were chosen, 1:10, 1:20 and 1:30, in accordance with the ratios found by [124] and [125], which should give Young's moduli close to human blood vessel stiffness.

To prepare the Sylgard membranes, the protocol described by [124] was followed with some additional alterations. To obtain the membranes with different elastic moduli, the silicon elastomer base and curing agent were mixed thoroughly for 10 min with a magnetic stirrer at the three different mixing ratios. Since air bubbles were trapped during mixing, the mixture was degassed with a vacuum pump for two hours. The three different mixtures were then poured into separate Petri dishes (100 mm square Petri dishes, PDS-140-120K, Fisher, UK) creating a layer of approximately 1 mm in height, within the range of typical vessel thicknesses [127]. Care was taken to minimise air entrapment during this process. The Petri dishes were then placed into the vacuum pump up to 1 hour for a second degassing. The Petri dishes were finally placed on a horizontal bench and the mixtures left to solidify for 48h. The chosen mixing ratios were then validated by measuring their Young's moduli.

6.2.2 Tensile testing of the membranes[3]

In order to study the effect of wall stiffness on the microbubble oscillations, both the Young's modulus and the thickness of the wall were varied.

The Young's moduli of the Sylgard membranes were determined by conducting tensile measurements [128] on an Instron materials machine (Instron 5565, High Wycombe, Buckinghamshire, UK), with accompanying Merlin software. Figure 6-1 shows the principles behind the tensile test on a sample.

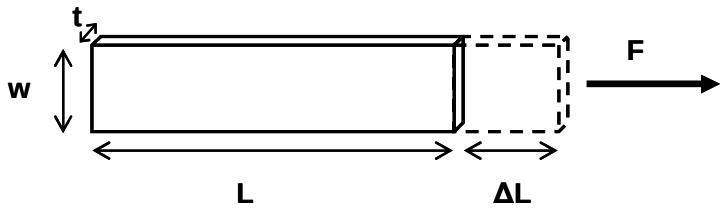

Figure 6-1: Tensile test principle on a membrane of dimensions w, t, and L (width, thickness and length). ΔL represents the elongation of the sample under the applied force F.

Eight samples were prepared for each of the membranes by cutting each into 60 mm x 10 mm (length, width) rectangles. Their thicknesses were measured separately with a calliper. Each sample had thicknesses varying between 0.5 mm and 1.3 mm.

A 10 N load cell was used and calibrated before the measurements and the tensile testing was conducted at a rate of 10 mm min^{-1}. The samples were mounted onto testing clamps as shown in Figure 6-2.

[3] The tensile tests were performed with the help of Dr Spyros Masouros from the Biomechanics Group, Department of Bioengineering, Imperial College London.

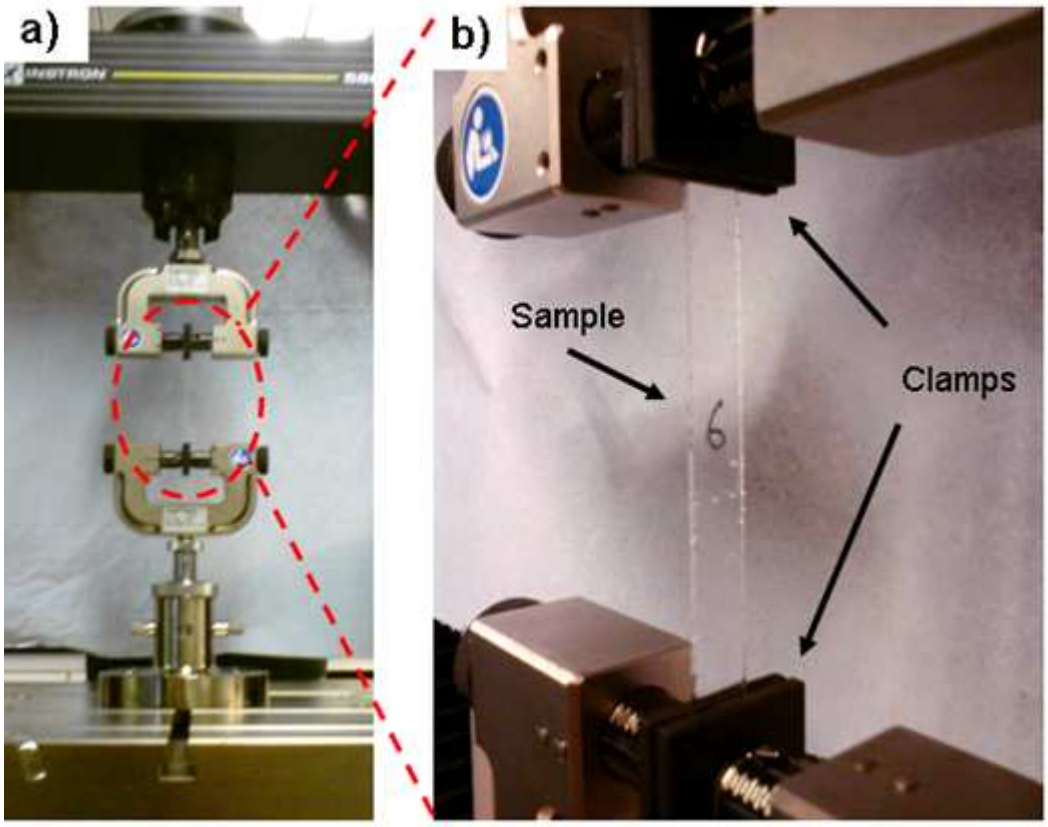

Figure 6-2: Picture of the membrane tensile test setup. a) Overall view of the setup, and b) a zoom on a Sylgard sample during testing.

The load-displacement curves were recorded and the experiment was automatically terminated if rupture of a sample occurred or when the maximum load was reached. The load-displacement curves obtained for the three different mixing ratios are represented in Figure 6-3.

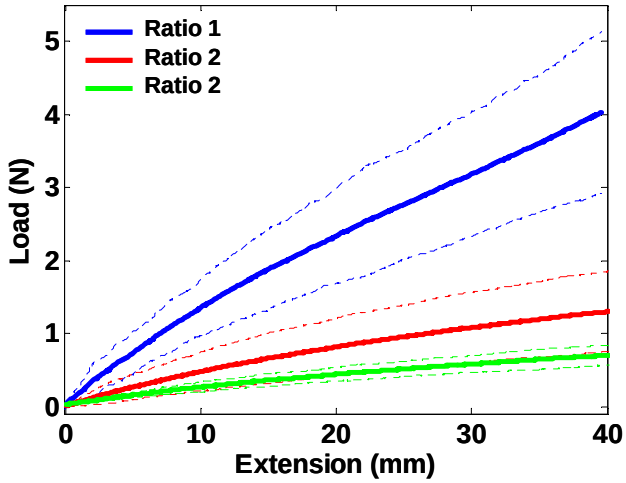

Figure 6-3: Load-elongation curves for the three Sylgard membranes prepared with different mixing ratios, ratio 1 (1:10), ratio 2 (1:20) and ratio 3 (1:30). The mean and standard deviation are represented by straight and dotted lines respectively.

The stiffness, k, was calculated from the slope of the load-elongation curves in the linear portion between 15 mm and 25 mm, following Equation 6.1.

$$k = F / \Delta L \qquad \text{Equation 6.1}$$

where F is the applied force and ΔL the elongation of the sample.
The Young's modulus E could then be deduced for each sample using the stiffness by accounting for the sample dimensions, as shown in Equation 6.2.

$$E = kL / A \qquad \text{Equation 6.2}$$

where L is the length of the sample and A is the cross sectional area the force was applied on.

For the three membranes, the Young's moduli E_1, E_2, E_3 were calculated to be 517.45 kPa (±92.10 kPa), 135.43 kPa (±12.83 kPa) and 80.26 kPa (±10.53 kPa) respectively. These values are within the range of the blood vessel Young's moduli values found in the literature for healthy and unhealthy subjects [116]. The membrane of lowest Young's modulus E_3 was dismissed at this stage as it was very fragile and tore too easily.

Table 6-1: Stiffness of the three samples used for the optical recording

	Sample 1	Sample 2	Sample 3
E, Young's modulus (kPa)	517(±92.10)	517(±92.10)	135(±12.83)
t, Thickness (mm)	1.20 (±0.03)	0.60 (±0.02)	1.21(±0.05)

Three samples of different stiffness k, as reported in Table 6-1 were chosen by selecting membranes of different Young's moduli and thicknesses. The samples were cut into identical squares of 2.5 cm x 2.5 cm. The thickness of each membrane was measured with a calliper and was found to be within the range of typical large human vessel thicknesses [127].

6.2.3 Experimental set up

In order to assess the response of microbubbles close to a membrane of varying stiffness, experiments were done using an optical setup as shown in Figure 6-4. Details of the experimental procedure can be found in [79]. A high speed camera (Cordin 550, Cordin, Salt Lake City, USA) capable of capturing 62 frames at 4 million frames per second allowed the optical recordings of the oscillations of individual microbubbles. A X10 field lens (MonoZoom 7 Optical System, Leica Microsystems GmbH, Wetzlar,

Germany) was used to couple a X100 microscope objective with a long working distance objective of 1.5 mm to the camera. This optical setup was coupled to an acoustic setup consisting of a single element ultrasound transducer (Videoscan, Panametrics-NDT, Waltham, MA, USA) with a centre frequency of 0.5 MHz which was powered by a power amplifier (ENI 240L, ENI Technology Inc, NY, USA) driven by an arbitrary waveform generator (AWG2021, Sony-Tektronix, ShangHai, China). The transducer had an aperture size of 3 cm and was geometrically focussed to 4 cm.

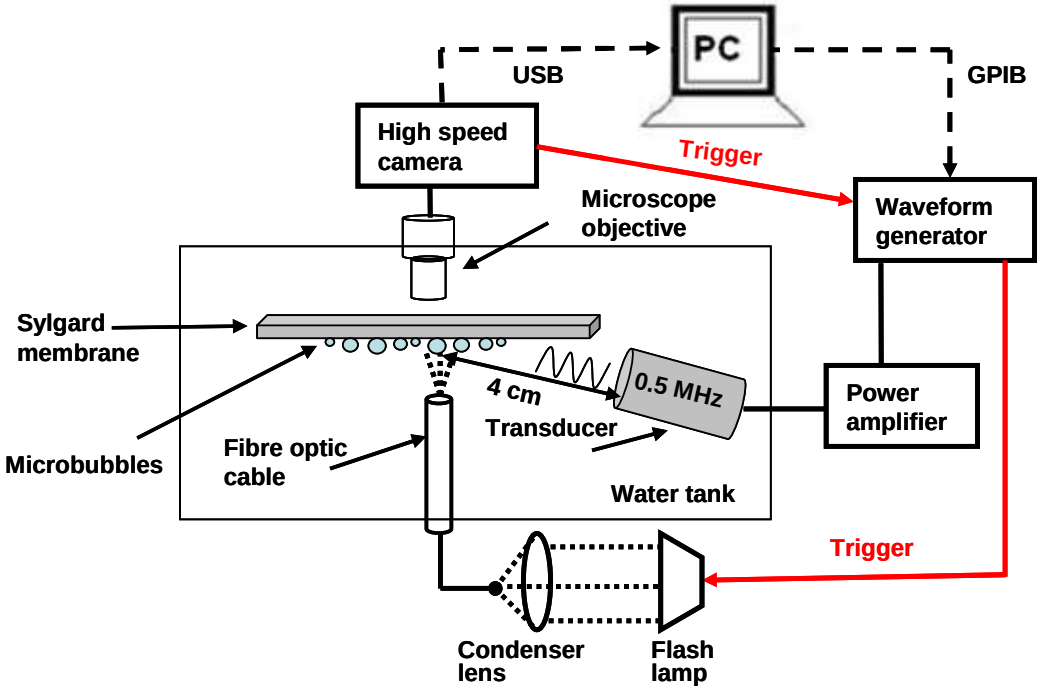

Figure 6-4: High speed camera setup for the imaging of a single oscillating microbubble floating up against a membrane.

Dilute suspensions of experimental phospholipid microbubbles [129] (20µL in 2mL saline) were injected via a syringe underneath a Sylgard membrane which was mounted on a custom-made holder. The membrane was submerged in a water bath containing saline. The position of the membrane was adjusted via an xyz stage so that a single bubble was located at the focus of the microscope objective as well as of the ultrasound transducer. To illuminate the microbubble, a 5 kV flash lamp (Cordin 659, Cordin Scientific) was coupled to a condenser lens (Comar Scientific, Reading, UK) which was connected to a fibre optic cable directed at the membrane. All the major components of this setup are represented in Figure 6-5.

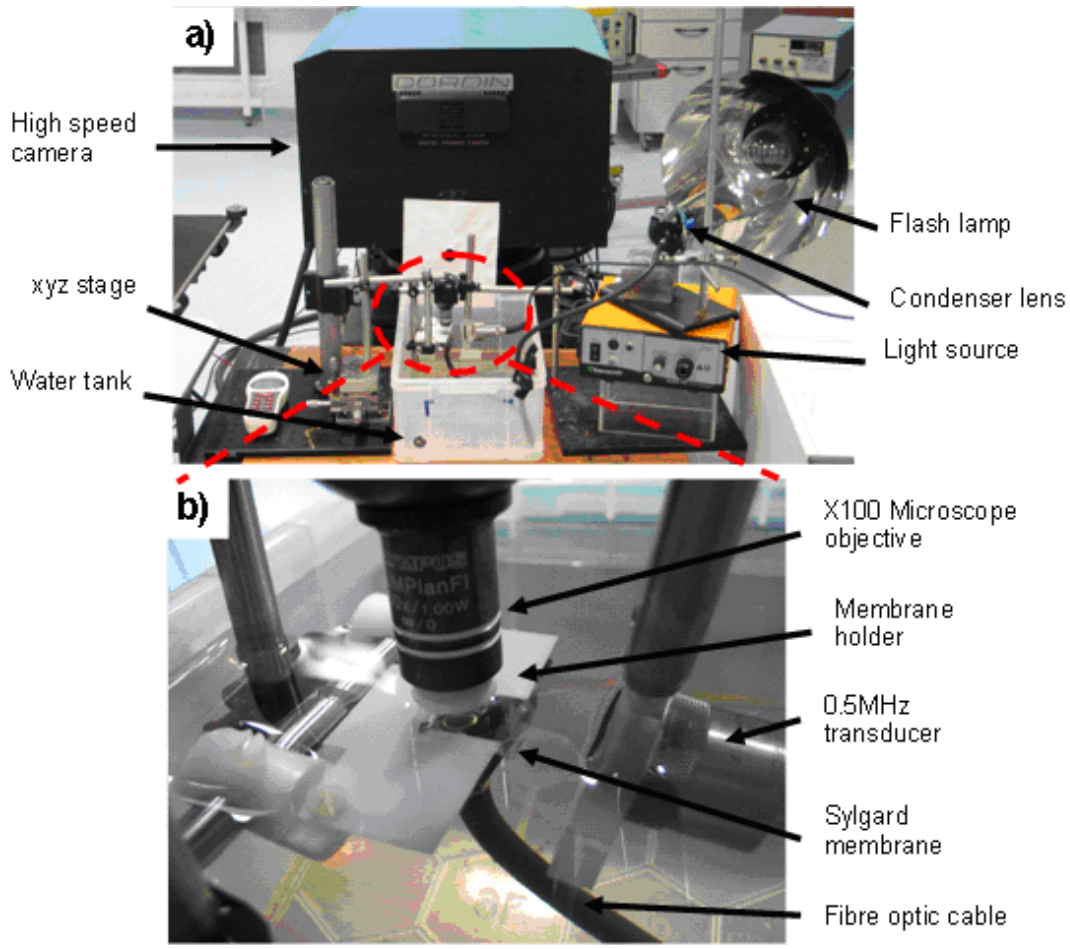

Figure 6-5: High speed camera setup. a) Overall view of the setup and b) zoom on the Sylgard membrane

6.2.4 Optical experiment[4]

Once the microbubbles were injected under the membrane and observing the microbubbles float upwards against the membrane due to buoyancy, one single microbubble was chosen and put into focus of the X100 objective. Care was taken to select an isolated bubble so that the response would not be affected by others. A distance of a few diameters from the nearest bubble neighbours was maintained. Since the interaction between bubbles by secondary Bjerknes forces decays as the inverse square of their distance [43], bubbles could be considered to oscillate independently when separated by a few bubble diameters.

After each recording, the bubbles were removed by flushing the sample with a solution of saline and their disappearance from the field of view was checked. New bubbles

[4] The optical experiment was performed with the help of Dr Robert Eckersley and Dr Helen Mulvana from the Imaging Science Department at Hammersmith Hospital, Imperial College London.
The phospholipid microbubbles were prepared by Dr Charles Sennoga from the department of Bioengineering, Imperial College London.

were then diluted and injected underneath the membrane. This ensured that the response of the next bubble batch could not be affected by a previous insonation as it is known that bubbles can be preconditioned [130], [79]. For each membrane stiffness around 15 bubble recordings were made for a range of diameters varying from 6 µm to 15 µm.

Three identical holders as shown in Figure 6-5 b) were manufactured beforehand on which the membranes were attached with superglue. In order to facilitate the changing of the membranes, the holders could be removed from the water tank and replaced by a new one to which the new membrane was stuck. This allowed the membranes to be used again if needed as well as to prevent them from being altered during the replacement process.

When the rotating sensor of the camera reached the required speed of 2.5 MHz, it initiated the acquisition by triggering both the waveform generator and the flash lamp to synchronize the ultrasonic excitation with the frame recording. To take into account the time between the transmission of ultrasound and the oscillation of the microbubble, a user-defined acquisition is incorporated into the camera control software.

The driving pulse used to excite the single bubble was a 12 cycle Gaussian windowed sine wave, as shown in Figure 6-6. The pulse was chosen to be narrowband in order to drive the bubble with one single frequency and to maximise its response. The peak negative pressure was measured with a needle hydrophone to be 50 kPa, which corresponds to an MI of 0.07. Driving the bubbles in this low acoustic field ensured the bubbles not to get destroyed [85].

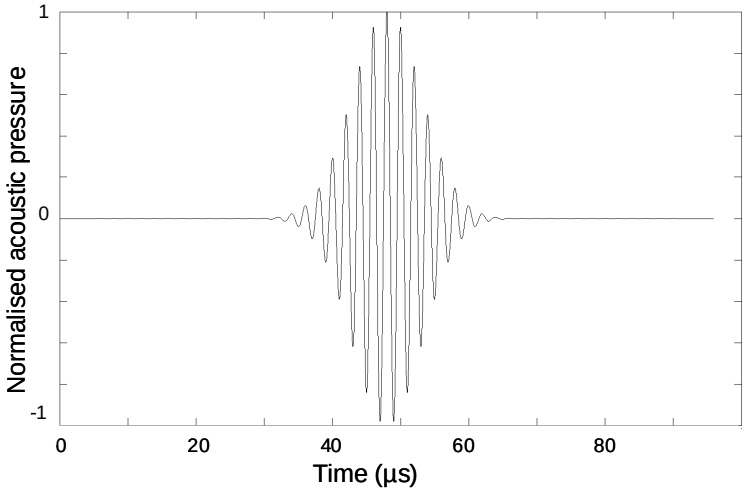

Figure 6-6: Driving pulse used to excite a single microbubble: 0.5 MHz, 12 cycle Gaussian windowed sine wave. The amplitude scale is normalised.

During each insonation, 62 pictures of the selected bubble were taken with the high speed camera and the images were post processed with Matlab™ (The Mathworks Inc., Natick, MA). A program [79] was used to detect the contour of the bubble in each frame in order to measure the variation of the bubble diameter over time due to the excitation pulse. The maximum excursion of the bubble was defined as the difference between the maximum diameter the bubble reaches during its oscillations and its initial diameter at rest. This parameter was used as a way to quantify how much a bubble has been oscillating and therefore how much it would scatter [131].

The results for each of the membranes were presented as graphs showing the maximum excursion as a function of the initial diameter. Information such as resonant frequency and oscillatory amplitude could then extracted for the different stiffness.

The axial and lateral acoustic beams of the 0.5 MHz single element transducer were also measured by placing a 0.1 mm needle hydrophone (Precision Acoustics Ltd, Dorset, UK) at the focus of the probe. The effect on the acoustic field of different types of membrane stiffness and thickness was also studied by measuring the peak to peak voltages with the hydrophone placed behind each of the membranes. The displacement which may be occurring during the change of the membranes was also studied by slightly modifying the membrane position by rotation and translation, and measuring the variations produced on the peak to peak voltage.

6.2.5 Modelling[5]

The experiments were then compared with a numerical model which was used to simulate the forced oscillations of bubbles of different sizes in three situations: for an unconfined bubble, a bubble in contact with an infinitely stiff surface (rigid surface) and in contact with an infinitely soft surface (free surface). The maximal diameter of a bubble in the plane parallel to the surface was calculated to provide a measure equivalent to that in the experiments.

The numerical model was first validated in the case of an unconfined bubble by comparing its bubble response against the solution of the Rayleigh-Plesset equation. The model was implemented using the finite element method package COMSOL MULTIPHYSICS 3.4 (COMSOLAB, Pala Alto, CA).

[5] This simulation work was performed by Dr Sergey Martynov from the Ultrasonics Group at University College London

The ultrasound driving pulse was approximated by a Gaussian windowed sinusoidal pulse of centre frequency f_0 and acoustic driving pressure p_{ac} as expressed in Equation 6.3.

$$p(t) = p_{ac} \sin(2\pi f_0 t) e^{-(0.286 f_0 t - 2.14)^2} \qquad \text{Equation 6.3}$$

Forced oscillations of a bubble with 6 μm equilibrium radius subject to the ultrasound pulse described by Equation 6.3 at p_{ac} = 10 kPa and f_0 = 0.5 MHz were calculated using the finite-volume model in COMSOL, and compared with the solution of the Rayleigh-Plesset equation using the Runge-Kutta method in Matlab. The two curves (curves shown in [121]) representing the variations of the bubble radius are indistinguishable. This was taken to confirm the validity of the computational model for the bubble dynamics built in COMSOL.

For the relatively large bubbles considered in the present study, the phospholipid coating is expected to have only a small effect on the natural frequency of the bubble oscillations [132]. Therefore the bubble natural frequency f_r can be estimated using an equation for uncoated bubbles [133]:

$$f_r = \frac{1}{2\pi} \sqrt{\frac{3\kappa(p_0 + 2\sigma/R_0)}{\rho R_0^2} - \frac{2\sigma}{\rho R_0^3}} \qquad \text{Equation 6.4}$$

where R_0 is the initial radius of the bubble, σ the surface tension, κ the polytropic exponent, p_0 the initial pressure in the liquid and ρ the density of the liquid.
The effect of confinement on the natural oscillation frequency f_r can be estimated using the approach developed by Strasberg [134]. He showed that a bubble oscillating near a boundary is equivalent to two oscillating neighbouring bubbles. He predicted the effect of a rigid wall or a free surface on the resonant frequency of an unconfined bubble described by Equation 6.5:

$$f_S = \frac{f_r}{\sqrt{1 \pm R_0/2d - (R_0/2d)^4}} \qquad \text{Equation 6.5}$$

where d corresponds to the distance from the centre of the bubble to the boundary. For a bubble in contact with the wall, d corresponds to the bubble radius R_0. The plus sign is used for a bubble oscillating in phase, corresponding to the case of a rigid surface. Inversely, the minus sign is used in the case of a bubble oscillating in antiphase, corresponding to the case of a free surface [134].

6.3 Results

6.3.1 High speed camera graphs plots

Extracts from typical series of images taken during a single bubble oscillation are represented in Figure 6-7 a). These images show snapshots of a microbubble during its expansion (at times t_2 and t_4) and compression (at times t_3 and t_5). The microbubble at rest is shown at time t_1 and after its oscillations at time t_6. The first and the last images show that the microbubble has not changed in size after its insonation. This indicates that the applied acoustic field was low enough to not alter the bubbles. The corresponding radial excursion graph to these images over time is shown in Figure 6-7 g).

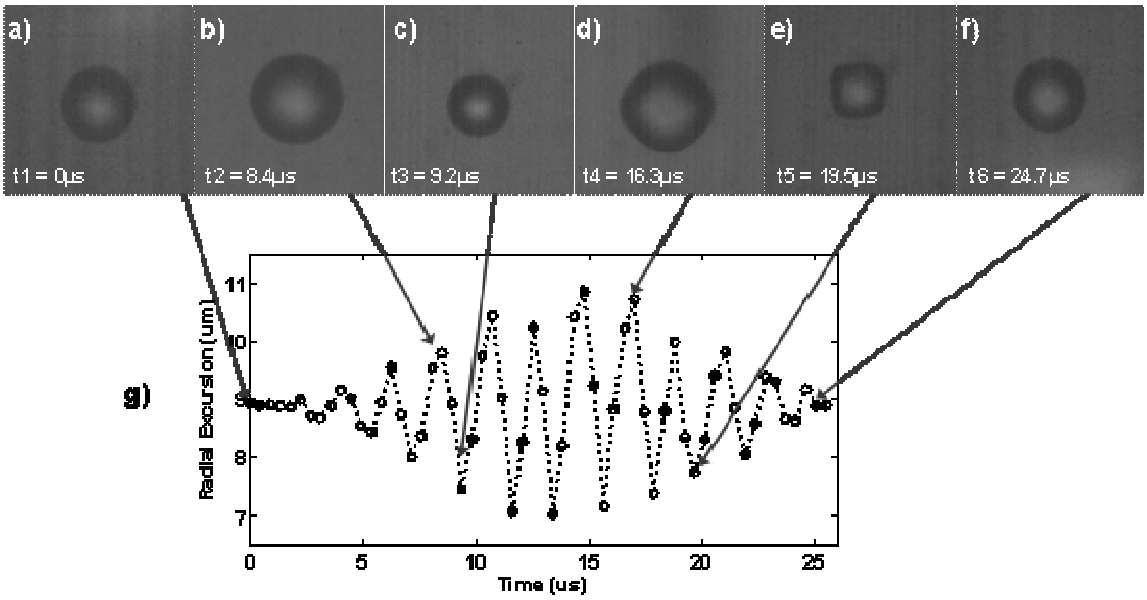

Figure 6-7: Radial excursion observation of a single microbubble of initial diameter 9 µm, placed underneath a membrane of stiffness 517 kPa. A series of six pictures taken at different times, corresponding to compressions (pictures c) and e)) or expansions (pictures b) and d)) are represented. The graph in g) represents the corresponding radial excursion of the bubble as a function of time. The maximum excursion of the microbubble is of 1.9 µm in this case.

All the single microbubble recordings allowed plotting the maximum excursions as a function of the initial diameter of the bubbles. The results for the three different membranes tested are shown in Figure 6-8. Each point was issued from a single bubble recording.

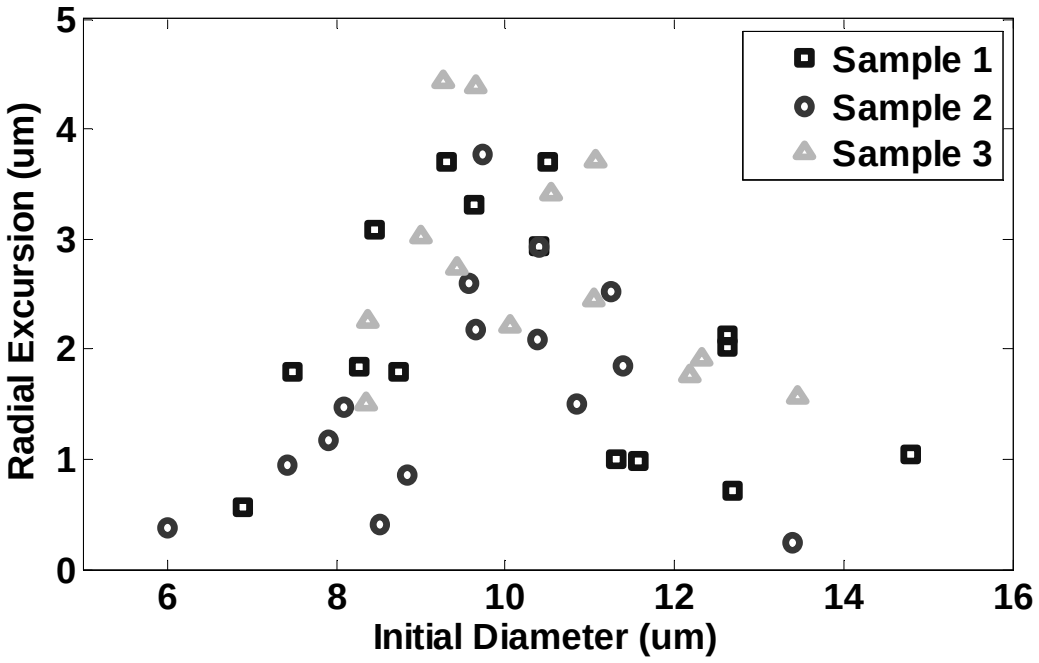

Figure 6-8: High speed camera recording of a single bubble maximal excursion as a function of its initial diameter for bubbles placed under membranes of different stiffness.

For the three different membrane samples, Figure 6-8 showed the bubbles had similar maximum excursions during acoustic insonation, with a peak centred on 10 µm, corresponding to their resonant size at 0.5 MHz.

The acoustic field of the 0.5 MHz transducer was characterised around the focus of the probe, by measuring the axial and lateral beams, as shown in Figure 6-9. As calculated from Figure 6-9 a) and b), the field variation over 3 mm along the axial direction at the focus is less than 1 % and the variation along the lateral beam is around 1.75 %.

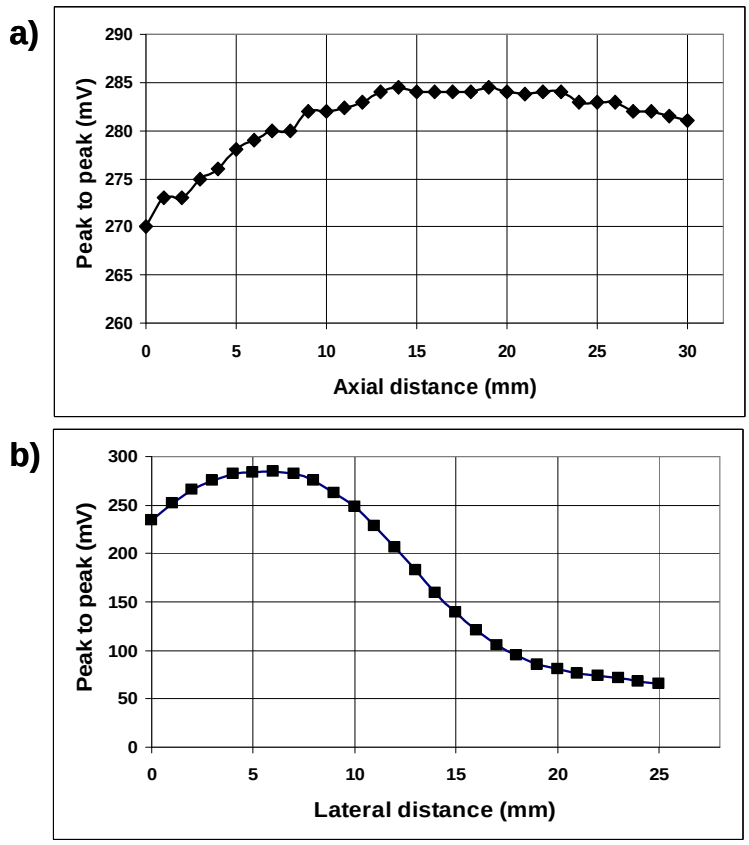

Figure 6-9: Beam profiles measured around the focal point of the 0.5 MHz single element transducer. a) Axial profile (focal point located at around 15mm) and b) lateral profile (focal point located at 5mm). The FWHM corresponds to 2 cm.

Although being cut into identical squares, the membrane samples had a different thickness which could affect the acoustic pressure perceived by the bubbles. The peak to peak voltage measured did not vary more than 1.5% for the three membranes and when their position was slightly modified.

6.3.2 Modelling results

For an unconfined bubble, the maximal calculated expansion as a function of equilibrium diameter is represented in Figure 6-10. The resonant diameter at 0.5 MHz driving frequency is located around 10 µm. It can be noted that the resonant frequency of the bubble decreases with increasing pressure, an observation which has been described by [135]. The second harmonic resonance can be observed for diameters around 6 µm.

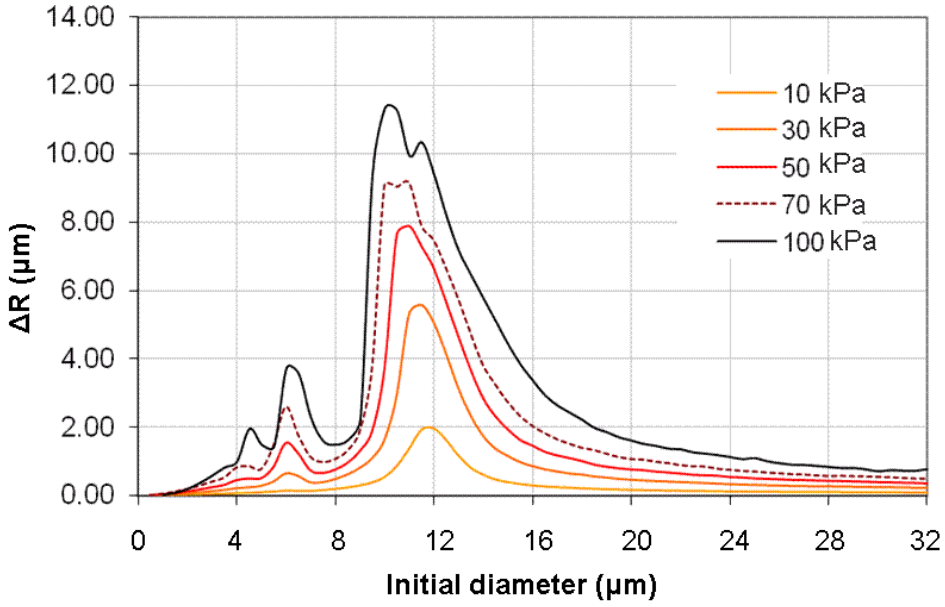

Figure 6-10: The maximal radial expansion of a bubble as a function of the equilibrium diameter, predicted using the Rayleigh-Plesset equation for the excitation pulse described by Equation 6.3Equation 6.3 at f_0 = 0.5 MHz and acoustic pressures p_{ac} = 10, 30, 50, 70 and 100 kPa.

For a confined bubble in contact with a rigid wall, Equation 6.4 and Equation 6.5 predict the resonant diameters at 0.5 MHz to be of 10 μm, which is lower than for an unconfined bubble. This resonant diameter of 10 μm corresponds to the same result observed with the high speed camera for a bubble floating against a membrane. When in contact with a free surface, the resonant diameter is predicted to be 15 μm, which is higher than for the unconfined bubble. This result is represented in Figure 6-11, where the natural resonance frequencies for an unconfined bubble, a bubble at a rigid boundary and at a free boundary are plotted as a function of initial diameter.

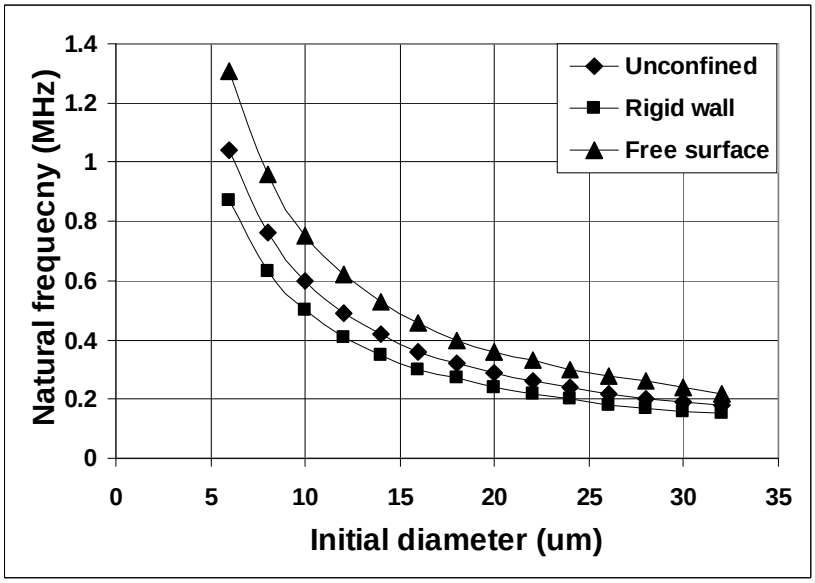

Figure 6-11: The natural frequencies of oscillations of a bubble for an unconfined bubble and for confined bubbles sitting at rigid and free surfaces.

As predicted by Equation 6.5, the resonance frequency of the bubbles decreases with increasing bubble initial diameter. Due to this effect, the maximum excursion observed in Figure 6-10 decreases from 12 μm in diameter onwards since the bubble becomes off-resonance.

For a diameter of 10 μm, the amplitudes of the oscillations of an unconfined bubble are expected to be lower than for a confined bubble near a rigid wall. This can be explained by the fact that the driving frequency f_0 = 0.5 MHz matches closely the resonant frequency of this confined bubble, while for an unconfined bubble the resonant frequency is around 0.6 MHz, i.e. higher than the driving frequency. For a free surface the resonant frequency is around 0.75 MHz, significantly higher than the driving frequency. It is also expecting to have lower oscillation amplitudes than for the confined bubble near a rigid wall.

The resonant diameter of a confined bubble in contact with a rigid wall obtained through the simulations is the same as the resonant diameter observed in the experiments for the different wall stiffness at 0.5 MHz.

6.4 Discussion and future work

6.4.1 Discussion

This work aimed at studying the effect of vessel wall stiffness on the response of a bubble in contact with this wall, through experiments and simulations.

The experimental results shown in Figure 6-8 do not indicate any clear difference in the resonant diameter or in the maximum radial excursion for the different membrane stiffness tested. This observed resonant diameter corresponds to the resonant diameter obtained through the simulations of a confined bubble in contact with a rigid wall, shown in Figure 6-11. A certain number of factors could explain these results.

The stiffness for which the bubble would show any difference was unknown at the start of the optical experiments. The Young's modulus and the membrane thicknesses were chosen to be in the range of typical human vessel walls [116], [127] and the stiffness tested in this study may not have had a noticeable effect on the bubble oscillation. The numerical results showed that for a bubble at a rigid surface the resonant diameter at 0.5 MHz was of 10 μm, which also corresponds to the resonant diameter found in the experiments. For a bubble near a free surface, the resonance is expected for a diameter of 7.5 μm. The numerical model placed itself in the two extreme vessel stiffness cases, and it is possible that the membrane stiffness tested in the experiments can be approximated by rigid walls.

The variation of the radial excursion amplitude for a particular initial diameter was found to be ± 0.5 μm, as shown in Figure 6-8. Errors such as the sensitivity of the CCDs, the optical alignment in the acquisition system and the uncertainties in the magnification calibration estimation were measured in [136] to lead to a combined error of ± 0.1 μm on the measured bubble diameter. Other sources of error include the bubble diameter estimation via the image processing programme described in [79], which detects the contour of the bubble. The change in bubble size during its oscillation can lead to the bubble being slightly out of focus, leading to blurred microbubble edges and causing an error in the measured diameters.

Uncertainties regarding the acoustic pressure perceived by the bubbles can also contribute to the total error. By replacing one membrane holder by another, slight changes of the acoustic field may occur. Some of these effects were quantified by measuring the beam widths at the focus of the single element transducer. The 1% and

1.75% peak to peak voltage variation measured at the focus over 3 mm, for the axial and lateral beams respectively, should not significantly vary the pressure perceived by the bubbles.

The optical recording frame rate also plays an important role in the accuracy of the measurements. In these experiments a frame rate of 2.5 MHz was used to observe microbubbles driven at 0.5 MHz. The limited frame rate can therefore induce errors in the measured maximum excursion during the bubble oscillation.

As described by Chetty [136], the camera was not operated at its maximum possible frame rate (4 MHz) due to the insufficient sensitivity of the CCDs. Improving the intensity of the incoming light could allow using an increased imaging rate. When working at 0.5 MHz, below the typical clinical frequencies, the resonant bubble diameters are correspondingly larger. The use of an apparatus such as Brandaris 128 camera [137], would allow higher sampling rates enabling to drive the bubbles at more clinically used frequencies as well as the detection of harmonics.

Care was taken to keep the bubbles highly concentrated in a vial during the entire experiment in order to enhance their lifetime and new dilutions were prepared before each bubble recording. However it is possible that the bubbles may have deteriorated over the time as the total time per membrane sample was of around two hours. A change in bubble concentration over time [105] could include a change in the stability and therefore induce differences in the scattering.

6.4.2 Future work suggestions

The choice of performing an optical experiment over an acoustic experiment had both advantages and inconveniences. The optical setup enabled the recording of the response of a single bubble only. By keeping a distance of a few bubble diameters with neighbouring bubbles, the secondary Bkerkness forces could be neglected and the bubble was considered to oscillate independently [43]. This is not the case in an acoustic experiment, imaging a cloud of bubbles of a certain size distribution. Such experiment, commonly performed on a pulse-echo acquisition bench would also enable information such as scattering and higher harmonic scattering. However, relating the results to any behaviour properties of the bubbles themselves could have proven to be difficult.

A complementary experiment would be to measure the acoustical scattering responses of single microbubbles placed underneath the membranes. One challenging step would

be the isolation of a single microbubble in order to acquire its response. This could be done as developed by Thomas *et al.* [138] by highly diluting a microbubble population, enabling the RF backscatter of individual microbubbles. However such setup did not enable the measurement of the initial bubble diameter and the results were related to the microbubble population. An optical system coupled to the acoustic system would allow the verification of the presence of an isolated bubble as well as the measurement of its initial diameter. Relations such as the amount of scattering and resonant diameter as a function of rest diameter could therefore be obtained. Such a setup would highly increase the number of recordings as well as the flexibility over the type of driving pulses used, due to the high sampling rate and short acquisition time required.

Complementary studies to this one could also include imaging the microbubble oscillations in the plane normal to the membrane. Indeed, previous studies have shown bubbles to behave asymmetrically when adherent [71] or in contact [36] with the wall.

The high speed camera study presented here could also lead to future work studying the behaviour of targeted microbubbles versus microbubbles in close proximity to but not stuck a wall. Indeed, one of the main challenges in molecular imaging is the discrimination of targeted bubbles from freely flowing ones. Especially at very slow velocities near the wall, current signal processing methods cannot properly distinguish between slowly moving bubbles and adherent bubbles [33]. The acoustic difference between targeted bubbles and bubbles in contact with a wall is not yet fully understood and could lead to improved methods to perform this discrimination.

6.5 Conclusion

The work in this chapter was aimed at studying the effect of vessel wall stiffness on the response of a microbubble in contact with this wall. Fields of application include the early detection of atherosclerosis, the assessment of artery calcification over time as well as a better understanding of the bubble-wall interactions for the development of selective targeted microbubble detection methods.

A large vessel was modelled by a flat membrane, whose stiffness could be controlled. The Young's moduli and thicknesses were chosen within the stiffness range of human blood vessels. High speed camera experiments were conducted to assess the influence of the stiffness on the dynamic behaviour of single microbubbles excited by an acoustic pulse. The maximum radial excursions were plotted as a function of initial bubble diameter for the three membranes. The experiments were then compared with

a numerical model simulating the forced oscillations of bubbles of different sizes in three cases: in contact with a rigid wall, with a free surface and when unconfined.

The experimental results showed the bubbles having similar maximum excursions and resonant diameters for the three membranes. The observed resonant diameter corresponded to the one obtained through the simulations for a confined bubble in contact with a rigid wall. These results showed a negligible influence of the membrane stiffness tested within the human stiffness range on the acoustical behaviour of microbubbles. Suggestions of future work include the observation of the bubble oscillations in the normal plane as well as single microbubble acoustics.

Chapter 7 Conclusions and achievements

7.1 Overview

The medical use of ultrasound targeted contrast agents presents many challenges, starting with the design of microbubbles of high specificity and efficiency, capable of binding to molecular markers expressing diseases. Once injected in the blood stream, the density of bound bubbles as well as their binding need to be high enough in order to be detectable.

One key challenge is the acoustic detection of the bound agents and in particular their differentiation from unbound agents and tissue. This thesis studied the imaging of targeted contrast agents in order to develop principles and methods for their discrimination. While many custom designed techniques to solve this issue are based on the succession of different steps such as 1) a slow time filter which rejects moving agents, 2) a nonlinear contrast agent modality which allows tissue signal cancellation, and 3) image post processing, no technique has been developed which makes use simultaneously (in the same operation) of the movement information and the nonlinear behaviour of the contrast agents. Although originally not designed for this purpose, such a technique was developed by Simpson *et al.* [50], named as pulse inversion Doppler (PID). One of the main questions of this thesis was to understand how PID could answer the problem of selectively imaging targeted ultrasound contrast agents. The study of this question lead to the conclusion that PID could be appropriate under certain conditions, but also that other excitation patterns could present the same interesting behaviour while offering other benefits. As such, the first technique developed in this thesis was pulse subtraction Doppler (PSD), based on a combination of pulse subtraction time delay imaging [56] and Doppler. However, the results obtained with PSD could not be fully explained by the theory developed by Simpson *et al.* [50]. It was hypothesised that the pulse sequences which were required to obtain typical dual band nonlinear Doppler spectra were not limited to a given shape. A generalised nonlinear Doppler framework was developed and was shown to enable the design of pulse sequences taking into consideration the specific clinical application and the hardware limitations for an improved sensitivity to contrast agents. The first steps towards the detection of targeted contrast agents were then undertaken by testing PSD on several *in vitro* flow phantoms.

A better understanding of the behaviour of targeted bubbles when bound to a vessel wall could enable the design of specific imaging sequences for their detection and discrimination from free flowing ones. The second approach taken in this thesis considered the influence of a membrane of varying elasticity on the behaviour of bubbles in its vicinity.

The following sections aim at summarising and discussing the main findings of this thesis as well as exploring future work directions. Possible research directions in the area of ultrasound molecular imaging are also presented. Finally, the principal achievements of the thesis are summarised.

7.2 Pulse subtraction Doppler

A novel nonlinear Doppler technique, pulse subtraction Doppler (PSD) was developed (chapter 3), based on the combination of pulse subtraction imaging [56] and ultrasound Doppler imaging. The technique was designed to exploit the fact that adherent bubbles are stationary and nonlinear scatterers.

This technique was shown, in both simulation and *in vitro* experiments, to enable the extraction of velocity information as well as the separation of nonlinear from linear scattering, as they appear in different frequency bands of the Doppler spectrum. A comparison of PSD with pulse inversion Doppler (PID) has shown the contrast to tissue ratio (CTR) in PSD to be on average 3.3 (± 0.4) times higher than PID at a mechanical index (MI) of 0.1 and when demodulating the RF echoes, as for conventional Doppler, at the fundamental frequency. When demodulating at the second harmonic frequency, PID was shown to have a 3.1 (± 0.4) times higher CTR than PSD. Overall, taken in their optimum processing conditions, PID had a CTR up to 1.9 (± 0.4) times higher than PSD.

The study highlighted that the detection of nonlinear signal was dependent on the transducer bandwidth characteristics. The detection of the nonlinear fundamental was not optimal for PSD as the receive transducer bandwidth was not centred on the fundamental frequency f_0 of the echo. Transmitting the pulses using a transducer centred at f_0 would improve the pulse transmit efficiency and receive sensitivity of the nonlinear fundamental signal. Depending on the ability of the transducer to detect second harmonics, PSD could prove itself as a useful alternative in the detection of nonlinear signal.

In addition, the PSD and PID pulses were compared on the basis of equal resolution and the actual energy transmitted into the medium was 25% less in PSD than in PID. The design of the PSD driving pulses has the drawback of cancelling the initial part of the nonlinear bubble response signal. This characteristic reduces the amount of useful microbubble signal which contributes to the nonlinear signal. Combining other nonlinear techniques with PSD could tackle this problem.

PSD was also shown to be straightforward to implement on a Sonix RP 500 (Ultrasonix Medical Corporation, BC, Canada) research scanner and provides an alternative approach on scanners which suffer from the inability to produce perfectly inverted or amplitude scaled pulses. This is as it does not require phase inversion or amplitude modulation.

In the framework of distinguishing targeted microbubbles from free-flowing ones, one major limitation with nonlinear Doppler is the difficulty of distinguishing slow flowing microbubbles near the vessel wall from stationary targeted microbubbles. Future *in vitro* and *in vivo* studies should try to exploit the properties of the nonlinear Doppler techniques in order to isolate signals arising from targeted microbubbles. Complementary work should include single bubble experiments providing a way of comparison with the simulation results.

7.3 Generalised contrast imaging and nonlinear Doppler

The development of PSD and its comparison study to PID imaging served as a starting point for the derivation of a generalised nonlinear Doppler technique (chapter 4). This technique was based on the construction of combined linear pulse pair sequences of varying parameters such as phase, amplitude and pulse length. Simulation studies showed that this technique enables, as for PSD and PID, the discrimination in the Doppler spectrum of linear and nonlinear scattering. The response from a single microbubble was simulated for different pulse combinations and their efficiency was compared with regards to criteria specific to technical and medical ultrasound imaging requirements. This work demonstrated that, for a well-characterised ultrasound system and a specific clinical application, an appropriate choice of the contrast specific pulse sequence could improve the sensitivity. This work also showed that there is no ideal nonlinear sequence to be used by all scanners, but rather that a dedicated pulse pair should be designed and optimised depending on the technical limitations and the specific clinical application.

White Gaussian noise was also added to the echoes and contrast to noise ratios for the different sequences were calculated. Pulses which required most operations in the construction of the virtual echo had the greatest noise level in the calculated nonlinear signal. This study showed that a trade-off must be found between the sophistication of the pulse pair and its final efficiency.

The nonlinear Doppler study highlighted an aspect also present in the comparison study between PSD and PID imaging. Depending on the transducer bandwidth, certain pulse combinations are more adapted and offer a better contrast. For example pulse inversion (PI) achieved its highest contrast level at the second harmonic. At the nonlinear fundamental however, a combination of pulse inversion, amplitude modulation and pulse subtraction (PIAMPS) was found to provide the highest contrast. Enhancing the nonlinear fundamental can be particularly useful for bandwidth limited transducers which do not detect second harmonics. Making use of the nonlinear fundamental has also the advantage of improving the sensitivity and tissue penetration since it is less attenuated than higher harmonics [55].

Comparing pulse sequences in a fair way was shown to be a challenging task since the pulses had different characteristics such as energy, peak negative pressure or pulse length. The pulse sequences were therefore also compared by normalising the obtained contrast by criteria defined with regards to standard clinical applications. PIAMPS imaging for example was shown to enable a higher contrast to transmitted energy ratio than PI and should be favoured if the transmitted energy needs be kept to a minimum. Especially for imaging modes such as Doppler imaging, where the pulse repetition rates can be high and the imaging time longer, it may be important to choose an appropriate pulse sequence to obtain a good contrast without transmitting too much energy into the tissue.

This study was based on the simulation of one single microbubble. In order to be closer to an *in vivo* situation, the nonlinear response of a bubble population would need to be simulated. The concentration and size distribution of bubbles, depth of imaging may play a role in the contrast to noise ratio. Future *in vitro* work should focus on assessing experimentally the relative performances of the pulse sequences on a solution of contrast agents and compare the results to simulations.

The effects of tissue attenuation and nonlinear propagation through tissues and bubble clouds were not considered in these simulations and would also play an important role in estimating the contrast to tissue ratio. Attenuation increases with frequency and

makes the imaging of higher order harmonics more difficult. Deep tissue imaging for example is usually limited by attenuation [82]. The use of a higher MI increases penetration, but would also increase nonlinear propagation [83], [84] which in turn contributes to reducing the CTR. Since tissues can also produce harmonics, these will mix with the ones produced by the microbubbles and cannot be removed [85].

Nonlinear propagation in a tissue medium could be simulated by solving the Khokhlov–Zabolotskaya–Kuznetsov (KZK) equation to calculate the CTR [98], as it was done by Borsboom *et al.* during the study of pulse subtraction time delay imaging [56]. In their paper, CTRs were calculated when a bubble was excited by the driving pulses after they had been propagating in the nonlinear medium. Future studies should incorporate the effect on echo recombination of tissue nonlinearities.

Although the pulse combinations proposed in Equation 4.4 are unlimited, the study was restricted to a limited number of pulse parameters: two amplitudes, two pulse lengths and two phases where chosen in order to simplify the computation. However more advanced studies could be considered by increasing the range of each parameter. Other contrast modes such as radial modulation imaging [139], coded excitations [99], [100], subharmonic imaging [140] or sequences based on the transmission of more than two pulses were not considered in this study. Their combination with nonlinear Doppler modalities could potentially enhance the contrast to tissue ratio. Optimising the CTR by varying the transmission pulse parameters as a function of initially set imaging conditions and equipment constraints would be a future way of choosing the most appropriate pulse for the desired application.

In this study the pulse parameters chosen had a limited risk factor for the patient and for the microbubble destruction, by keeping the driving pressures low. However in a general approach consisting of testing many complex sequences of varying amplitudes, the safety criteria become important.

Future work should also include the determination of pulse sequences maximising the response of targeted bubbles and allowing their distinction from free flowing ones. Such specific pulse developments also rely on the improved understanding of the acoustic properties of agents bound to a surface.

7.4 Towards the detection of targeted bubbles with nonlinear Doppler

Two *in vitro* flow phantoms were designed for testing nonlinear Doppler as a potential tool for discriminating targeted microbubbles from free flowing ones and tissue. Preliminary work was also performed on in-house made targeted bubbles.

7.4.1 Imaging of static microbubbles

The first flow phantom consisted of linear scattering tubing, static microbubbles at the tube walls and flowing bubbles. Pulse subtraction Doppler was shown to detect the static microbubbles and to reject both the flowing bubbles and the linear scattering tubing. Different types of information could be displayed at the same time: static and nonlinear Doppler scattering was overlaid on standard colour Doppler images.

The phantom model chosen to test the technique was a starting point for future targeted microbubble phantoms. In the real context of a blood vessel, the targeted microbubbles would be bound to the endothelial cells of the vessel wall through ligands and the density of bound bubbles may be far less than in this experiment, leading to a weaker signal from the bubbles. The characteristic response of bubbles adjacent to a wall was also shown to differ from the free bubbles in frequency and amplitude [72]. The response signal from the bubbles in between the two tubes of our approach-phantom may therefore be different from the true targeted bubbles. However since the discrimination process in this study was strictly based on the static and nonlinear properties of the still agents, the technique should not be affected by these acoustic differences.

One main limitation of the technique is the separation between slowly moving scatterers near the vessel wall and static stuck microbubbles. The ability to separate slow motion from no motion is limited by the frequency resolution, depending on the length of the observation interval. Increasing the observation time by increasing the number of recorded Doppler samples would improve the frequency resolution and reduce the overlap of slowly moving scatterers; however this would also reduce the frame rate. This limitation is a common issue for the current techniques, which use averaging over multiple pulses in order to suppress the decorrelation between the frames, such as in [29] and [31].

Another common issue of the current targeted detection techniques [29] are their efficiency under conditions of tissue motion. Areas of further work with nonlinear

Doppler should include testing the technique under such conditions and determine its efficiency.

7.4.2 Imaging of magnetic microbubbles

In this study, magnetic microbubbles were characterised by observing their behaviour in a magnetic field by microscopy, and by recording ultrasound video with the bubbles in flow conditions. Microscopy images of the displacement of the bubbles under the action of a magnet showed them to move towards it at different speeds, suggesting possible different magnetisation levels or chemical composition of the bubbles. It was also shown that the magnetic bubbles could be immobilised to a specific region of interest under flow conditions by a magnetic field. The pulse subtraction Doppler sequences were tested on free and immobilised bubbles at the wall. The immobilised bubbles were shown to be acoustically detectable by an enhancement in signal intensity at the wall. Applying PSD sequences to immobilised and free microbubbles has shown the bubbles to scatter linearly in both cases for the driving pressures used. PSD was therefore not a suitable technique for distinguishing the immobilised bubbles from the flowing ones since they were not detectable in the nonlinear band of the Doppler spectrum. Future work should address this issue and could aim at varying the chemical composition of the microbubbles in order to increase their nonlinearity. Stride *et al.* [110] have suggested modelling approaches of these bubbles in order to better understand their behaviour with regards to their chemical composition.

The video recordings showed that some bubbles did not immobilise at the wall. This may be explained by the different forces acting on them. Depending on the chemical properties (e.g. the amount of magnetic particles contained in its shell or shell material), physical properties (e.g. its size or shell thickness) of the bubbles and depending on the ultrasound and magnetic field characteristics, all the bubbles will experience different forces and therefore have different trajectories. Further work could use single bubble acoustics or high speed camera recordings to measure the possible differences in oscillation of bubbles of different magnetisations. Future *in vivo* work would also require a better understanding of the magnetic bubble acoustical behaviour and their immobilisation under different flow rates. Knowledge of the magnet strength required and its positioning with regards to the desired focus seem to constitute important preliminary steps. Finally, the acoustic parameters such as driving pressure, frequency and exposure time should be optimised.

7.4.3 Preliminary work on biotinylated microbubbles

Some preliminary work was performed with in-house developed targeted microbubbles. The detailed methodology for attaching biotinylated microbubbles to a streptavidin coated surface was described and tested to attach bubbles to different types of surfaces. The bubbles were shown through microscopy images to attach to a petri dish, agar, gelatine and sylgard, however not to latex.

An immediate outcome of this work would require the testing of nonlinear Doppler pulse sequences on flow phantoms containing targeted microbubbles in the presence of flowing ones and tissue. The information on the binding of biotinylated bubbles to different types of streptavidin coated surfaces is useful knowledge for the good choice of vessel mimicking material for the design of such flow phantoms as constructed by [31], [32]. The effect of wall shear stress on the binding strength of the agents [113], [141] as well as their binding density to the surface [101] are important factors to be taken into consideration during the design. In this thesis, the bubbles were bound to streptavidin coated surfaces by floatation. The method used for their attachment under flow conditions therefore also needs to be addressed. Radiation force has been shown a useful tool for an increased bubble adherence by pushing them to the walls [26] and should be considered for the design.

7.5 Oscillations of microbubbles in contact with an elastic wall

A better understanding of bubble-wall interactions could enable the design of specific imaging sequences for the detection and discrimination of targeted contrast agents from free flowing ones. A second approach taken in this thesis considered the influence of a membrane of varying elasticity on the behaviour of bubbles in its vicinity. A large vessel was modelled by a flat membrane, whose stiffness could be controlled. The Young's moduli and thickness were chosen within the stiffness range of human blood vessels. High speed camera experiments were conducted to measure the maximum radial excursions as a function of initial bubble diameter for three membranes of different stiffness. The experiments were compared with a numerical model simulating the forced oscillations of bubbles of different sizes in three cases: for an unconfined bubble, a bubble in contact with an infinitely stiff surface (rigid surface) and in contact with an infinitely soft surface (free surface).

The experimental results showed the bubbles having similar maximum radial excursions and resonant diameters for the three membranes. The observed resonant

diameter at 0.5 MHz driving pulse frequency was of 10 µm, corresponding to the one obtained through the simulations for a confined bubble in contact with a rigid wall. The results suggest that the influence of the membrane stiffness within the human stiffness range is negligible on the acoustical behaviour of microbubbles.

Several sources of error were described, which lead to a combined error of around ± 0.5 µm on the measurement of the bubble diameter. Errors were listed such as the sensitivity of the CCDs, the image processing programme estimating the bubble diameter, the change in the bubble size during its oscillation which can lead to the blurred edges and the optical recording frame rate.

Due to the limited camera frame rate, the size distribution of the excited bubbles had to be increased accordingly in order to work with resonant sized bubbles. These were much larger than the common resonant bubbles typically used in clinical examinations.

Future complementary experiments could include single bubble acoustics, measuring the responses of single microbubbles placed underneath the membranes, which can typically be done with a pulse echo system. Such experiment would allow acquisitions at higher sampling rates and therefore more flexibility over the type of driving pulses at clinical driving frequencies. Challenging steps in this setup would be the acoustic isolation of a single microbubble. For optical recordings a distance of a few microbubble diameters was enough to consider the bubble to oscillate independently from its neighbours [43]. However for an acoustic acquisition, it is important to be able to record to response of a single bubble only. Thomas *et al.* [123] proposed generating a jet of solution containing a highly diluted microbubble population, allowing the measurement of backscatter from individual microbubbles. However such a setup does not enable the measurement of the initial bubble diameter and the results were related to the microbubble population. Coupling an optical system to the acoustic system would allow the verification of the presence of an isolated bubble as well as the measurement of its initial diameter. Relations such as the amount of scattering and resonant diameter as a function of rest diameter could therefore be obtained. Such a setup would also highly increase the number of recordings due to the short acquisition time required. Future experiments could also include imaging the microbubble oscillations in the plane normal to the membrane as they were shown to behave more asymmetrically [71], [36] than in the parallel plane.

In the aim of distinguishing targeted microbubbles from free flowing ones, it is important to improve our understanding of the differences in acoustic signatures between

adherent and free bubbles. Especially at very slow velocities near the wall, current signal processing methods cannot properly distinguish between slowly moving bubbles and stuck bubbles [33]. The acoustic differences between targeted bubbles and bubbles in contact with a wall is not yet fully understood and could lead to improved methods to perform this discrimination.

7.6 Future research directions for ultrasound molecular imaging

Ultrasound has the advantage over other imaging techniques to be low cost, portable and able to achieve high frame rates, as well as to provide potentials for therapy [81]. Furthermore, the application of contrast agents to molecular imaging was shown to be a promising tool for the early detection of cardiovascular diseases and cancer [81]. Some areas of current research in molecular ultrasound imaging are described in this section.

One achievement of this thesis was to show that dedicated pulse pair sequences could be designed and optimised under specific imaging constraints and medical applications in order to enhance the sensitivity of ultrasound to microbubbles. This study was performed on simulated single bubbles. However, in experimental conditions the pulses will act on microbubble distributions which have a broad range of diameters, typically 1 to 10 µm. In molecular imaging, where the density of adherent bubbles is low, it is important to be maximally sensitive to the entire adherent bubble population [142]. The design of novel types of microbubbles could improve their detectability. Talu *et al.* [103] have shown promising results in the manufacturing of monodisperse microbubbles which can produce greater sensitivity than polydisperse contrast agents. Their attachment *in vitro* in a flow chamber has been shown by Schmidt *et al.* [143], however the production rates of such agents is still relatively low compared to polydisperse bubbles [103]. Stride *et al.* [110] have shown that the changing in the coating of microbubbles could also greatly increase the nonlinear response of bubbles. Combining novel types of microbubbles with selective imaging pulses could lead to enhanced contrast from targeted bubbles.

The development of adapted imaging systems which can keep up with the advancement of the imaging sequences required also plays an important role. One common limitation is the bandwidth specification of the systems, usually reducing the ability to detect higher harmonics. The recent development for example of a dual frequency transducer by Zheng *et al.* [144] has shown to achieve both radiation force

pulses for pushing the bubbles to the walls to increase their attachment, as well as imaging the adhered agents. Targeted microbubbles have also been observed using high frame rate ultrafast imaging [145], capturing around 500 frames per second. Such imaging systems have enabled the tracking of the gas contained in targeted microbubbles just after their disruption. As they expect the dissolution of the gas from targeted bubbles to be different from free bubbles, this imaging may help developing techniques for the discrimination of bound from free-flowing agents.

Molecular imaging has not only the potential for early disease detection but can also be a tool for treatment and monitoring of diseases. Under ultrasound action microbubbles have shown to be therapeutic tools which can facilitate gene transfection [146] [147]. The design of novel magnetically active bubbles has also been shown *in vitro* to enhance gene transfection under acoustic and magnetic fields [104]. As well as immobilising them to a specific region of interest under flow conditions, the work with magnetic bubbles in chapter 5 showed them to scatterer linearly. Future work on the chemical composition of bubbles through simulation and experimental studies are crucial for the design of optimised bubbles for both therapeutic and targeted applications.

7.7 Principal achievements

- A novel contrast agent detection method PSD was developed which simultaneously enables the separation in the Doppler spectrum of linear and nonlinear scattering as well as the measurement of the scatterer velocities.

- PSD was tested on a flow phantom and was shown to discriminate static nonlinear bubbles from freely flowing ones. Different types of information were displayed at the same time: nonlinear Doppler information was being overlaid on standard colour Doppler images.

- The nonlinear Doppler imaging concept was generalised and it was shown that the combination of linear pulse pair sequences with Doppler could lead to similar dual band spectra. Simpson's PID [50] and the PSD developed in this thesis belong to this family of techniques, which cover standard nonlinear imaging techniques.

- Nonlinear Doppler sequences were created with a given set of parameters and compared with each other. It was demonstrated that there is no ideal nonlinear sequence to be used by all scanners, but rather that a dedicated pulse pair should be designed and optimised depending on the technical limitations and the specific clinical application.

- An in vitro study of novel magnetic bubbles has shown it possible to immobilise them under a magnetic field to a specific region of interest at the vessel wall under flow conditions.

- The magnetic bubbles were shown to be acoustically detectable by an enhancement of the signal at the wall when immobilised. PSD sequence acquisitions of the magnetic bubbles showed them to behave as linear scatterers at the driving pressure used.

- Preliminary work was performed with in-house made targeted microbubbles. The protocol for the attachment of biotinylated microbubbles to streptavidin coated surfaces was tested and the bubbles were shown to attach to different types of surfaces including a petri dish, agar, gelatine and sylgard; however they did not attach to latex surfaces.

- High speed camera images of bubbles close to a membrane of different stiffness showed that the bubbles exhibited similar resonant radii and amplitudes within the range of large human blood vessel stiffness.

- Technical developments:

- A pulse-echo acquisition system was set up, remotely controlling a function generator and an oscilloscope via Matlab^{TM}. A computer designed pulse could be uploaded via GPIB interface onto a pulse generator which then produced electrical impulses to drive a transmitting transducer. The echo signals were then acquired on the receiving transducer, stored on an oscilloscope and transferred to a work station via USB for future post processing.

- Pulse sequences such as pulse subtraction Doppler were implemented onto the Sonix RP 500 research scanner.

- Contributions were made to the development of a robust method for the counting and sizing of microbubble populations. This work was published in [105].

7.8 Final conclusion

This thesis has taken two complementary research approaches to tackle one major problem in molecular imaging with ultrasound. Both approaches have shown to constitute advancements for the detection and discrimination of targeted microbubbles from free flowing ones and tissue. The foundations of a generalised nonlinear Doppler concept constitutes a new imaging method allowing the differentiation of targeted bubbles but also the possible optimal design of adapted imaging pulses for medical imaging requirements. In conjunction with the constant increased knowledge about the acoustic properties of targeted bubbles, new imaging strategies will be developed and allow a cascade of new means of investigation and communication with the vascular system.

References

[1] D. Lloyd-Jones, R. J. Adams, T. M. Brown, M. Carnethon, S. Dai, G. De Simone, T. B. Ferguson, E. Ford, K. Furie, C. Gillespie, A. Go, K. Greenlund, N. Haase, S. Hailpern, P. M. Ho, V. Howard, B. Kissela, S. Kittner, D. Lackland, L. Lisabeth, A. Marelli, M. M. McDermott, J. Meigs, D. Mozaffarian, M. Mussolino, G. Nichol, V. L. Roger, W. Rosamond, R. Sacco, P. Sorlie, R. Stafford, T. Thom, S. Wasserthiel-Smoller, N. D. Wong, J. Wylie-Rosett, and S. Amer Heart Assoc Stat Comm, "Heart Disease and Stroke Statistics-2010 Update A Report From the American Heart Association," *Circulation,* vol. 121, pp. E46-E215, 2010.

[2] J. Leal, R. Luengo-Fernandez, A. Gray, S. Petersen, and M. Rayner, "Economic burden of cardiovascular diseases in the enlarged European Union," *European Heart Journal,* vol. 27, pp. 1610-1619, 2006.

[3] T. Thom, N. Haase, W. Rosamond, V. J. Howard, J. Rumsfeld, T. Manolio, Z. J. Zheng, K. Flegal, C. O'Donnell, S. Kittner, D. Lloyd-Jones, D. C. Goff, Y. L. Hong, R. Adams, G. Friday, K. Furie, P. Gorelick, B. Kissela, J. Marler, J. Meigs, V. Roger, S. Sidney, P. Sorlie, J. Steinberger, S. Wasserthiel-Smoller, M. Wilson, P. Wolf, C. Amer Heart Assoc Stat, and S. Stroke Stat, "Heart disease and stroke statistics - 2006 update - A report from the American Heart Association Statistics Committee and Stroke Statistics Subcommittee," *Circulation,* vol. 113, pp. E85-E151, 2006.

[4] R. P. Choudhury, V. Fuster, and Z. A. Fayad, "Molecular, cellular and functional imaging of atherothrombosis," *Nature Reviews Drug Discovery,* vol. 3, pp. 913-925, 2004.

[5] P. Libby, "Inflammation in atherosclerosis," *Nature,* vol. 420, pp. 868-874, 2002.

[6] H. D. Liang and M. J. K. Blomley, "The role of ultrasound in molecular imaging," *British Journal of Radiology,* vol. 76, pp. S140-S150, 2003.

[7] J. Folkman, "The role of angiogenesis in tumor growth," *Semin Cancer Biol,* vol. 3, pp. 65-71, 1992.

[8] H. F. Dvorak, "Vascular permeability factor/vascular endothelial growth factor: A critical cytokine in tumor angiogenesis and a potential target for diagnosis and therapy," *Journal of Clinical Oncology,* vol. 20, pp. 4368-4380, 2002.

[9] F. A. Jaffer, P. Libby, and R. Weissleder, "Molecular and cellular imaging of atherosclerosis - Emerging applications," *Journal of the American College of Cardiology,* vol. 47, pp. 1328-1338, 2006.

[10] W. B. Cai and X. Y. Chen, "Multimodality molecular imaging of tumor angiogenesis," *Journal of Nuclear Medicine,* vol. 49, pp. 113S-128S, 2008.

[11] J. R. Lindner, M. P. Coggins, S. Kaul, A. L. Klibanov, G. H. Brandenburger, and K. Ley, "Microbubble persistence in the microcirculation during ischemia/reperfusion and inflammation is caused by integrin- and complement-mediated adherence to activated leukocytes," *Circulation,* vol. 101, pp. 668-675, 2000.

[12] G. ter Haar, "Ultrasound bioeffects and safety," *Proceedings of the Institution of Mechanical Engineers Part H-Journal of Engineering in Medicine,* vol. 224, pp. 363-373, 2010.

[13] D. Cosgrove and N. Lassau, "Imaging of perfusion using ultrasound," *European Journal of Nuclear Medicine and Molecular Imaging,* vol. 37, pp. S65-S85, 2010.

[14] J. M. Mari, K. Hibbs, E. Stride, R. J. Eckersley, and M. X. Tang, "An Approximate Nonlinear Model for Time Gain Compensation of Amplitude Modulated Images of Ultrasound Contrast Agent Perfusion," *Ieee Transactions on Ultrasonics Ferroelectrics and Frequency Control,* vol. 57, pp. 818-829, 2010.

[15] J. R. Lindner, "Molecular imaging with contrast ultrasound and targeted microbubbles," *Journal of Nuclear Cardiology,* vol. 11, pp. 215-221, 2004.

[16] M. J. K. Blomley, J. C. Cooke, E. C. Unger, M. J. Monaghan, and D. O. Cosgrove, "Science, medicine, and the future - Microbubble contrast agents: a new era in ultrasound," *British Medical Journal,* vol. 322, pp. 1222-1225, 2001.

[17] A. L. Klibanov, "Ligand-carrying gas-filled microbubbles: Ultrasound contrast agents for targeted molecular imaging," *Bioconjugate Chemistry,* vol. 16, pp. 9-17, 2005.

[18] B. A. Kaufmann, J. M. Sanders, C. Davis, A. Xie, P. Aldred, I. J. Sarembock, and J. R. Lindner, "Molecular imaging of inflammation in atherosclerosis with targeted ultrasound detection of vascular cell adhesion molecule-1," *Circulation,* vol. 116, pp. 276-284, Jul 2007.

[19] J. R. Lindner, J. Song, J. Christiansen, A. L. Klibanov, F. Xu, and K. Ley, "Ultrasound assessment of inflammation and renal tissue injury with microbubbles targeted to P-selectin," *Circulation,* vol. 104, pp. 2107-2112, Oct 2001.

[20] B. A. Kaufmann, C. Lewis, A. Xie, A. Mirza-Mohd, and J. R. Lindner, "Detection of recent myocardial ischaemia by molecular imaging of P-selectin with targeted contrast echocardiography," *European Heart Journal,* vol. 28, pp. 2011-2017, 2007.

[21] C. Bachmann, A. L. Klibanov, T. S. Olson, J. R. Sonnenschein, J. Rivera-Nieves, F. Cominelli, K. F. Ley, J. R. Lindner, and T. T. Pizarro, "Targeting mucosal addressin cellular adhesion molecule (MAdCAM)-1 to noninvasively image experimental Crohn's disease," *Gastroenterology,* vol. 130, pp. 8-16, 2006.

[22] P. C. Brooks, R. A. F. Clark, and D. A. Cheresh, "Requirement of vascular alpha v beta 3 for angiogenesis," *Science,* vol. 264, pp. 569-571, 1994.

[23] D. B. Ellegala, H. L. Poi, J. E. Carpenter, A. L. Klibanov, S. Kaul, M. E. Shaffrey, J. Sklenar, and J. R. Lindner, "Imaging tumor angiogenesis with contrast ultrasound and microbubbles targeted to alpha(v)beta(3)," *Circulation,* vol. 108, pp. 336-341, 2003.

[24] E. C. Unger, T. P. McCreery, R. H. Sweitzer, D. K. Shen, and G. L. Wu, "In vitro studies of a new thrombus-specific ultrasound contrast agent," *American Journal of Cardiology,* vol. 81, pp. 58G-61G, 1998.

[25] P. A. Schumann, J. P. Christiansen, R. M. Quigley, T. P. McCreery, R. H. Sweitzer, E. C. Unger, J. R. Lindner, and T. O. Matsunaga, "Targeted-microbubble binding selectively to GPIIb IIIa receptors of platelet thrombi," *Investigative Radiology,* vol. 37, pp. 587-593, 2002.

[26] J. J. Rychak, A. L. Klibanov, and J. A. Hossack, "Acoustic radiation force enhances targeted delivery of ultrasound contrast microbubbles: In vitro verification," *Ieee Transactions on Ultrasonics Ferroelectrics and Frequency Control,* vol. 52, pp. 421-433, 2005.

[27] P. Dayton, A. Klibanov, G. Brandenburger, and K. Ferrara, "Acoustic radiation force in vivo: A mechanism to assist targeting of microbubbles," *Ultrasound in Medicine and Biology,* vol. 25, pp. 1195-1201, 1999.

[28] P. A. Dayton, J. S. Allen, and K. W. Ferrara, "The magnitude of radiation force on ultrasound contrast agents," *Journal of the Acoustical Society of America,* vol. 112, pp. 2183-2192, 2002.

[29] S. Zhao, D. E. Kruse, K. W. Ferrara, and P. A. Dayton, "Selective imaging of adherent targeted ultrasound contrast agents," *Physics in Medicine and Biology,* vol. 52, pp. 2055-2072, Numb 8 2007.

[30] H. Leong-Poi, J. Christiansen, P. Heppner, C. W. Lewis, A. L. Klibanov, S. Kaul, and J. R. Lindner, "Assessment of endogenous and therapeutic arteriogenesis by contrast ultrasound molecular Imaging of integrin expression," *Circulation,* vol. 111, pp. 3248-3254, 2005.

[31] A. V. Patil, J. J. Rychak, J. S. Allen, A. L. Klibanov, and J. A. Hossack, "Dual frequency method for simultaneous translation and real-time imaging of ultrasound contrast agents within large blood vessels," *Ultrasound in Medicine and Biology,* vol. 35, pp. 2021-2030, Dec 2009.

[32] A. Needles, O. Couture, and F. S. Foster, "A method for differenciating targeted microbubbles in real time using subharmonic micro-ultrasound and interframe filtering.," *Ultrasound in Medicine and Biology,* vol. 35, pp. 1564-1573, Sep 2009.
[33] X. W. Hu, H. R. Zheng, D. E. Kruse, P. Sutcliffe, D. N. Stephens, and K. W. Ferrara, "A Sensitive TLRH Targeted Imaging Technique for Ultrasonic Molecular Imaging," *Ieee Transactions on Ultrasonics Ferroelectrics and Frequency Control,* vol. 57, pp. 305-316, Feb 2010.
[34] V. Garbin, D. Cojoc, E. Ferrari, E. Di Fabrizio, M. L. J. Overvelde, S. M. van der Meer, N. de Jong, D. Lohse, and M. Versluis, "Changes in microbubble dynamics near a boundary revealed by combined optical micromanipulation and high-speed imaging," *Applied Physics Letters,* vol. 90, Mar 2007.
[35] S. K. Zhao, D. E. Kruse, K. W. Ferrara, and P. A. Dayton, "Acoustic response from adherent targeted contrast agents," *Journal of the Acoustical Society of America,* vol. 120, pp. EL63-EL69, 2006.
[36] H. J. Vos, B. Dollet, J. G. Bosch, M. Versluis, and N. de Jong, "Nonspherical Vibrations of Microbubbles in Contact with a Wall--A Pilot Study at Low Mechanical Index," *Ultrasound in medicine & biology,* vol. 34, pp. 685-688, 2008.
[37] N. de Jong, A. Bouakaz, and P. Frinking, "Basic acoustic properties of microbubbles," *Echocardiography-a Journal of Cardiovascular Ultrasound and Allied Techniques,* vol. 19, pp. 229-240, 2002.
[38] L. Rayleigh, "On the pressure developed in a liquid during collapse of a spherical cavity," *Philosophical Magazine,* pp. 34:94-98, 1917.
[39] M. S. Plesset, "The dynamics of cavitation bubbles," *ASME J, Appl. Mech,* vol. 16, pp. 228-231, 1949.
[40] B. E. Noltingk and E. A. Neppiras, "Cavitation produced by Ultrasonics," *Proc Phys Soc London B,* pp. 674-685, 1950.
[41] M. Poritsky, "The collapse on growth of a spherical bubble on cavity in a viscous fluid," in *first US National Congress of Applied Mechanics*, Illinois Institute of Technology, 1951, pp. 813-821.
[42] A. Prosperetti, "Thermal effects and damping mechanisms in forced radial oscillations of gas-bubbles in liquids," *Journal of the Acoustical Society of America,* vol. 61, pp. 17-27, 1977.
[43] T. G. Leighton, *The acoustic bubble*. London: Academic Press Limited, 1994.
[44] N. de Jong, R. Cornet, and C. T. Lancee, "Higher harmonics of vibrating gas-filled microspheres. 1. Simulations," *Ultrasonics,* vol. 32, pp. 447-453, Nov 1994.
[45] C. C. Church, "The effects of an elastic solid-surface layer on the radial pulsations of gas-bubbles," *Journal of the Acoustical Society of America,* vol. 97, pp. 1510-1521, 1995.
[46] L. Hoff, P. C. Sontum, and J. M. Hovem, "Oscillations of polymeric microbubbles: Effect of the encapsulating shell," *Journal of the Acoustical Society of America,* vol. 107, pp. 2272-2280, 2000.
[47] P. Marmottant, S. van der Meer, M. Emmer, M. Versluis, N. de Jong, S. Hilgenfeldt, and D. Lohse, "A model for large amplitude oscillations of coated bubbles accounting for buckling and rupture," *Journal of the Acoustical Society of America,* vol. 118, pp. 3499-3505, 2005.
[48] M. Emmer, "The onset of bubble vibration," in *department of Biomedical Engineering*. vol. PhD Rotterdam: Erasmus Medical Centre, 2009.
[49] B. Haider and R. Y. Chiao, "Higher order nonlinear ultrasonic imaging," *1999 Ieee Ultrasonics Symposium Proceedings, Vols 1 and 2,* pp. 1527-1531, 1999.
[50] D. H. Simpson, C. T. Chin, and P. N. Burns, "Pulse inversion Doppler: A new method for detecting nonlinear echoes from microbubble contrast agents," *Ieee Transactions on Ultrasonics Ferroelectrics and Frequency Control,* vol. 46, pp. 372-382, Mar 1999.

[51] R. Eckersley, C. Chin, and P. Burns, "Optimising phase and amplitude modulation schemes for imaging microbubble contrast agents at low acoustic power," *Ultrasound in medicine & biology,* vol. 31, pp. 213-219, 2005.
[52] N. de Jong, P. J. A. Frinking, A. Bouakaz, and F. J. Ten Cate, "Detection procedures of ultrasound contrast agents," *Ultrasonics,* vol. 38, pp. 87-92, 2000.
[53] P. N. Burns, J. E. Powers, and T. Fritzsch, "Harmonic imaging: new imaging and Doppler method for contrast enhanced ultrasound," *Radiology,,* vol. 185 (P), pp. 142-142, 1992.
[54] G. A. Brock-Fisher, M. Poland, and P. G. Rafter, "Means for increasing sensitivity in nonlinear ultrasound imaging systems." vol. 5577505 United States Patent, 1996.
[55] P. J. Phillips, "Contrast Pulse Sequences (CPS): Imaging nonlinear microbubbles," in *IEEE International Ultrasonic Symposium*, Atlanta, Ga, 2001, pp. 1739-1745.
[56] J. Borsboom, A. Bouakaz, and N. de Jong, "Pulse Subtraction Time Delay Imaging Method for Ultrasound Contrast Agent Detection," *IEEE transactions on ultrasonics, ferroelectrics, and frequency control,* vol. 56, pp. 1151-1158, 2009.
[57] T. Albrecht, A. Urbank, M. Mahler, A. Bauer, C. J. Dore, M. J. K. Blomley, D. O. Cosgrove, and R. Schlief, "Prolongation and optimization of Doppler enhancement with a microbubble US contrast agent by using continuous infusion: Preliminary experience," *Radiology,* vol. 207, pp. 339-347, 1998.
[58] D. Cosgrove, "Why do we need contrast agents for ultrasound?," *Clinical Radiology,* vol. 51, pp. 1-4, 1996.
[59] R. P. Kedar, D. Cosgrove, V. R. McCready, J. C. Bamber, and E. R. Carter, "Microbubble contrast agent for color Doppler US: Effect on breast masses," *Radiology,* vol. 198, pp. 679-686, 1996.
[60] S. Shigeo, "Ultrasonic Doppler Method for the Inspection of Cardiac Functions," *The Journal of the Acoustical Society of America,* vol. 29, pp. 1181-1185, 1957.
[61] D. H. Evans and W. N. McDicken, *Doppler Ultrasound: Physics, Instrumentation and Signal Processing*: Wiley, John & Sons, Incorporated, 2000.
[62] O. Bonnefous and P. Pesque, "Time domain formulation of pulse-Doppler ultrasound and blood velocity estimations by cross-correlation," *Ultrasonic Imaging,* vol. 8, pp. 73-85, 1986.
[63] P. M. Embree and W. D. Obrien, "Volumetric blood flow via time domain correlation - Experimental - verification," *Ieee Transactions on Ultrasonics Ferroelectrics and Frequency Control,* vol. 37, pp. 176-189, 1990.
[64] J. A. Jensen, *Estimation of Blood Velocities Using Ultrasound: A Signal Processing Approach*: Cambridge University Press, 1996.
[65] C. Kasai, "Real-time two-dimensional blood flow imaging using an autocorrelation technique," *Ieee Transactions on Ultrasonics Ferroelectrics and Frequency Control,* vol. 33, pp. 94-94, 1986.
[66] U. M. Hamper, M. R. DeJong, C. I. Caskey, and S. Sheth, "Power Doppler imaging: Clinical experience and correlation with color Doppler US and other imaging modalities," *Radiographics,* vol. 17, pp. 499-513, 1997.
[67] D. H. Simpson, "Detecting and imaging microbubble contrast agents with ultrasound," in *Department of Medical Biophysics*. vol. PhD Toronto: University of Toronto, 2000.
[68] V. L. Newhouse, B. A. Schrope, V. Uhlendorf, S. Dubin, and M. Victor, "Second harmonic Doppler ultrasound blood perfusion measurement," *Ieee 1992 Ultrasonics Symposium : Proceedings, Vols 1 and 2,* pp. 1175-1177, 1992.
[69] P. N. Burns, J. E. Powers, D. H. Simpson, A. Brezina, A. Kolin, C. T. Chin, V. Uhlendorf, and T. Fritzsch, "Harmonic power mode Doppler using microbubble contrast agents - An improved method for small vessel flow imaging," *1994 Ieee Ultrasonics Symposium Proceedings, Vols 1-3,* pp. 1547-1550, 1994.
[70] A. Y. Kim, T. K. Kim, Y. H. Kim, J. K. Han, and B. I. Choi, "Comparison of harmonic and conventional power Doppler ultrasonography for assessment of

slow flow in hyperechoic tissue - Experimental study using a Doppler phantom," *Investigative Radiology,* vol. 35, pp. 105-110, 2000.

[71] S. K. Zhao, K. W. Ferrara, and P. A. Dayton, "Asymmetric oscillation of adherent targeted ultrasound contrast agents," *Applied Physics Letters,* vol. 87, 2005.

[72] V. Garbin, "Optical tweezers for the study of microbubble dynamics in ultrasound." vol. PhD Trieste: University of Trieste, 2006.

[73] J. R. Lindner, J. Song, F. Xu, A. L. Klibanov, K. Singbartl, K. Ley, and S. Kaul, "Noninvasive ultrasound imaging of inflammation using microbubbles targeted to activated leukocytes," *Circulation,* vol. 102, pp. 2745-2750, 2000.

[74] H. Becher and P. N. Burns, "Handbook of Contrast Echocardiography," Frankfurt and New York: Springer Verlag, 2000, p. 200.

[75] C. C. Shen and P. C. Li, "Pulse-inversion-based fundamental imaging for contrast detection," *Ieee Transactions on Ultrasonics Ferroelectrics and Frequency Control,* vol. 50, pp. 1124-1133, Sep 2003.

[76] W. T. Shi, C. S. Hall, P. G. Rafter, and Ieee, "Contrast Resonance Imaging with Embedded Ultrasound Imaging Pulses," in *2006 Ieee Ultrasonics Symposium, Vols 1-5, Proceedings*, 2006, pp. 212-215.

[77] K. Morgan, M. Averkiou, and K. Ferrara, "The effect of the phase of transmission on contrast agent echoes," *Ieee Transactions on Ultrasonics Ferroelectrics and Frequency Control,* vol. 45, pp. 872-875, Jul 1998.

[78] J. M. Gorce, M. Arditi, and M. Schneider, "Influence of bubble size distribution on the echogenicity of ultrasound contrast agents - A study of SonoVue (TM)," *Investigative Radiology,* vol. 35, pp. 661-671, Nov 2000.

[79] K. Chetty, E. Stride, C. Sennoga, J. Hajnal, and R. Eckersley, "High-speed optical observations and simulation results of SonoVue microbubbles at low-pressure insonation," *IEEE transactions on ultrasonics, ferroelectrics, and frequency control,* vol. 55, pp. 1333-1342, 2008.

[80] J. Christiansen and J. Lindner, "Molecular and cellular imaging with targeted contrast ultrasound," *Proceedings of the IEEE,* vol. 93, pp. 809-818, 2005.

[81] N. Deshpande, A. Needles, and J. K. Willmann, "Molecular ultrasound imaging: current status and future directions," *Clinical Radiology,* vol. 65, pp. 567-581, 2010.

[82] M. X. Tang, J. M. Mari, P. N. T. Wells, and R. J. Eckersley, "Attenuation correction ultrasound contrast agent imaging: elementary theory and preliminary experimental evaluation," *Ultrasound in Medicine and Biology,* vol. 34, pp. 1998-2008, Dec 2008.

[83] M. X. Tang, N. Kamiyama, and R. J. Eckersley, "Effects of nonlinear propagation in ultrasond contrast agent imaging," *Ultrasound in Medicine and Biology,* vol. 36, pp. 459-466, 2010.

[84] M. X. Tang and R. J. Eckersley, "Nonlinear propagation of ultrasound through microbubble contrast agents and implications for Imaging," *Ieee Transactions on Ultrasonics Ferroelectrics and Frequency Control,* vol. 53, pp. 2406-2415, 2006.

[85] D. Cosgrove, "Ultrasound contrast agents: An overview," *European Journal of Radiology,* vol. 60, pp. 324-330, 2006.

[86] FDA, "Information for manufacturers seeking marketing clearance of diagnostic ultrasound systems and transducers," 1997.

[87] M. Crocco, M. Palmese, C. Sciallero, and A. Trucco, "A comparative analysis of multi-pulse techniques in contrast-enhanced ultrasound medical imaging," *Ultrasonics,* vol. 49, pp. 120-125, 2009.

[88] P. Phillips and E. Gardner, "Contrast-agent detection and quantification," *European Radiology,* vol. 14, pp. P4-P10, Oct 2004.

[89] A. Bouakaz, S. Frigstad, F. J. Ten Cate, and N. de Jong, "Super harmonic imaging: A new imaging technique for improved contrast detection," *Ultrasound in Medicine and Biology,* vol. 28, pp. 59-68, Jan 2002.

[90] M. A. Averkiou, "Tissue harmonic ultrasonic imaging," *Comptes Rendus De L Academie Des Sciences Serie Iv Physique Astrophysique,* vol. 2, pp. 1139-1151, 2001.
[91] R. B. Peterson, L. E. Atlas, and K. W. Beach, "A comparison of IIR initialization techniques for improved color Doppler wall filter performance," *1994 Ieee Ultrasonics Symposium Proceedings, Vols 1-3,* pp. 1705-1708, 1994.
[92] L. Thomas and A. Hall, "An improved wall filter for flow imaging of low velocity flow," *1994 Ieee Ultrasonics Symposium Proceedings, Vols 1-3,* pp. 1701-1704, 1994.
[93] R. Senior, S. Kaul, P. Soman, and A. Lahiri, "Power Doppler harmonic imaging: A feasibility study of a new technique for the assessment of myocardial perfusion," *American Heart Journal,* vol. 139, pp. 245-251, 2000.
[94] T. J. Hunt, P. G. Rafter, and G. A. Brock-Fisher, "System and method for non-linear detection of ultrasonic contrast agents at a fundamental frequency." vol. 6,652,463 United States Patent, 2003.
[95] D. Maulik and I. Zalud, *Doppler ultrasound in obstetrics and gynecology*: Springer-Verlag New York, LLC, 2005.
[96] J. G. Abbott, "Rationale and derivation of Mi and Ti - A review," *Ultrasound in Medicine and Biology,* vol. 25, pp. 431-441, Mar 1999.
[97] Q. Y. Ma, D. Zhang, X. F. Gong, and Y. Ma, "Phase-coded multi-pulse technique for ultrasonic high-order harmonic imaging of biological tissues in vitro," *Physics in Medicine and Biology,* vol. 52, pp. 1879-1892, Apr 2007.
[98] Y. S. Lee and M. F. Hamilton, "Time-domain modeling of pulsed tinite-amplitude sound beams," *Journal of the Acoustical Society of America,* vol. 97, pp. 906-917, 1995.
[99] K. Chetty, J. V. Hajnal, and R. J. Eckersley, "Investigating the nonlinear microbubble response to chirp encoded, multipulse sequences," *Ultrasound in Medicine and Biology,* vol. 32, pp. 1887-1895, Dec 2006.
[100] J. M. G. Borsboom, C. T. Chin, A. Bouakaz, M. Versluis, and N. de Jong, "Harmonic chirp imaging method for ultrasound contrast agent," *Ieee Transactions on Ultrasonics Ferroelectrics and Frequency Control,* vol. 52, pp. 241-249, Feb 2005.
[101] B. A. Kaufmann and J. R. Lindner, "Molecular imaging with targeted contrast ultrasound," *Current Opinion in Biotechnology,* vol. 18, pp. 11-16, 2007.
[102] A. L. Klibanov, "Preparation of targeted microbubbles: ultrasound contrast agents for molecular imaging," *Medical & Biological Engineering & Computing,* vol. 47, pp. 875-882, Aug 2009.
[103] E. Talu, K. Hettiarachchi, S. Zhao, R. L. Powell, A. P. Lee, M. L. Longo, and P. A. Dayton, "Tailoring the size distribution of ultrasound contrast agents: Possible method for improving sensitivity in molecular imaging," *Molecular Imaging,* vol. 6, pp. 384-392, Nov-Dec 2007.
[104] E. Stride, C. Porter, A. G. Prieto, and Q. Pankhurst, "Enhancement of microbubble mediated gene delivery by simultaneous exposure to ultrasonic and magnetic fields," *Ultrasound in Medicine and Biology,* vol. 35, pp. 861-868, May 2009.
[105] C. A. Sennoga, V. Mahue, J. Loughran, J. Casey, M.-X. Tang, and R. J. Eckersley, "On sizing and counting of microbubbles using optical microscopy," 2010.
[106] D. W. Rickey, P. A. Picot, D. A. Christopher, and A. Fenster, "A wall-less vessel phantom for Doppler ultrasound studies," *Ultrasound in Medicine and Biology,* vol. 21, pp. 1163-1176, 1995.
[107] F. Forsberg, W. T. Shi, C. R. B. Merritt, Q. Dai, M. Solcova, and B. B. Goldberg, "On the Usefulness of the Mechanical Index Displayed on Clinical Ultrasound Scanners for Predicting Contrast Microbubble Destruction," *J Ultrasound Med,* vol. 24, pp. 443-450, April 1, 2005 2005.
[108] P. Tortoli, V. Michelassi, F. Guidi, M. Corsi, M. Hori, K. Ishihara, F. Moriyasu, and Y. Takeuchi, "Dynamic effect of acoustic radiation force on microbubbles,"

The Research Reports of the Faculty of Engineering, Kagoshima University 2001.

[109] J. S. Allen, D. E. Kruse, P. A. Dayton, and K. W. Ferrara, "Effect of coupled oscillations on microbubble behavior," *Journal of the Acoustical Society of America,* vol. 114, pp. 1678-1690, Sep 2003.

[110] E. Stride, K. Pancholi, M. J. Edirisinghe, and S. Samarasinghe, "Increasing the nonlinear character of microbubble oscillations at low acoustic pressures," *Journal of the Royal Society Interface,* vol. 5, pp. 807-811, 2008.

[111] C. A. Sennoga, J. S. Yeh, S. J. M., S. Nourshargh, R. J. Eckersley, D. O. Haskard, D. O. Cosgrove, and P. Nihoyannopoulos, "Microbulles ciblées pour l'imagerie ultrasonore," in *Échographie de contraste*, 1 ed Paris: Springer, 2007.

[112] A. L. Klibanov, P. T. Rasche, M. S. Hughes, J. K. Wojdyla, K. P. Galen, J. H. Wible, and G. H. Brandenburger, "Detection of individual microbubbles of ultrasound contrast agents - Imaging of free-floating and targeted bubbles," *Investigative Radiology,* vol. 39, pp. 187-195, 2004.

[113] T. Sugiura, K. Kooiman, M. Emmer, H. J. Vos, A. v. Wamel, and N. d. Jong, "Evaluation of the binding force between a biotinylated microbubble and a streptavidin-coated surface by ultrasound radiation," in *IEEE International Ultrasonics Symposium*, 2009.

[114] M. Writing Group, D. Lloyd-Jones, R. Adams, M. Carnethon, G. De Simone, T. B. Ferguson, K. Flegal, E. Ford, K. Furie, A. Go, K. Greenlund, N. Haase, S. Hailpern, M. Ho, V. Howard, B. Kissela, S. Kittner, D. Lackland, L. Lisabeth, A. Marelli, M. McDermott, J. Meigs, D. Mozaffarian, G. Nichol, C. O'Donnell, V. Roger, W. Rosamond, R. Sacco, P. Sorlie, R. Stafford, J. Steinberger, T. Thom, S. Wasserthiel-Smoller, N. Wong, J. Wylie-Rosett, Y. Hong, C. for the American Heart Association Statistics, and S. Stroke Statistics, "Heart Disease and Stroke Statistics--2009 Update: A Report From the American Heart Association Statistics Committee and Stroke Statistics Subcommittee," *Circulation,* vol. 119, pp. e21-181, January 27, 2009 2009.

[115] R. T. Lee, A. J. Grodzinsky, E. H. Frank, R. D. Kamm, and F. J. Schoen, "Structure-dependent dynamic mechanical behavior of fibrous caps from human atherosclerotic plaques," *Circulation,* vol. 83, pp. 1764-1770, May 1991.

[116] H. Hasegawa, H. Kanai, N. Hoshimiya, N. Chubachi, and Y. Koiwa, "Measurement of local elasticity of human carotid arterial walls and its relationship with risk index of atherosclerosis," *1998 Ieee Ultrasonics Symposium - Proceedings, Vols 1 and 2,* pp. 1451-1454, 1998.

[117] C. Schmitt, G. Soulez, R. L. Maurice, M. F. Giroux, and G. Cloutier, "Noninvasive vascular elastography: Toward a complementary characterization tool of atherosclerosis in carotid arteries," *Ultrasound in Medicine and Biology,* vol. 33, pp. 1841-1858, Dec 2007.

[118] N. Dejong, R. Cornet, and C. T. Lancee, "Higher harmonics of vibrating gas-filled microspheres. 1. Simulations," *Ultrasonics,* vol. 32, pp. 447-453, Nov 1994.

[119] E. Sassaroli and K. Hynynen, "Resonance frequency of microbubbles in small blood vessels: a numerical study," *Physics in Medicine and Biology,* vol. 50, pp. 5293-5305, Nov 2005.

[120] S. P. Qin and K. W. Ferrara, "The natural frequency of nonlinear oscillation of ultrasound contrast agents in microvessels," *Ultrasound in Medicine and Biology,* vol. 33, pp. 1140-1148, Jul 2007.

[121] S. Martynov, E. Stride, and N. Saffari, "The natural frequencies of microbubble oscillation in elastic vessels," *Journal of the Acoustical Society of America,* vol. 126, pp. 2963-2972, Dec 2009.

[122] C. F. Caskey, D. E. Kruse, P. A. Dayton, T. K. Kitano, and K. W. Ferrara, "Microbubble oscillation in tubes with diameters of 12, 25, and 195 microns," *Applied Physics Letters,* vol. 88, 2006.

[123] D. Thomas, M. Emmer, H. Vos, V. Sboros, and N. d. Jong, "Optical Observations of Microbubble Oscillation in Small Tubes," in *IEEE International Ultrasonics Symposium*, Rome, Italy, 2009, pp. ref. P-S-11.
[124] K. Khanafer, "Effects of strain rate, mixing ratio, and stress–strain definition on the mechanical behavior of the polydimethylsiloxane (PDMS) material as related to its biological applications," *Biomedical Microdevices,* vol. 11, pp. 503-508, 2009.
[125] C. M. Cesa, N. Kirchgessner, D. Mayer, U. S. Schwarz, B. Hoffmann, and R. Merkel, "Micropatterned silicone elastomer substrates for high resolution analysis of cellular force patterns," *Review of Scientific Instruments,* vol. 78, p. 10, Mar 2007.
[126] Y. C. Fung, *Bioemechanics: Mechanical properties of living tissue*, second edition ed.: Springer, 1993.
[127] A. Noble, R. Johnson, A. Thomas, and P. Bass, "The cardiovascular system," Churchill Livingstone, 2005.
[128] S. D. Masouros, K. H. Parker, A. M. Hill, A. A. Amis, and A. M. J. Bull, "Testing and modelling of soft connective tissues of joints: a review," *Journal of Strain Analysis for Engineering Design,* vol. 44, pp. 305-318, 2009.
[129] S. CA, Y. JS, S. JM, N. S, E. RJ, H. DO, C. DO, and N. P., "Microbulles ciblées pour l'imagerie ultrasonore," in *Échographie de contraste*, 1 ed Paris: Springer, 2007.
[130] W. T. Shi, F. Forsberg, R. Bautista, C. Vecchio, R. Bernardi, and B. B. Goldberg, "Image enhancement by acoustic conditioning of ultrasound contrast agents," *Ultrasound in Medicine and Biology,* vol. 30, pp. 191-198, Feb 2004.
[131] S. Hilgenfeldt, D. Lohse, and M. Zomack, "Response of bubbles to diagnostic ultrasound: a unifying theoretical approach," *European Physical Journal B,* vol. 4, pp. 247-255, 1998.
[132] D. B. Khismatullin, "Resonance frequency of microbubbles: Effect of viscosity," *Journal of the Acoustical Society of America,* vol. 116, pp. 1463-1473, 2004.
[133] D. L. Miller, "Ultrasonic detection of resonant cavitation bubbles in a flow tube by their second harmonic emissions," *Ultrasonics,* vol. 19, pp. 217-224, 1981.
[134] M. Strasberg, "The Pulsation Frequency of Nonspherical Gas Bubbles in Liquids," *The Journal of the Acoustic Society of America,* vol. 25, 1953.
[135] A. A. Doinikov, J. F. Haac, and P. A. Dayton, "Resonance frequencies of lipid-shelled microbubbles in the regime of nonlinear oscillations," *Ultrasonics,* vol. 49, pp. 263-268, 2009.
[136] K. Chetty, "Ultrasound Contrast Agents. Microbubble Modelling and Advanced Detection Strategies," in *Imaging Sciences Department*. vol. PhD London: Imperial College London, 2007.
[137] C. T. Chin, C. Lancee, J. Borsboom, F. Mastik, M. E. Frijlink, N. de Jong, M. Versluis, and D. Lohse, "Brandaris 128: A digital 25 million frames per second camera with 128 highly sensitive frames," *Review of Scientific Instruments,* vol. 74, pp. 5026-5034, Dec 2003.
[138] D. H. Thomas, M. B. Butler, T. Anderson, R. Steel, S. D. Pye, M. Poland, T. Brock-Fisher, W. N. McDicken, and V. Sboros, "Single microbubble response using pulse sequences: initial results," *Ultrasound in Medicine and Biology,* vol. 35, pp. 112-119, Jan 2009.
[139] A. Bouakaz, M. Versluis, J. Borsboom, and N. de Jong, "Radial modulation of microbubbles for ultrasound contrast imaging," *Ieee Transactions on Ultrasonics Ferroelectrics and Frequency Control,* vol. 54, pp. 2283-2290, 2007.
[140] F. Forsberg, W. T. Shi, and B. B. Goldberg, "Subharmonic imaging of contrast agents," *Ultrasonics,* vol. 38, pp. 93-98, 2000.
[141] A. M. Takalkar, A. L. Klibanov, J. J. Rychak, J. R. Lindner, and K. Ley, "Binding and detachment dynamics of microbubbles targeted to P-selectin under controlled shear flow," *Journal of Controlled Release,* vol. 96, pp. 473-482, 2004.

[142] P. A. Dayton, "Improving technology for molecular imaging with ultrasound," *2009 Ieee International Symposium on Biomedical Imaging: From Nano to Macro, Vols 1 and 2,* pp. 751-753, 2009.
[143] B. J. Schmidt, I. Sousa, A. A. van Beek, and M. R. Bohmer, "Adhesion and ultrasound-induced delivery from monodisperse microbubbles in a parallel plate flow cell," *Journal of Controlled Release,* vol. 131, pp. 19-26, 2008.
[144] H. R. Zheng, D. E. Kruse, D. N. Stephens, K. W. Ferrara, P. Sutcliffe, and E. Gardner, "A Sensitive Ultrasonic Imaging method for Targeted Contrast Microbubble Detection," *2008 30th Annual International Conference of the Ieee Engineering in Medicine and Biology Society, Vols 1-8,* pp. 5290-5293, 2008.
[145] O. Couture, S. Bannouf, G. Montaldo, J.-F. Aubry, M. Fink, and M. Tanter, "Ultrasfast imaging of ultrasound contrast agents," *Ultrasound in Medicine and Biology,* vol. 35, pp. 1908-1916, 2009.
[146] S. Mehier-Humbert, F. Yan, P. Frinking, M. Schneider, R. H. Guy, and T. Bettinger, "Ultrasound-mediated gene delivery: Influence of contrast agent on transfection," *Bioconjugate Chemistry,* vol. 18, pp. 652-662, 2007.
[147] Q. L. Lu, H. D. Liang, T. Partridge, and M. J. K. Blomley, "Microbubble ultrasound improves the efficiency of gene transduction in skeletal muscle in vivo with reduced tissue damage," *Gene Therapy,* vol. 10, pp. 396-405, 2003.

Appendix

The Matlab™ code[6] used to simulate the response of a microbubble is provided in this appendix. It was based on the de Jong model [44] described by Equation 2.1.

```
function [Echo] = EchoCalc(pBase,fs)
c0=1500; % speed of sound
rho=1000; %water density
p0=1e5; %ambient pressure

data = pBase; tdata = linspace(0,length(data)*1/fs,length(data));
pulse.p = data; pulse.t = tdata; pulse.fs = fs;
% pulse = BPfilter(pulse,0.5e7,7e3);

pslen=pulse.t(end); %pulse length
sp=abs(fft(pulse.p));
f0=(find(sp==max(sp))-1)/(length(pulse.p)-1)*pulse.fs;%find the central frequency
omega=f0(1)*2*pi;%pulse central freq
%.....................................................................
R0 = 3e-6;% size 3e-6 is the resonance size for 1.9MHz insonation, obtained by simulation with
NonlinearOsciRPNNP, the theoretical value is also roughly the same;
%.....................................................................
dx=1.5e-5;%1.5e-5;
dt=dx/c0; %temporal sample frequency match with spatial grid
nt=round(pulse.t(end)/dt);    %number of time points

t=0:dt:pulse.t(end);%linspace(0,totaltime,nt);
p=(interp1(pulse.t, pulse.p,t))';

nt=nt*2; t=[t t+pulse.t(end)+dt];%patch some zeros at the end of the data
p(nt/2+1:nt)= 0;
R1=zeros(nt,1)+R0; dR1=zeros(nt,1); ddR1=zeros(nt,1);
```

[6] This de Jong model [44] code was programmed by Dr Mengxing Tang from the Ultrasound Group, Imperial College London.

```
for j=3:nt
        rr=RungeKutta(j*dt,[R1(j-1);dR1(j-1)],dt,p(j),omega,R0);
        R1(j)=rr(1);
        dR1(j)=rr(2);
end
ddR1=[0; diff(dR1)]/dt;

rho=998;%density
distance=0.05;%1;%1metre away

scatp=rho/distance*(R1.^2.*ddR1+2*R1.*dR1.^2); Echo = scatp;

end

---------------------------------------------------------------------------------------------------------------
function r=RungeKutta(t0,r0,dt,p,omega,R0)
%this function carries out 1-step Runge-Kutta method to solve the ODE defined
%in RPNNP
%t0: the initial time point
%r0: the initial condition including radius and its derivative at t0
%R0: the equilibrium radius, different from r0
%dt: time step
%p:  acoustic pressure at t0
%omega: central frequency of insonation

k1=dt*RPNNP(t0,r0,p,omega,R0);
k2=dt*RPNNP(t0+dt/2,r0+k1/2,p,omega,R0);
k3=dt*RPNNP(t0+dt/2,r0+k2/2,p,omega,R0);
k4=dt*RPNNP(t0+dt,r0+k3,p,omega,R0);

r=r0+(k1+2*k2+2*k3+k4)./6;

end
```